Measuring precision, temporal decorrelation, and integrative analysis of InSAR with different frequency bands

（異周波数帯の干渉SARの計測精度，時間干渉性低下及び統合的解析手法に関する研究）

Yu Morishita

Department of Natural History Sciences, Graduate School of Science,

Hokkaido University

Submitted for the degree of Doctor of Philosophy

September 2016

Contents

Abstract

Ground surface deforms due to various causes on earth. Measuring and monitoring ground surface displacement can contribute to disaster prevention and mitigation. Synthetic aperture radar (SAR) interferometry (InSAR), one of the useful geodetic techniques to measure the displacement, provides spatially dense information with high resolution and has revealed a lot of detailed crustal and ground deformations. In recent years, InSAR time series analysis, which is feasible by abundant and high quality SAR data, has revealed very slow deformation on the order of a few mm/yr. Diversity of available radar frequency bands, i.e., L-, C- and X-band, enables us to choose the optimal data depending on a target. Moreover, integrative use of these data with different bands will disclose unknown deformation which conventional techniques cannot detect. It is important for the selection of the optimal data and the integrative use to comprehend the difference of the features among the different bands.

One of the inevitable problems for InSAR is decorrelation. InSAR can no longer measure deformation when a condition of ground surface changes greatly. As the decorrelation proceeds quickly with time over pasture on drained peat soils in the Netherlands, which is one of the study areas in this thesis, conventional InSAR techniques including time series analysis methods such as Persistent Scatterer Interfer-

ometry (PSI) and Small BAseline Subset (SBAS) have not succeeded in detecting the detailed displacement so far. Moreover there is no other effective measuring method because stable ground observation points cannot be installed on the soft soils. Peat soils are decreasing because of drainage for agricultural use, resulting in subsidence and emission of greenhouse gases. Therefore, figuring out the height change over peat meadows is crucial for flood hazard assessment, water management, and global warming prevention.

In this thesis, I will mention mainly following three topics about InSAR with different bands.

(1) Comparison of PSI measuring capability of L- and C-band

InSAR time series analysis is a promising technique to monitor slow displacement, e.g., subsidence and deformation of infrastructures. To be used as a monitoring method, it is necessary to know the measuring capability, i.e., what deformation can be detected. However, there are few studies about measuring precision of L-band data by comparing with ground observation data, whereas many studies using C- and X-band exist because they have much available data. Moreover, leveling results which have only a vertical component and sparse GNSS data are mainly used as the ground data to be compared, which might be insufficient for quantitative evaluation.

Here I conduct PSI analysis using L- and C-band data, quantitatively assess the measuring precision, and compare the results between L- and C-band. The study area is around Omaezaki city, Japan, where continuous GNSS observation stations have been densely deployed. According to the result, density of identified PS points is proportional to the inherent spatial resolution of the used data. In vegetated ar-

eas, L-band is superior than C-band in terms of detection of PS points. Measuring precision of an individual PS point is 8-11 mm and 2-3 mm for L-band and C-band, respectively, almost proportional to the wavelength, which means shorter wavelength is more suitable for pointwise usage such as infrastructure monitoring. According to the comparison with GNSS, measuring accuracy of spatially averaged neighboring PS points tends to have no dependency on the wavelength, 4-6 mm of LOS displacement and 2 mm/yr of mean LOS velocity. In other words, L-band can have comparable precision with C-band by spatially averaging the measurement of neighboring PS points.

(2) Quantitative assessment of temporal decorrelation in L-, C-, and X-band

Temporal decorrelation behavior of InSAR depends on bands of used data and scattering properties on the ground. In an area where temporal decorrelation is faster than the minimum interferometric time interval, i.e., revisit time of a satellite, it is impossible to measure displacement by spaceborne SAR interferometry. Therefore the feasibility of measuring displacement by InSAR in a area with quick temporal decorrelation is determined by the radar wavelength, the scattering properties and the revisit time of a satellite.

First, a temporal decorrelation model described by three parameters is proposed. Next, coherence of interferograms produced from actual SAR data with three different bands (L-, C- and X-band) is calculated. The result shows that interferograms with a short time interval can have adequate coherence and that the coherence tends to be higher in winter than in summer on the condition that no sudden and complete change of ground surface (e.g., cultivation or snow fall) occurs. Then the parame-

ters of the temporal decorrelation model for each wavelength and for each season are estimated from the calculated coherence data. As a result, it is quantitatively shown that the temporal decorrelation is slower in a longer wavelength and in winter. Moreover it is also quantitatively proven that the larger number of independent samples for multilook, i.e., higher inherent spatial resolution can provide more significant information. New SAR satellites that have a shorter revisit time than their predecessors' have a possibility to allow more noteworthy interferometric results.

(3) Displacement extraction by integrative InSAR analysis

A short time interval of an interferometric pair is crucial to obtain adequate coherence in quickly decorrelating peat meadow. However, a short time interval means small displacement for slowly deforming phenomena such as subsidence. Hence, it is difficult to measure the displacement because of relatively large noise (low SNR). Even InSAR time series analysis methods such as PSI and SBAS, which mitigate noises and can detect small displacement by using a large amount of data, have not succeeded in achieving adequate measuring precision yet in the target area.

Here I propose an advanced method to obtain a more robust solution by integrative use of SAR data with different wavelengths and incidence angles. I also propose an efficient adaptive coherence estimation method to improve the precision of coherence estimator and multilooked phases by filtering out scatterers with a different scattering property from surrounding major scatterers. Applying these methods, precise displacement behavior over the pasture has been detected for the first time. The pasture area has subsided 33.6 mm/yr with annual up-down fluctuations of 10.6 mm amplitude, maximum on 17 February and minimum on 18 August on average.

概要

地表面は様々な要因によって変動しており，その変動を計測・監視することにより，防災・減災に貢献することができる．変動を計測するための測地学的手法の一つである干渉SARは，面的かつ高分解能な情報をもたらし，多くの詳細な地殻・地盤変動を明らかにしてきた．特に近年では，高品質なSARデータの蓄積により可能となった時系列解析と呼ばれる手法により，数mm/yrといった微小な速度で進行する変動が検出可能となっている．また，L，C，Xといった異なる周波数帯のデータが利用可能になり，対象に応じて最適なデータを選択することが可能になってきた．さらに，これら異なる特性を持つ異周波数帯のデータを統合的に利用することで，従来では検出できなかった変動も捉えられるようになることが期待される．最適なデータの選択や統合的利用のためには，異周波数帯の特性の違いを把握することは重要である．

干渉SARにおいて不可避な問題として，干渉性の低下がある．地表面の状態が大きく変化してしまうと，干渉性が低下してしまい，干渉SARでは変動計測が不可能となる．本研究の対象地域の一つであるオランダの泥炭草地は，時間の経過とともに干渉性が急速に低下する特性があり，PSIやSBASといった時系列解析手法を含む従来の干渉SARの手法では詳細

な変動を検出するに至っていない．また，軟弱な地盤であるため，安定した地上観測点を設置することができず，他の有効な変動計測手法も存在しない．しかし，農業利用のための排水により泥炭は減少しており，地盤沈下及び温室効果ガスの排出につながっている．泥炭草地の高さの変化を把握することは洪水危険性評価，地下水管理及び地球温暖化対策にとって重要である．

本論文では，異周波数帯の干渉SARの研究について，主に以下3つの話題を記述する．

(1) L及びCバンドの変動計測能力の比較

時系列解析は微小な速度で進行する地盤沈下や構造物の変形等の監視への利用が期待されているが，監視手法として利用するためには，どの程度の変動であれば検出可能であるのかを把握しておく必要がある．しかし，これまでに実施されてきた地上観測データとの比較による精度検証は，主に多量の観測データが存在するCバンドやXバンドによるものであり，Lバンドの事例は少なかった．また，比較対象の地上観測データは，鉛直方向のみの水準測量や低密度なGNSS観測データが多く，定量的な評価としては十分とは言い切れない．

そこで，高密度にGNSS連続観測が実施されている静岡県御前崎市周辺を対象に，Lバンド及びCバンドのデータを使用して時系列解析（PSI）を実施し，変動計測精度の定量的な評価及び異周波数帯同士の比較を行った．その結果，PS点密度はデータの空間分解能が高いほど高く，植生地域においてはLバンドに優位性が見られた．個々のPS点の計測誤差はLバンドで8-11mm程度，Cバンドで2-3mm程度で，おおむね波長に比例するため，

構造物監視等には短い波長が適していると考えられる．GNSS観測結果との比較から，空間平均したPS点の計測誤差に波長依存性はあまり見られず，LOS変位量で4-6mm程度，LOS平均変位速度で2mm/yr程度であった．これらのことから，ある程度のPS点を空間的に平均することにより，Lバンドでも**C**バンドに匹敵する精度が得られると考えられる．

(2) L，C，Xバンドにおける時間干渉性低下の定量的評価

干渉SARにおける時間干渉性低下速度は，レーダーの周波数帯（波長）及び対象地域の散乱特性に依存する．また，衛星搭載SARでは，最短の時間間隔は衛星の回帰日数と等しく，それよりも速く干渉性が低下してしまう地域では，干渉SARでは変動計測は不可能になってしまう．よって，時間干渉性低下が急速な地域における干渉SARによる変動計測の可否は，レーダーの波長，対象地域の散乱特性，衛星の回帰日数によって決まるといえる．

まず，時間干渉性低下を3つのパラメータにより表現するモデルを導出した．次に，研究対象地域の泥炭草地において，L，C，Xの3つの周波数帯のSARデータを使用してSAR干渉解析を実施し，干渉性の指標であるコヒーレンスを計算した．結果から，時間間隔が短い干渉ペアであれば十分なコヒーレンスが得られることがあること，また，季節依存性があり，冬季ではコヒーレンスが高い傾向にあることがわかった．さらに，実データから計算されたコヒーレンスを使用して，各周波数帯における時間干渉性低下モデルのパラメータを季節ごとに推定した．その結果，時間干渉性低下は長波長ほど遅いこと，また冬季には遅いことを定量的に示した．また，空間平均する独立標本数が多いほど，つまりセンサー固有の空間分解能が

高いほど，有意な結果が得られやすいことが定量的に示された．回帰日数の短い新たなSAR衛星であれば，当該地域でより有意な結果が得られる可能性があることがわかった．

(3) 複数衛星干渉SARの統合的利用による変動計測

対象地域である泥炭草地では，十分な干渉性を得るには時間間隔が短い必要がある．しかし，時間的にゆっくり変動する地盤沈下のような現象において，時間間隔が短いということは変動量が小さいことを意味し，相対的に誤差の影響が大きく変動を計測することは困難となる．多量のデータを利用して誤差を低減し微小な変動を検出することができるPSIやSBASといった干渉SAR時系列解析においても，従来の手法では十分な計測精度を得ることはできていない．

そこで，波長や入射角が異なるデータを統合的に利用することでデータ量を増やし，解の信頼度を高める計算手法を考案した．また，周囲とは異なる特性を持つ散乱体を除去してコヒーレンス及び平均化位相の推定精度を高めるため，効率的な適応型コヒーレンス推定手法を考案した．これらの手法を使用した結果，泥炭草地での変動分布が初めて詳細に捉えられた．平均では33.6mm/yrの地盤沈下，2月17日頃に極大，8月18日頃に極小となり10.6mmの振幅を持つ年周変動が推定された．

Acknowledgment

This thesis is based on my researches conducted at Delft University of Technology (TU Delft) as a visiting researcher supported by Ministry of Education, Culture, Sports, Science and Technology (MEXT) in 2012, and conducted at Geospatial Information Authority of Japan (GSI) in 2014. I would like to express my gratitude to everyone who has helped and encouraged me.

First of all, I would like to express my greatest gratitude to Prof. Ramon Hanssen for his support, patience, motivation, and immense knowledge. He kindly welcomed me though I had few research accomplishments at that time, and he showed a tolerant attitude to my unfluent English.

Also, I would like to appreciate very much Prof. Masato Furuya for undertaking the chair of my thesis committee and his valuable comments. He introduced me to Prof. Hanssen to start the research at TU Delft, which led to this research and thesis. Additionally, I would like to thank the rest of my thesis committee, Prof. Kosuke Heki, Prof. Makoto Murakami and Prof. Youichiro Takada for their constructive comments. In particular, Prof. Heki got me interested in geodesy by his impressive supervision when I was a university student, which resulted in my current position.

I would like to thank Mr. Sami Samiei-Esfahany, Dr. Miguel Caro Cuenca, and all the other colleagues in Radar Group of TU Delft for giving me valuable knowl-

edge through discussions and meetings. I would like to appreciate the colleagues in the department of Geoscience & Remote Sensing and all my Japanese friends in the Netherlands for making my stay in the Netherlands wonderful.

I also would like to thank people in GSI. The excellent people and working environment in GSI enabled my researches and accomplishments. In particular, Dr. Tomokazu Kobayashi, Dr. Mikio Tobita (now at JAXA), Mr. Hiroshi Yarai, Ms. Tomomi Amagai, Mr. Akira Suzuki, and Dr. Satoshi Fujiwara have provided me with much knowledge about InSAR since I started to engage in the InSAR project in GSI. Also, Mr. Masayuki Yamanaka, Dr. Koji Matsuo, Mr. Yuji Miura, Mr. Kozin Wada (now at MEXT), Dr. Hiroshi Munekane, Mr. Satoshi Kawamoto, and Mr. Basara Miyahara greatly helped my work and research, resulting in completion of my thesis.

ALOS/PALSAR data used in this thesis were purchased by GSI through the joint cooperative agreement between GSI and Japan Aerospace Exploration Agency (JAXA). The ownership of the ALOS/PALSAR data belongs to JAXA and Ministry of Economy, Trade and Industry (METI). I also would like to thank GSI and MEXT for providing an opportunity to study in the Netherlands.

Last but not the least, I would like to express my hearty appreciation to my parents for their understanding and warm support.

謝辞

本論文は，筆者が文部科学省平成23年度宇宙関係在外研究員としてデルフト工科大学へ派遣された際に実施した研究，及び平成26年度に国土地理院で実施した研究をまとめたものです．これまでご支援・ご協力を賜りました全ての方々へ感謝の意を表します．

まず，本研究を実施するにあたり，多大なるご指導・ご助言を賜りましたデルフト工科大学のRamon Hanssen教授に深く感謝申し上げます．実績もない筆者を快く受け入れ，拙い英語にも親切に接してくださいました．

また，学位論文審査委員会の主査を担当してくださいました，古屋正人教授に心よりお礼申し上げます．古屋教授には留学先の相談にも乗っていただき，Hanssen教授を紹介していただいたことが本研究に繋がりました．さらに，副査を担当してくださいました日置幸介教授，村上亮教授，高田陽一郎准教授にも深く感謝いたします．特に，日置教授には筆者が北海道大学在学中にご指導を賜り，それにより測地学に魅了され，現職に就くきっかけとなりました．ありがとうございました．

筆者が滞在時にデルフト工科大学に在籍していたSami Samiei-Esfahany氏，Miguel Caro Cuenca博士，その他Radar Groupのメンバーからは，日々の議論やミーティングを通して多くの貴重な知識を得ることがで

きました．また，Geoscience & Remote Sensing学科のメンバー，在蘭日本人の友達など多くの方々のおかげで，1年間のオランダ滞在が素晴らしいものになりました．本当にありがとうございました．

国土地理院の関係者の皆様にも，心から感謝申し上げます．この素晴らしい環境のおかげで，干渉SARをはじめとする測地技術に深い興味を抱き，多くの知識を習得することができ，本研究へとつながりました．特に小林知勝博士，飛田幹男博士（現JAXA），矢来博司氏，雨貝知美氏，鈴木啓氏，藤原智博士からは，筆者が干渉SARに携わった初期の頃から，干渉SARについて多くのことを学ばせていただきました．また，山中雅之氏，松尾功二博士，三浦優司氏，和田弘人氏（現文部科学省），宗包浩志博士，川元智氏，宮原伐折羅氏からは，国土地理院での業務や研究において多大なるお力添えをいただき，そのおかげで博士論文を完成させることができました．今後もよろしくお願いいたします．

本研究で使用したALOS/PALSARのデータは，国土地理院と宇宙航空研究開発機構（JAXA）との協定に基づき，国土地理院が購入したものです．ALOS/PALSARの著作権はJAXA及び経済産業省にあります．また，在外研究員派遣の機会を与えてくださった国土地理院及び文部科学省にもお礼申し上げます．

最後に，これまで自分の思う道に進ませていただき，それを温かく見守ってくれた両親に心から感謝いたします．

Nomenclature

List of acronyms

ALOS	Advanced Land Observing Satellite
APS	atmospheric phase screen
ASTER GDEM	Advanced Spaceborne Thermal Emission and Reflection Radiometer Global Digital Elevation Model
DEM	digital elevation model
Doris	Delft object-oriented radar interferometric software
DS	distributed scatterer
Envisat	Environmental Satellite
ERS-1	European Remote-Sensing Satellite 1
FBD	Fine Beam Dual polarization
FBS	Fine Beam Single polarization
GEONET	GNSS Earth Observation Network System
GLS	generalized least squares
GNSS	Global Navigation Satellite System
GSI	Geospatial Information Authority of Japan
InSAR	synthetic aperture radar interferometry
IRLS	iteratively reweighted least squares
JMA	Japan Meteorological Agency
LOS	line-of-sight
LP	linear and seasonal periodic component
LS	least squares
MODIS	Moderate Resolution Imaging Spectroradiometer
NDVI	Normalized Difference Vegetation Index

NESZ	Noise Equivalent Sigma Zero
PS	persistent scatterer
PSI	Persistent Scatterer Interferometry
RS2	RADARSAT-2
SAR	synthetic aperture radar
SBAS	Small BAseline Subset
SHP	statistically homogeneous pixel
SNR	signal-to-noise ratio
SRTM	Shuttle Radar Topography Mission
StaMPS/MTI	Stanford Method for Persistent Scatterers / Multi-Temporal InSAR
SVD	singular value decomposition
TSX	TerraSAR-X
VC	variance-covariance

List of symbols

cm	centimeter
deg	degree
km	kilometer
m	meter
mm	millimeter
rad	radian
yr	year

$\bar{\cdot}$	averaged value
$\hat{\cdot}$	estimated value
$\{\cdot\}'$	approximated value
$\{\cdot\}^*$	complex conjugate
$\{\cdot\}_{\mathrm{ERS}}$	parameter for ERS data set
$\{\cdot\}_i$	parameter for i^{th} interferogram
$\{\cdot\}_j$	parameter for j^{th} image
$\{\cdot\}^K$	parameter for K^{th} data set
$\{\cdot\}_{\mathrm{v}}$	vertical component of parameter
$E\{\cdot\}$	expectation operator
${}_pF_q(a;b;z)$	Generalized hypergeometric function

Γ	Gamma function
γ	(theoretical) complex coherence
γ_0	initial coherence
γ_∞	long term coherence
γ_{proc}	coherence reduction due to processing error
γ_{spat}	coherence reduction due to spatial decorrelation
γ_{td}	coherence associated with total decorrelation
γ_{temp}	coherence reduction due to temporal decorrelation
γ_{therm}	coherence reduction due to thermal noise
γ_{vol}	coherence reduction due to volume decorrelation
$\Delta_{\text{azi}}, \Delta_{\text{gr}}$	pixel spacing of azimuth and ground range
$\boldsymbol{\epsilon}$	vector of observation errors
θ	incidence angle
λ	radar wavelength
$\rho_{\text{azi}}, \rho_{\text{gr}}$	spatial resolution of azimuth and ground range
σ	standard deviation
σ^2	variance
τ	decorrelation rate
$\boldsymbol{\phi}$	vector of unwrapped interferometric differential phase with regard to reference image
ϕ	unwrapped interferometric differential phase with regard to reference image
ϕ^{LP}	LP component of ϕ
ϕ_n	systematic (linear) phase component
$\boldsymbol{\delta\phi}$	vector of unwrapped interferometric differential phase
$\boldsymbol{\delta\phi'}$	vector of improved unwrapped phase without DEM error
$\delta\phi$	unwrapped interferometric differential phase
$\delta\phi^{\text{atm}}$	differential phase of APS
$\delta\phi^{\text{defo}}$	differential phase due to surface displacement along LOS
$\delta\phi^{\text{noise}}$	differential phase due to other error contributions
$\delta\phi^{\text{orb}}$	residual phase caused by satellite orbit inaccuracies
$\delta\phi^{\text{topo}}$	residual topographic phase caused by DEM error
$\boldsymbol{\psi}$	vector of phase of SAR image

ψ	phase of SAR image
$\mathbf{A}$, $\mathbf{M}$, $\mathbf{c}$	design matrix
A	amplitude of seasonal periodic displacement
$B_\perp$	perpendicular baseline
B_{crit}	critical baseline
$\mathbf{d}$	vector of LOS displacement
d	LOS displacement
L	number of independent samples; number of looks
N	number of samples
Q	VC matrix
r	range distance
S , C	coefficients describing seasonal periodic displacement
Δt	time offset of seasonal periodic displacement
dt	time interval
t_{td}	decorrelation time
v	linear deformation rate
$\mathbf{x}$	vector of LP deformation model parameters
y_1, y_2	complex stochastic values
Δz	DEM error

Chapter 1

Introduction

1.1 Ground surface deformation and measuring methods

Ground surface of the earth deforms by various causes, e.g., earthquakes (preseismic, coseismic, postseismic and interseismic), volcanic activities, ground subsidence and landslides. These natural disasters sometimes bring serious consequences for human society. Monitoring and measuring the deformation can contribute to disaster prevention and mitigation.

Various geodetic techniques have been developed and employed to measure the deformation. Leveling is one of the most classical but precise methods to measure relative elevation and vertical displacement. Global Navigation Satellite System

(GNSS) has become a major monitoring way recently, which can provide temporally contiguous three dimensional displacement globally and locally with high precision. Synthetic aperture radar (SAR) interferometry (InSAR) achieves spatially continuous observation, giving dense information.

Each technique has advantages and disadvantages; there is no perfect technique. A proper method should be selected depending on a characteristic of the deformation to be measured, or a combination of these techniques is more effective than individual ones. For example, while leveling and GNSS have higher precision than InSAR, they are not suitable for discovering unknown local displacement because they need ground observation instruments and their spatial density is limited.

1.2 Objective and outline of this thesis

A research objective of this thesis is to extract a deformation signal by an advanced InSAR processing approach in a region where there has been no suitable and satisfactory measuring methods so far. I investigate features of different radar frequency bands and feasibility in the study area, develop a multisatellite InSAR algorithm, and validate with real data.

Chapter 2 provides fundamentals of SAR, InSAR and time series analysis, and features of various SAR satellites.

Chapter 3 clarifies measuring precision of PSI using L- and C-band SAR data, and difference of the features between two bands.

Chapter 4 describes features of the study area, pasture on drained peat soils in the Netherlands, and limitations of existing techniques.

Chapter 5 is dedicated to a feasibility study on the use of InSAR in terms of coherence in the target area. A temporal decorrelation model is proposed and temporal decorrelation behavior is evaluated using numerous real SAR data.

Chapter 6 describes an advanced InSAR processing algorithm using multisatellite data. Detailed displacement in the area is revealed precisely by applying the integrative algorithm with the real data.

Chapter 7 summarizes this research.

Chapter 2

SAR Interferometry

2.1 SAR

SAR is an imaging radar technique with high spatial resolution. A SAR antenna is usually mounted on an airplane or satellite and transmits microwave pulses to the ground during the flight. Figure 2.1 depicts the geometry of a SAR observation. The flying and looking direction is called azimuth and range, respectively. The range direction is slanting, not vertical to the ground. An angle between the vertical axis and the slant range direction is called off-nadir angle, slightly smaller than the incidence angle due to the earth curvature. The SAR antenna also receives backscattering of the transmitted pulses from the ground, which has information of amplitude and a fraction of phase. While the amplitude represents intensity of the backscatter, the phase is related to distance between the SAR antenna and the ground. High resolution is achieved by a synthetic aperture technique in the azimuth direction and a pulse

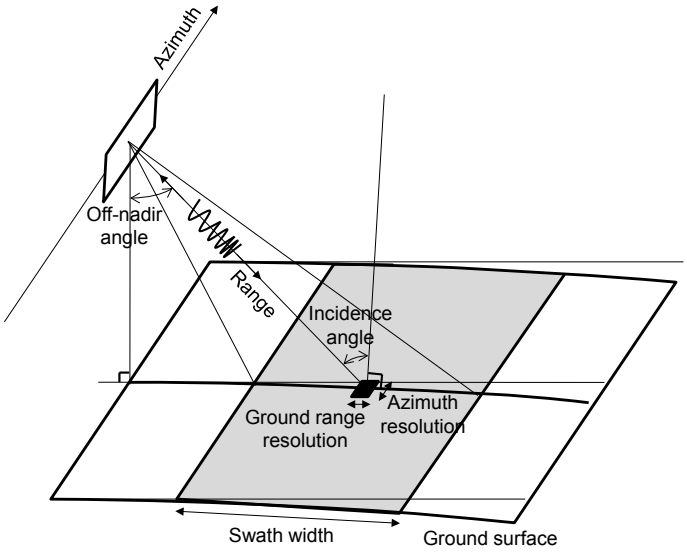

Figure 2.1: Geometry of a SAR observation.

compression technique in the range direction (Curlander and McDonough, 1991).

In this thesis various satellite SAR data are used. Different SAR satellites have different characteristics, e.g., revisit time and wavelengths. Table 2.1 lists past and present major SAR satellites, and their specifications.

2.2 InSAR

If two or more SAR images with almost identical geometry exist, InSAR can be applied (Figure 2.2). InSAR calculates phase difference, consisting of several components. One of the main components is topography. The InSAR technique has been initially developed for estimation of topography (Jordan et al., 1996; Bamler, 1999). Another component is ground surface displacement. If the topography (i.e., the topographic phase component) is known, ground surface displacement can be separated on the order of millimeters or centimeters (Massonnet et al., 1993). This

Table 2.1: Past and present major SAR satellites

Satellite	Year	Country	dt[a]	Band
ERS-1	1991 - 2000	EU	35	C
JERS-1	1992 - 1998	Japan	44	L
ERS-2	1995 - 2011	EU	35	C
RADARSAT-1	1995 - 2013	Canada	24	C
Envisat	2002 - 2012	EU	35	C
ALOS	2006 - 2011	Japan	46	L
RADARSAT-2	2007 -	Canada	24	C
TerraSAR-X	2007 -	Germany	11	X
COSMO-SkyMed[b]	2007 -	Italy	16	X
TanDEM-X	2010 -	Germany	11	X
Sentinel-1A	2014 -	EU	12	C
ALOS-2	2014 -	Japan	14	L

[a] Standard revisit time (day)
[b] Constellation of four satellites

technique is called Differential InSAR (DInSAR) as well as simply InSAR. Since several kinds of useful global digital elevation models (DEM) are available currently (e.g., Shuttle Radar Topography Mission (SRTM, Farr et al. (2007)) DEM and Advanced Spaceborne Thermal Emission and Reflection Radiometer Global Digital Elevation Model (ASTER GDEM, Tachikawa et al. (2011))), DInSAR can be applied every land on earth (except higher latitude than 83°). DInSAR has detected ground surface displacement due to various mechanisms, such as tectonics (Massonnet et al., 1994; Ozawa et al., 1997; Tobita et al., 2011; Kobayashi et al., 2011, 2012; Abe et al., 2013), volcanism (Fujiwara et al., 2000; Nishimura et al., 2001; Furuya, 2005; Ozawa and Fujita, 2013; Takada and Fukushima, 2013), subsidence (Nakagawa et al., 1999; Ng et al., 2009) and landslides (Kimura and Yamaguchi, 2000; Une et al., 2008; Sato et al., 2012, 2014). In this thesis, InSAR means DInSAR, not for the topographic

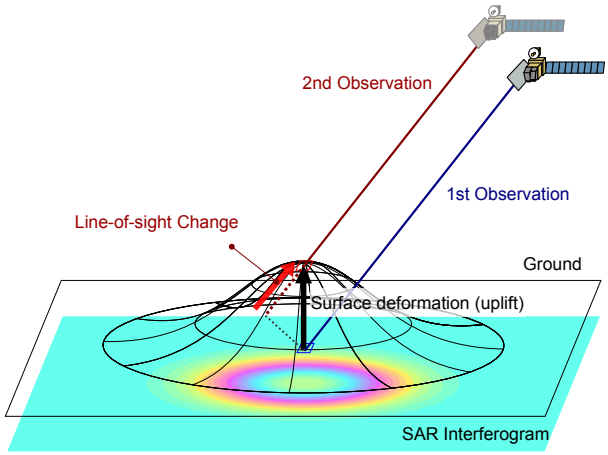

Figure 2.2: Principle of InSAR.

estimation. The reader is referred to Bamler and Hartl (1998); Rosen et al. (2000); Hanssen (2001) for further reference on the SAR and InSAR technique.

Scattering properties at the same location between SAR acquisitions used for InSAR should be as identical as possible in order to get a better coherent signal. A drastic change of the surface condition, e.g., snow coverage or land formation, leads to loss of coherence, called decorrelation. No deformation signal can be extracted from a decorrelated interferogram.

One of the most crucial factors affecting on coherence is a frequency band (wavelength) of the transmitted microwave. The wavelengths of L-, C-, X-band are approximately 24 cm, 5.6 cm, 3.1 cm, respectively. While L-band radar can generally penetrate vegetation and reach stable ground, C- and X-band cannot (Figure 2.3). One of the reasons why Japanese SAR satellites have an L-band sensor is to obtain a coherent signal even in widely and densely distributed vegetated areas all over the country. However L-band also has drawbacks, e.g., high sensitivity to ionospheric disturbances (Rignot, 2000; Wright et al., 2003). Moreover, Sandwell et al. (2008)

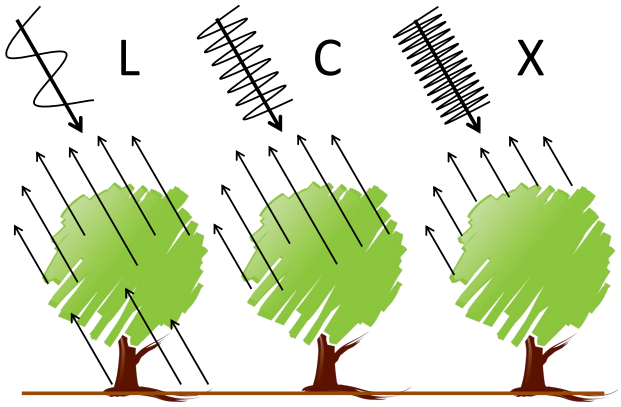

Figure 2.3: Difference of transparency between different bands.

reported that L-band has lower measuring precision than C-band.

The interferometric differential phase $\delta\phi$ contains several phase components,

$$\delta\phi = \delta\phi^{\text{defo}} + \delta\phi^{\text{topo}} + \delta\phi^{\text{orb}} + \delta\phi^{\text{atm}} + \delta\phi^{\text{noise}}, \tag{2.1}$$

where $\delta\phi^{\text{defo}}$ is the differential phase due to surface displacement along a line-of-sight (LOS) direction between two acquisitions, $\delta\phi^{\text{topo}}$ is the residual topographic phase caused by a DEM error, $\delta\phi^{\text{orb}}$ is the residual phase caused by satellite orbit inaccuracies, $\delta\phi^{\text{atm}}$ is the differential phase of atmospheric phase screen (APS) between two acquisitions and $\delta\phi^{\text{noise}}$ includes the other error contributions such as a coregistration error and decorrelation. These phase components have different spatial and temporal characteristics. $\delta\phi^{\text{topo}}$ always comes out at the same location where the DEM error exists and is proportional to a perpendicular baseline ($B_{\perp}$, the perpendicular component of the distance of the satellite at two acquisitions to the look direction) of the interferometric pair. $\delta\phi^{\text{orb}}$ is a smooth plane and proportional to the orbit inaccuracy. $\delta\phi^{\text{atm}}$ is also spatially smooth but temporally random. $\delta\phi^{\text{orb}}$ and $\delta\phi^{\text{atm}}$ are long wavelengths in space domain and can be dramatically reduced by fitting the phase to the

ground truth surface deformation data collected by, e.g., GNSS or leveling if they are available (Wei et al., 2010; Kobayashi et al., 2011; Tong et al., 2013).

2.3 InSAR time series analysis

InSAR time series analysis overcomes the cumbersome noises seriously contaminating the conventional InSAR result (Hooper et al., 2012). Using a lot of images allows reduction of the noises, resulting in high precision of the measurement. There are mainly two different approaches, Persistent Scatterer (PS) Interferometry (PSI) and Small BAseline Subset (SBAS). PSI focuses on pointwise, stable and hardly decorrelating scatterers, e.g., buildings or rocks (Ferretti et al., 2000, 2001; Kampes, 2005; Hooper et al., 2007). SBAS increases signal-to-noise ratio (SNR) by using interferometric pairs only with a small perpendicular baseline and a time interval, and multilooking at the expense of spatial resolution (Berardino et al., 2002; Pepe et al., 2005; Lanari et al., 2007). In both methods, temporally random atmospheric noise $\delta\phi^{\mathrm{atm}}$ can be mitigated by a statistical approach. Hybrid techniques have also been proposed recently (Hooper, 2008; Ferretti et al., 2011). In recent days these approaches are becoming a standard instead of the conventional InSAR owing to abundantly accumulated SAR data and rapid development of the analytical techniques. Many applications have been reported, such as to tectonics (Furuya et al., 2007; Arıkan et al., 2010; Fukushima and Hooper, 2010; Peyret et al., 2011), to volcanism (Hooper et al., 2004, 2007; Doin et al., 2011; Ozawa and Ueda, 2011; Champenois et al., 2014), to subsidence (Crosetto et al., 2008; López-Quiroz et al., 2009; Aobpaet et al., 2013; Arimoto et al., 2013), to landslides (Ferretti et al., 2011; Sun et al., 2014)

and to infrastructures (Arikan and Hanssen, 2008; Chang and Hanssen, 2012, 2014; Shamshiri et al., 2014).

Chapter 3

Comparison of PSI measuring capability of L- and C-band

Paper was published in *Journal of the Geodetic Society of Japan*

Morishita, Y., 2015: Comparison of PSI Results between L- and C-band SAR Data, *J. Geod. Soc. Jpn.*, 61(3), 157-166. (In Japanese with English abstract)

3.1 Introduction

As mentioned in Section 2.3, PSI can measure deformation at identified PS points with high spatial resolution and high precision. PSI is a promising technique for deformation monitoring, e.g., subsidence and infrastructure. In order to use PSI as a monitoring method, it is important to know its measuring capability, i.e., what deformation can be detected. However, there are few studies about measuring precision of L-band data by comparing with ground observation data, whereas many studies using C- and X-band have been conducted because there have been much available data of these bands since earlier times (Crosetto et al., 2008). Moreover, leveling results which have only a vertical component and sparse GNSS data are mainly used as the ground data to be compared, which might be insufficient for quantitative evaluation. Here I conduct PSI analysis using L- and C-band data, quantitatively assess the measuring precision, and compare the results between L- and C-band.

3.2 Study area, data and method

3.2.1 Study area and "H points"

The study area is around Omaezaki city, Shizuoka, Japan, where a lot of ground observation equipments such as seismometers and strain meters have been densely deployed in order to detect a preslip of a coming Tokai earthquake (Figure 3.1). As

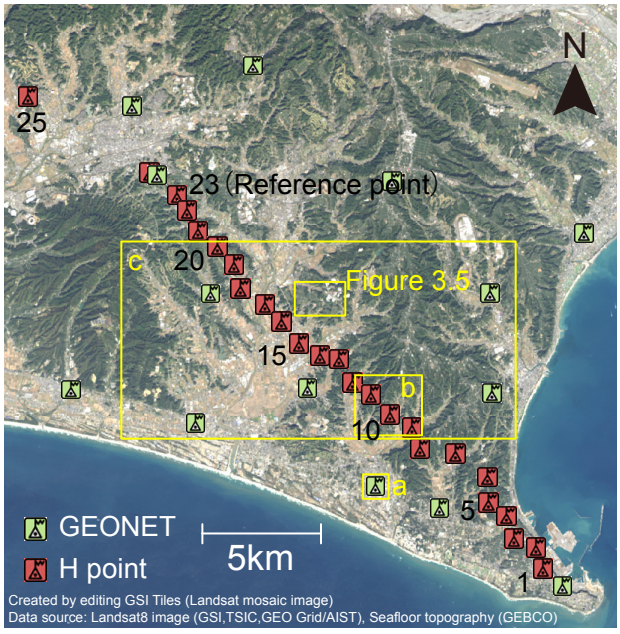

Figure 3.1: An optical image of the study area and locations of GNSS continuous observation points. Numbers represent identification number of the H points. Characters of a-c indicate areas where density of PS points is computed (Table 3.2).

a part of the dense ground observation network, Geospatial Information Authority of Japan (GSI) started continuous GNSS observation at 25 stations (called H points) in 1999, in addition to GNSS Earth Observation Network System (GEONET) which consists of approximately 1300 stations all over Japan (Kawawa and Suga, 2000). The interval between each H point and between other GNSS stations in this region are only about 1 km and 10 km, respectively, whereas standard GEONET stations in other areas have an about 20 km interval. In other words, this area has one of the densest GNSS observation network in the world.

According to the result of the continuous GNSS observation, steady northwestward deformation and subsidence has been detected at the southeastern tip of the peninsula, with an amount of about 1 cm/yr (Figure 3.2).

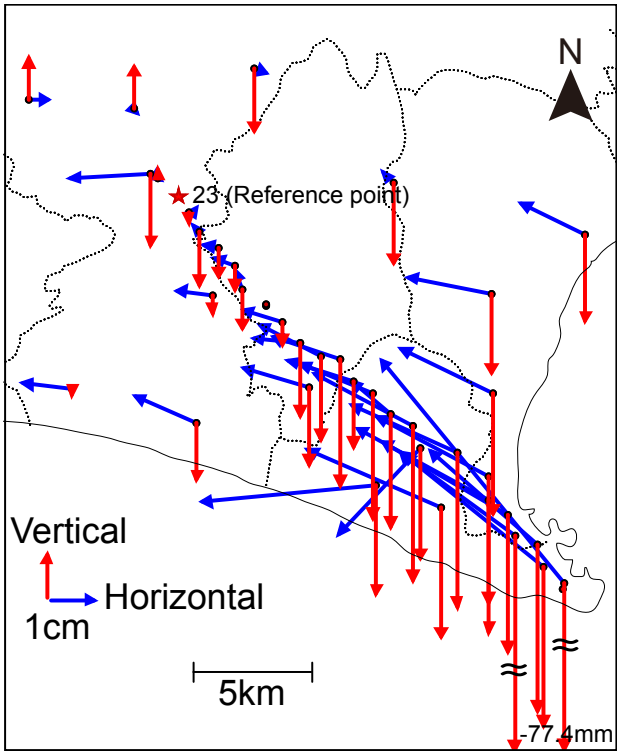

Figure 3.2: Displacement observed by GNSS at GNSS continuous observation points for seven years (2004-2011). A red star represents the reference point. Red and blue arrows on each point indicate vertical and horizontal displacement, respectively.

3.2.2 Data

I used L-band Advanced Land Observing Satellite (ALOS) data and C-band RADARSAT-1 data. Both ALOS and RADARSAT-1 have two data sets, i.e., four data sets of AA, AD, RDF, and RDS are available, which have different orbital directions, observation modes, or incidence angles (Table 3.1, Figure 3.3). Although the observation periods are not identical (ALOS; Oct. 2006 - Jan. 2011, RADARSAT-1; Apr 2004 - Mar 2007), the trend of the deformation in the study area had been steady according to the GNSS observation. Regarding the RDF data set, 12 data with a relatively long perpendicular baseline compared to the critical baseline were rejected due to inadequate coherence (Figure 3.3).

Table 3.1: Specifications of used data sets

Data set	**AA**	**AD**	**RDF**	**RDS**
Satellite	**A**LOS		**R**ADARSAT-1	
Wavelength	23.6 cm (L-band)		5.6 cm (C-band)	
Flight direction	Ascending (**A**)	Descending (**D**)		
Mode	FBS / FBD		**F**ine	**S**tandard
Incidence angle	39°		44°	22°
Spatial resolution	4 m × 9 m (FBS) / 17 m (FBD)		6 m × 10 m	6 m × 32 m
Observation period	2007/01/15 2011/01/26	2006/10/16 2010/09/11	2004/04/22 2007/03/14	2004/07/23 2007/01/21
Number of data	24 (FBD: 11)	19 (FBD: 1)	23	32 (Rejected: 12)
Critical baseline	14,000 m (FBS) / 7,000 m (FBD)		5,800 m	1,100 m

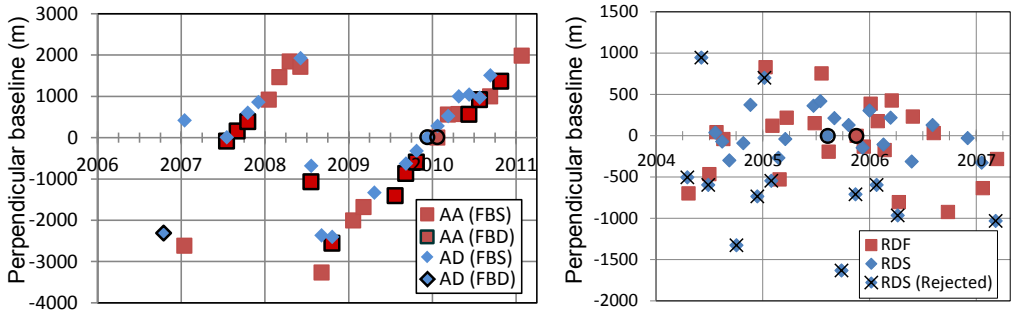

Figure 3.3: Baseline configurations of the used data sets (Table 3.1) of ALOS (left) and RADARSAT-1 (right). A large absolute value of a perpendicular baseline means a bad condition for interferometry due to spatial decorrelation (Zebker and Villasenor, 1992). Note that RDS is much more vulnerable to a long perpendicular baseline due to the much shorter critical baseline than the other data sets (Table 3.1). Circles indicate a common single master used in the PSI processing for each data set. Black frame borders of the symbols in ALOS indicate FBD data, while symbols without the border are FBS data. Cross marks in RDS represent rejected data due to too long perpendicular baselines.

3.2.3 Method

I applied PSI using Stanford Method for Persistent Scatterers / Multi-Temporal InSAR (StaMPS/MTI) software (Hooper et al., 2007; Fukushima, 2010). Main pa-

rameter settings are common for all four data sets and as follows. A threshold of amplitude dispersion to select PS candidates is 0.4, which is the standard value. A threshold of phase standard deviation to remove PS candidates with large noises is 0.7 as a result of trial and error. The identified PS points were not downsampled. Phase ramps caused by orbital errors were removed by using GNSS data except for at H points (Kobayashi et al., 2011). Tropospheric noise reduction using a numerical weather model provided by Japan Meteorological Agency (JMA) was applied to ALOS data (Kobayashi et al., 2014).

3.3 Results and discussion

3.3.1 Mean LOS velocity

Estimated mean LOS velocities of the four data sets show a common signal; LOS extension in the southeast area (Figure 3.4). These results are consistent with the results of other ground observations such as GNSS and leveling. The AA data set, whose observation is only from west, shows smaller LOS extension than the others. This is because westward deformation which has been detected by GNSS has an effect to cancel out the LOS extension caused by the subsidence for an observation from west.

3.3.2 Density of PS points

Figure 3.4 shows that the density of the PS points varies substantially among the data sets and areas. I computed the density of the PS points in an urban area, a mountainous area, and a broad area for each data set (Figure 3.1, Table 3.2). I also

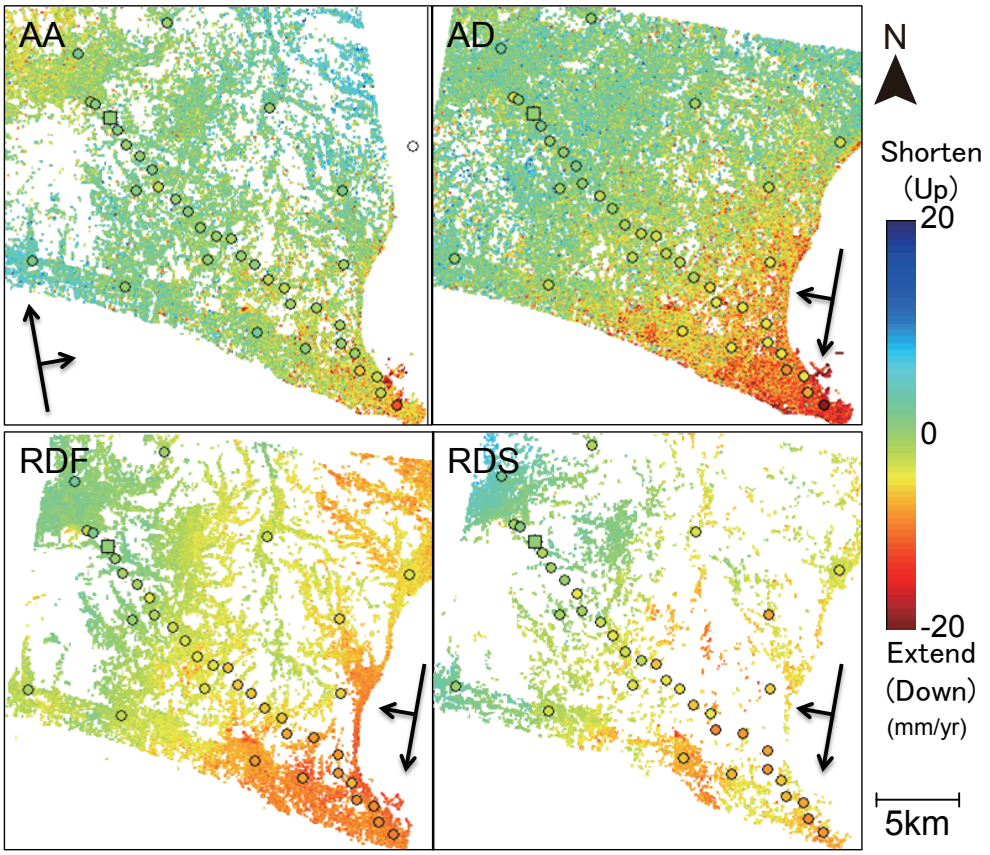

Figure 3.4: Distribution maps of the estimated mean LOS velocity at identified PS points. Long arrows indicate flight direction of the satellite, while short ones indicate beam direction. Circles and their colors represent locations of GNSS continuous observation points and their LOS velocity observed by GNSS, respectively. Squares indicate the reference point; 23th H point.

computed a ratio of spatial resolution of the data to the RDF data set because it is expected that the density of PS points depends on inherent spatial resolution of the data.

According to Table 3.2, the urban area has higher density (200-1500 km^{-2}) than the broad area for all data sets. The ratio of RDS to RDF (both are C-band) in the urban area is comparable to the ratio of the spatial resolution, implying that the density of PS points is basically proportional to the inherent spatial resolution of used

Table 3.2: Density of PS points (km^{-2}) and ratios of spatial resolution to RDF data set. Numbers in parentheses are ratios of density of PS points to RDF data set.

Data set	**AA**	**AD**	**RDF**	**RDS**
a (Urban)	1180 (1.4)	1443 (1.7)	840 (1.0)	210 (0.3)
b (Mountains)	82 (3.3)	237 (9.5)	25 (1.0)	0 (0.0)
c (Broad)	266 (1.5)	568 (3.2)	178 (1.0)	35 (0.2)
Ratio of spatial resolution	1.2	1.6	1.0	0.3

data. Although the L-band data sets have higher density than the C-band data sets, the ratio is almost proportional to the resolution. These facts suggest that the density of PS points in urban areas dominantly depends on the spatial resolution of the data, without dependence on the wavelength. This is probably because buildings which are regarded as PS points in an urban area are stable scatterers for all wavelength.

In the mountainous area, the L-band data sets clearly have higher density than the C-band data sets. Figure 3.5 shows the distribution of the PS points on various land conditions. On areas without vegetation, all data sets including C-band have PS points. On the other hand, on tea gardens, there are almost no PS points for C-band, whereas L-band have more or less. These facts indicate that L-band has an advantage in vegetated areas like a tea garden. It has to be noted that, however, L-band cannot identify PS points in all vegetated areas, as no PS point is seen in tree areas even in L-band (Figure 3.5).

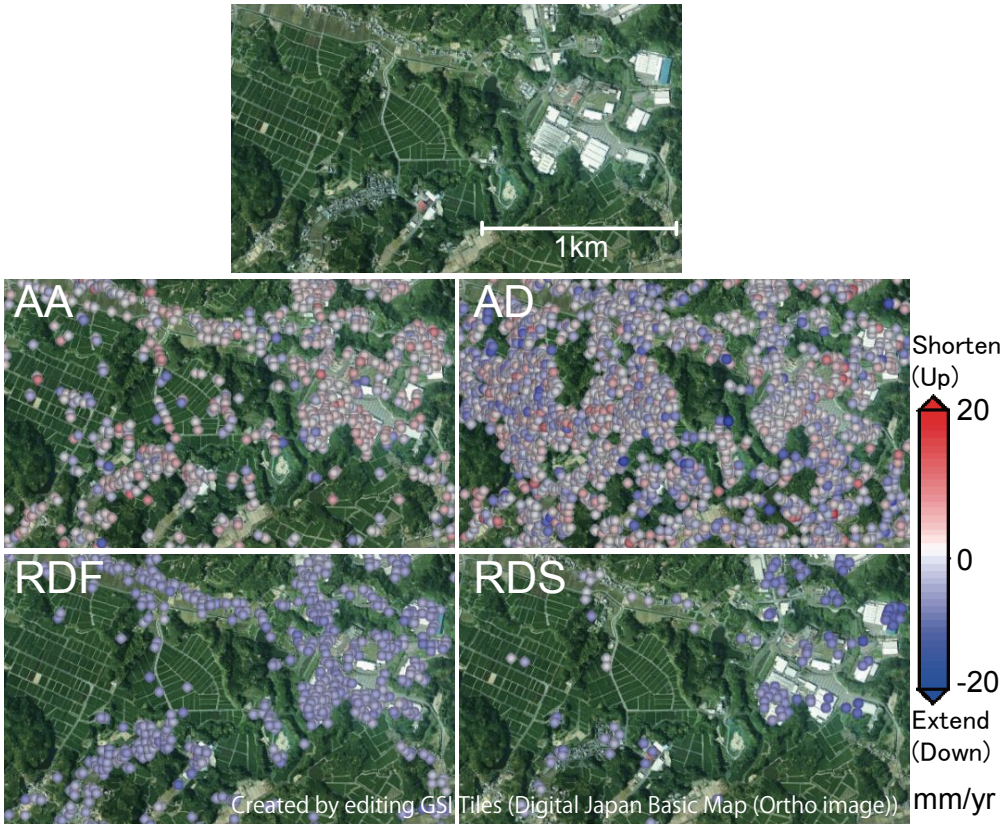

Figure 3.5: Distribution of PS points (circles). Green surface with narrow paths represents tea gardens. While there are many PS points at buildings for all data sets, ALOS also finds out many PS points on tea gardens. There is no PS point in areas with trees among all data sets.

3.3.3 Measuring precision of an individual PS point

As mentioned in Section 2.2, an observed differential phase at a PS point is composed of several components,

$$\delta\phi = \delta\phi^{\mathrm{defo}} + \delta\phi^{\mathrm{topo}} + \delta\phi^{\mathrm{orb}} + \delta\phi^{\mathrm{atm}} + \delta\phi^{\mathrm{noise}}. \tag{2.1}$$

Here a deformation signal $\delta\phi^{\text{defo}}$ is decomposed into three in terms of a spatial scale,

$$\delta\phi^{\text{defo}} = \delta\phi^{\text{defo,broad}} + \delta\phi^{\text{defo,local}} + \delta\phi^{\text{defo,point}}, \tag{3.1}$$

where $\delta\phi^{\text{defo,broad}}$ is a broad component such as interseismic deformation, $\delta\phi^{\text{defo,local}}$ is a local component such as subsidence, and $\delta\phi^{\text{defo,point}}$ is pointwise component such as deformation of a building. In a narrow area (< 1 km), $\delta\phi^{\text{defo,broad}}$, $\delta\phi^{\text{atm}}$, and $\delta\phi^{\text{orb}}$ are small enough to be ignored. $\delta\phi^{\text{topo}}$ can be removed precisely in the processing of PSI (Ferretti et al., 2001). Hence, in a narrow area, $\delta\phi$ can be rewritten as

$$\delta\phi \approx \delta\phi^{\text{defo,local}} + \delta\phi^{\text{defo,point}} + \delta\phi^{\text{noise}}, \tag{3.2}$$

and the variance is

$$\sigma^2_{\delta\phi} \approx \sigma^2_{\delta\phi^{\text{defo,local}}} + \sigma^2_{\delta\phi^{\text{defo,point}}} + \sigma^2_{\delta\phi^{\text{noise}}}, \tag{3.3}$$

where $\sigma_{\delta\phi}$ is the standard deviation of $\delta\phi$. Therefore,

$$\sigma^2_{\delta\phi^{\text{noise}}} \leq \sigma^2_{\delta\phi}, \tag{3.4}$$

and in an area where $\delta\phi^{\text{defo,local}}$ and $\delta\phi^{\text{defo,point}}$ are very small,

$$\sigma^2_{\delta\phi^{\text{noise}}} \approx \sigma^2_{\delta\phi}. \tag{3.5}$$

Consequently, (the maximum of) the measuring error of an individual PS point can be estimated from the standard deviation of the differential phases at PS points in a narrow area.

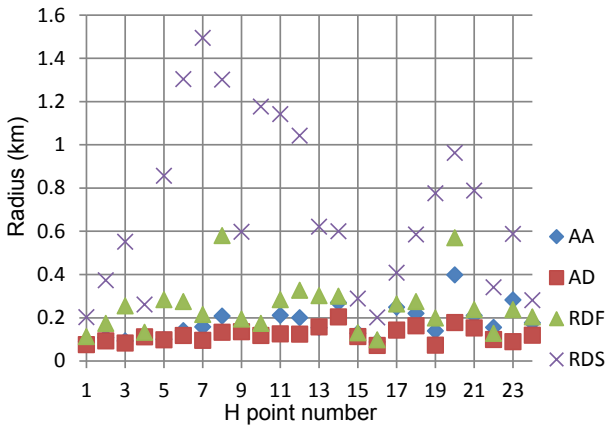

Figure 3.6: Radii within which there are 30 PS points around each H point.

Here I computed the standard deviation of unwrapped differential phases of 30 PS points around each H point for each data set. 30 PS points are mostly located within a 500 m radius from each H point, which means that Equation (3.2) holds (Figure 3.6). Moreover, since no localized subsidence is seen from the PSI results around all H points and it is unlikely that much pointwise deformation exists, Equation (3.5) holds.

The computed $\sigma_{\delta\phi}$ are mostly 8-11 mm for ALOS and 2-3 mm for RADARSAT-1, roughly proportional to the wavelength (Figure 3.7). It is natural because the same precision in a unit of phase (rad) leads to higher precision in a unit of length (mm) for a shorter wavelength (Sandwell et al., 2008). Several points with larger $\sigma_{\delta\phi}$ than 3 mm in C-band would be caused by a contribution of long wavelength components ($\delta\phi^{\text{defo,broad}}$, $\delta\phi^{\text{atm}}$, and $\delta\phi^{\text{orb}}$) because these points have a large radius of the used 30 PS points (Figure 3.6).

The estimated measuring error of an individual PS point represent a limit of a detectable amount of deformation from a measurement at a PS point. These results indicate that the shorter wavelength like C- and X-band is more suitable for infrastructure monitoring which needs pointwise information of deformation.

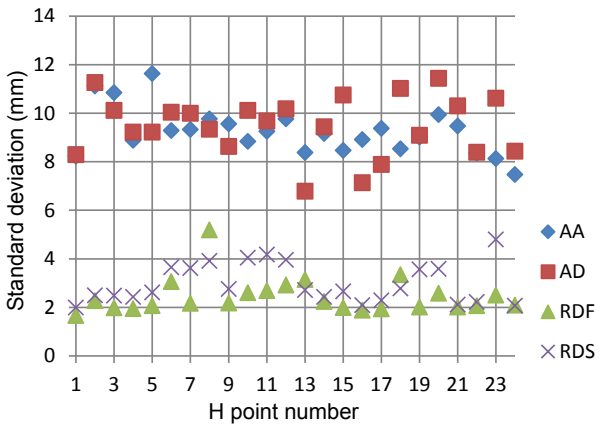

Figure 3.7: Phase standard deviations of PS points around each H point.

3.3.4 Measuring accuracy of spatially averaged PS points

Measurement accuracy of PSI is estimated by comparing with the results of GNSS at H points. Here I have averaged the deformation at 30 PS points around each H point as the deformation observed by PSI, in order to evaluate a capability of detecting deformation with some spatial extent, and compared with the projection of the GNSS three dimensional deformation onto the LOS direction. A root mean square error (RMSE) between PSI and GNSS represents the error of PSI if GNSS has no error. In reality, GNSS also has some errors, so the RMSE is regarded as the maximum of the error of PSI.

Figure 3.8 shows that the computed RMSE are approximately 4-6 mm except for the RDS data set, independent to the wavelengths, at 13th-22th H points which are located within 10 km from the reference point (23th H point). At farther H points from the reference (1st-12th), the RMSE tend to increase. This is probably because the farther points are affected by noises with long wavelength such as atmospheric noises. The reason why the only RDS data set shows a different pattern is the PSI

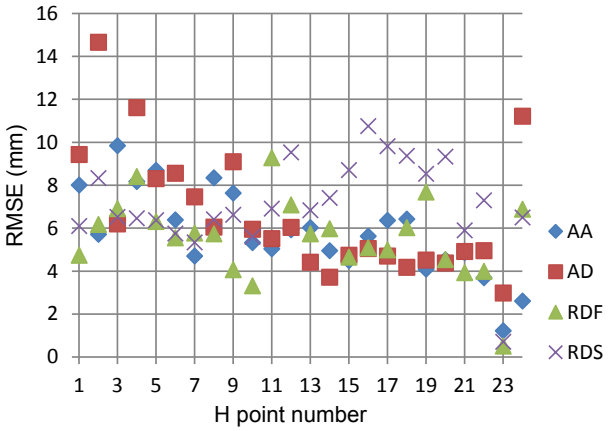

Figure 3.8: RMSE of LOS displacement between PSI observations and GNSS observations at each H point.

result at the reference is contaminated by some noises, for the radius of used 30 PS points is relatively large (~ 600 m) at the reference point (23th) according to Figure 3.6.

In the comparison of the mean LOS velocity between PSI and GNSS, all data sets except AA show high correlation (Figure 3.9, Table 3.3). The low correlation of the AA data set is due to small LOS displacement resulting from the opposite viewing direction to the others' (Section 3.3.1). The RMSE are approximately 2 mm/yr except for RDS data set, and the L-band is comparable to the C-band. The reason why the RMSE of the RDS data set is large is also probably caused by the noises at the reference point, as mentioned above. Consequently, spatially averaging neighboring PS points can reduce noises of individual PS points even for L-band, and L-band is suitable for detecting deformation with some spatial extent, also from the view point of achievable density of PS points (Section 3.3.2).

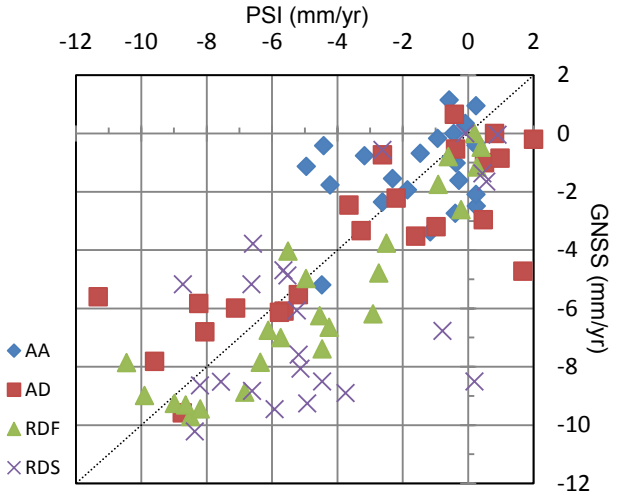

Figure 3.9: Correlations of mean LOS velocity between PSI observations and GNSS observations.

Table 3.3: Correlation coefficients and RMSE of mean LOS velocity between PSI observations and GNSS observations.

Data set	**AA**	**AD**	**RDF**	**RDS**
Correlation coefficient	0.34	0.84	0.92	0.64
RMSE (mm/yr)	1.80	2.29	1.63	3.43

3.4 Conclusions

PSI results of different radar wavelengths were compared; L- and C-band. Density of identified PS points depends on spatial resolution of the used data in urban areas. L-band has a better capability to detect PS points in vegetated areas than C-band. Measuring precision of an individual PS point is 8-11 mm for L-band and 2-3 mm for C-band, almost proportional to the wavelength. This suggests that the shorter wavelength is more suitable for pointwise usage such as infrastructure monitoring. Measuring accuracy of spatially averaged 30 PS points are 4-6 mm and approximately 2 mm/yr, being independent of wavelength, according to the comparison with continuous GNSS observation results. This implies that L-band has a

comparable capability of detecting spatially distributed deformation to C-band.

Chapter 4

Subsidence over pasture on drained peat soils

4.1 Mechanism of shallow subsidence of peat soils

In some countries, peat forms a major soil type for dairy farming and is therefore economically valuable (Montanarella et al., 2006). Peat is composed of organic materials which oxidize and emits greenhouse gases such as CO_2 and methane when exposed to the air (Bartlett and Harriss, 1993; van Huissteden et al., 2006). Oxidation of peat soils results in volume reduction and subsequent subsidence. As a result, a thickness of a vadose zone decreases, as a land surface gets closer to a phreatic zone or groundwater level. Consequently, to keep the land sufficiently dry for agricultural use, the soil needs to be drained, resulting in an increased vadose zone thickness, in

more oxidation, and therefore more subsidence (Schothorst, 1977; Hoogland et al., 2012). This loop is bound to continue until the peat soils have disappeared completely.

4.2 Drained peat soils in the Netherlands

In the Netherlands, peat soils cover approximately 2800 km^2, almost 10% of the total land area (Figure 4.1). Most soils are drained, fertilized and used as pasture land for agriculture (also called peat meadow). About 30% of the pastures in the Netherlands is situated on drained peat soils (Langeveld et al., 1997).

Along with sea level rise and tectonic subsidence, one-third of the land in the Netherlands is situated below sea level (Hoogland et al., 2012). Global warming will accelerate the sea level rise and peat oxidation, resulting in more subsidence and increased flooding risks. Water management is important to control peat oxidation, leading to delay or stop of subsidence. However drainage is required for agricultural use, hence it is a difficult trade-off problem. Accurate deformation data of subsidence would greatly contribute to optimize the water management solution.

Peat soils are also subject to reversible elastic volume changes because of fluctuations in groundwater levels between summer and winter, which causes annual vertical displacement (Schothorst, 1977; Nieuwenhuis and Schokking, 1997).

4.3 Past studies

Measuring subsidence rates in pasture on drained peat soils is difficult with conventional geodetic means as soft soils make it impossible to install fixed benchmarks

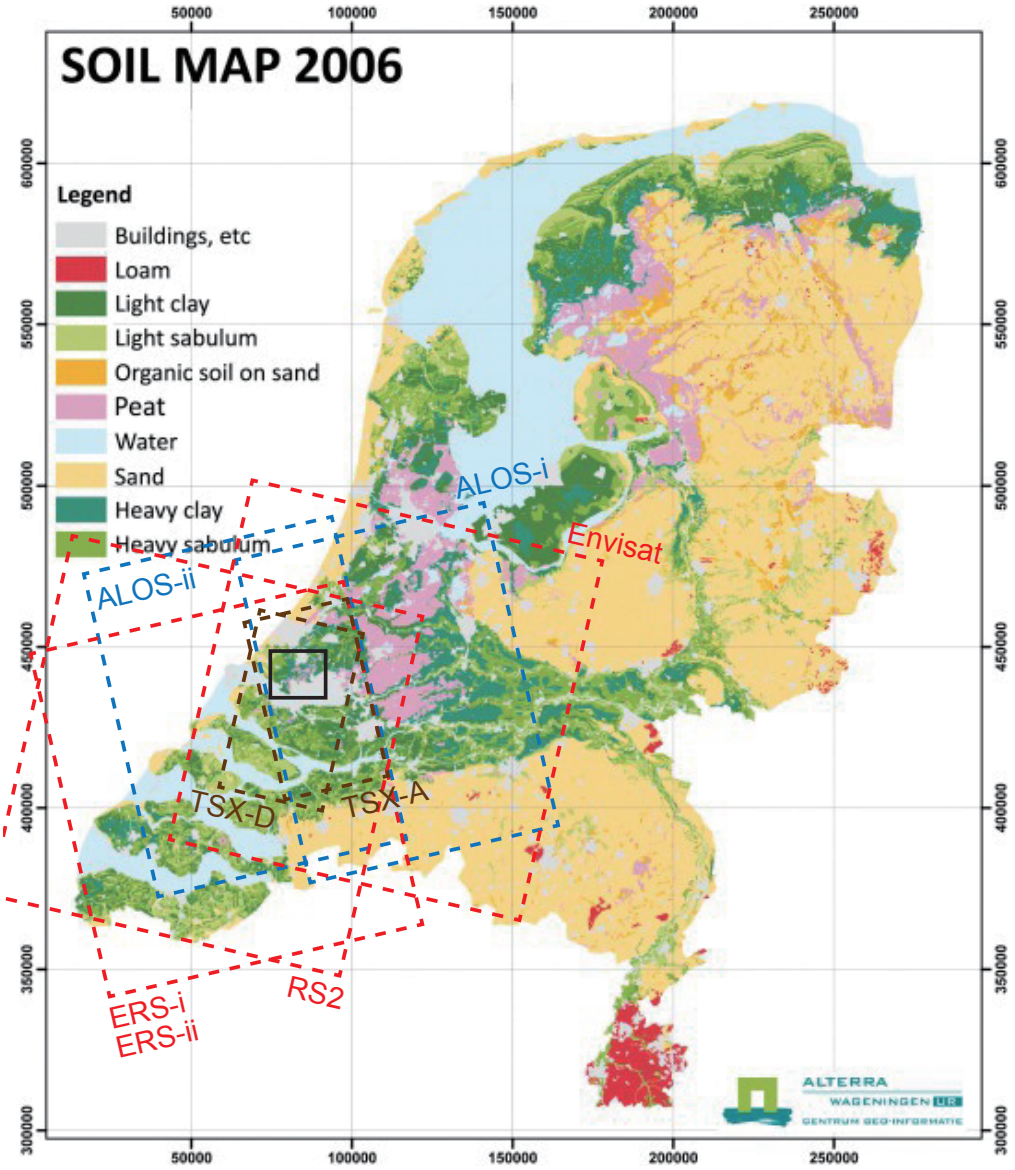

Figure 4.1: Soil map of the Netherlands (back ground image from Wageningen UR (2006)). Solid black lines and dashed lines indicate the target area (Section 4.4) and coverage of used SAR data (Table 4.1) in this thesis, respectively.

for repeated surveying. Soil subsidence rates in these areas have been estimated to range between extremes of 2 and 51 mm/yr, with common values between 5 and 15 mm/yr (van Huissteden et al., 2006). These values, however, are not reliable and based on models or incidental measurements. Although Hoogland et al. (2012) pre-

sented a subsidence model in a polder on peat soils near Amsterdam in the Netherlands, inputs of the model, peat thickness derived from soil surveys and elevation data measured by leveling and airborne lidar, suffer from large measurement errors. Nieuwenhuis and Schokking (1997) estimated subsidence rates in drained peat areas of the Province of Friesland, northern part of the Netherlands. However, the used leveling data were spatially limited along particular utility lines. Moreover, as the observed seasons of leveling are hardly unknown, unconsidered annual vertical fluctuations of the ground badly affect the estimated subsidence rates.

InSAR is a solution to monitor the subsidence successfully because fixed ground control points need not be installed. However, there is a critical problem; temporal decorrelation. Conventional InSAR techniques cannot obtain adequate coherence due to the very fast temporal decorrelation over pasture.

Cuenca and Hanssen (2007) studied displacement in the western part of the Netherlands by PSI from 1992 to 2005. Annual fluctuations with the amplitude of about 3 mm were detected in peat meadow areas; the ground surface gets highest at 23 August, delayed 1–2 months with respect to the ground water level fluctuations. The estimated subsidence rate of about 2 mm/yr is smaller than expected by other previous studies. A possible cause of the underestimation is that scatterers detected as PS are mainly man-made structures, which have deep foundations reaching to a stable layer to avoid subsidence (Figure 4.2). This implies PSI is not suitable to detect shallow subsidence of peat soils.

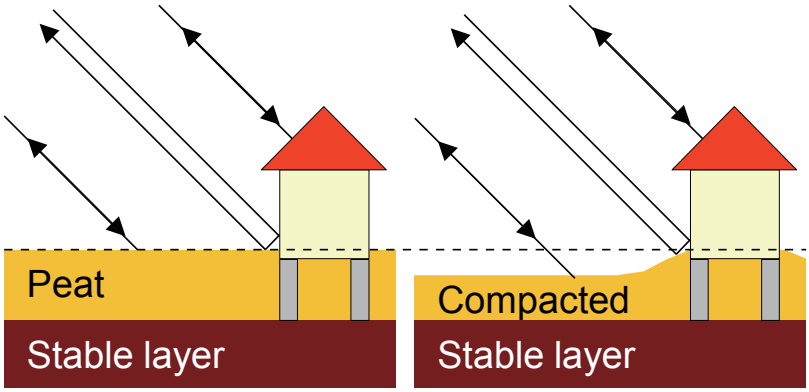

Figure 4.2: Possible cause of underestimated displacement of PSI.

4.4 Target area

A 16 km × 13 km area south of Delft, the Netherlands, is the target area in this study (Figure 4.3). The center of the area is widely covered with pasture (Figure 4.4). In order to distinguish the pasture area from the other types of land coverage, Normalized Difference Vegetation Index (NDVI) derived from Moderate Resolution Imaging Spectroradiometer (MODIS) is used (Huete et al., 2002). The NDVI indicates a concentration of green plants; the higher it is, the denser the vegetation is. Figure 4.5 shows the average of NDVI from 2003 to 2011, whose spatial resolution is 250×250 m and temporal resolution is 16 days. The area where the NDVI is higher than 0.7 is regarded to be pasture, consistent with visible classification according to the aerial photography (Figure 4.3). This area is selected as the target because there are plenty of SAR data acquired by different satellites with different wavelengths (Table 4.1).

Table 4.1: Used data sets in this thesis

Satellite	ALOS		ERS-1 (Ice Phase)		Envisat
Subscript	i	ii	i	ii	–
λ (mm) [a]	236	236	56	56	56
dt (day) [b]	46	46	3	3	35
B_{crit} (m) [c]	7000 (FBD[g]) / 14000 (FBS[h])		1100	1100	1100
$\rho_{\text{gr}} \times \rho_{\text{azi}}$ (m) [d]	17×4 (FBD) / 9×4 (FBS)		23×5	23×5	23×5
N/L [e]	2.86 (FBD) / 1.43 (FBS)		1.49	1.49	1.51
Flight direction	Ascending	Ascending	Ascending	Ascending	Descending
θ (deg) [f]	37.0	39.2	25.0	25.0	24.3
Path number	650	651	15	15	423
Polarimetry	HH	HH	VV	VV	VV
Start date	2007/03/05	2006/12/20	1992/01/29	1993/12/25	2003/02/12
End date	2011/03/16	2011/02/15	1992/03/29	1994/04/09	2010/10/13
# of scenes	10 (FBD) 11 (FBS)	10 (FBD) 11 (FBS)	20	34	75

Satellite	RS2 (RADARSAT-2)		TSX (TerraSAR-X)	
Subscript	HH	HV	A	D
λ (mm)	56	56	31	31
dt (day)	24	24	11	11
B_{crit} (m)	1300	1300	5400	3800
$\rho_{\text{gr}} \times \rho_{\text{azi}}$ (m)	24×7	24×7	2.5×2.5	2.5×2.5
N/L	1.64	1.64	1.51	1.63
Flight direction	Descending	Descending	Ascending	Descending
θ (deg)	32.7	32.7	39.0	24.0
Path number	102	102	25	48
Polarimetry	HH	HV	HH	HH
Start date	2010/06/13	2010/07/31	2009/04/06	2009/04/08
End date	2012/06/02	2012/06/02	2012/04/10	2012/04/12
# of Scenes	30	28	79	85

[a] Radar wavelength [b] Repeat interval [c] Critical baseline
[d] Spatial resolution of ground range × azimuth
[e] Oversampling ratio [f] Incidence angle at the center of the area
[g] Fine Beam Dual polarization [h] Fine Beam Single polarization

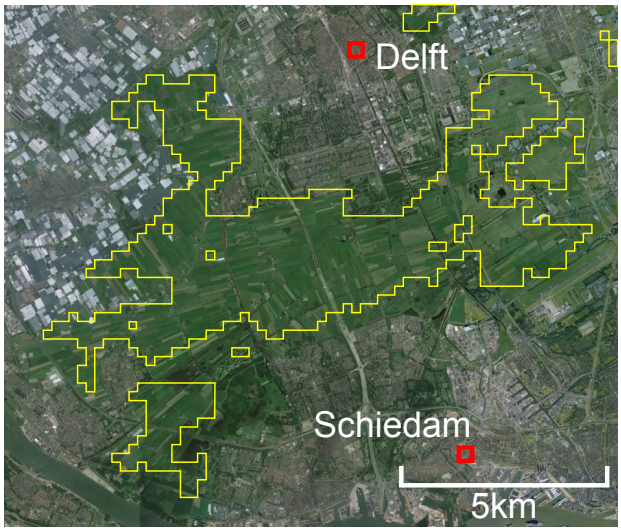

Figure 4.3: Target area (Image Google Earth). The yellow polygons indicate the boundary of pasture and the other types of land coverage based on NDVI (Figure 4.5). The green pasture delineated by the polygon is clearly visible between the cities of Delft and Schiedam (red squares), to the north and the south of the area, respectively.

Figure 4.4: Ground view of the pasture area, showing the drainage canals and the approximate depth of the vadose zone.

4.5 Results of InSAR and PSI

I processed interferograms with various time intervals and wavelengths (Figure 4.6). Although interferograms with the shortest time interval (left column) show coherent differential phases all over the area except water surfaces, coherence is

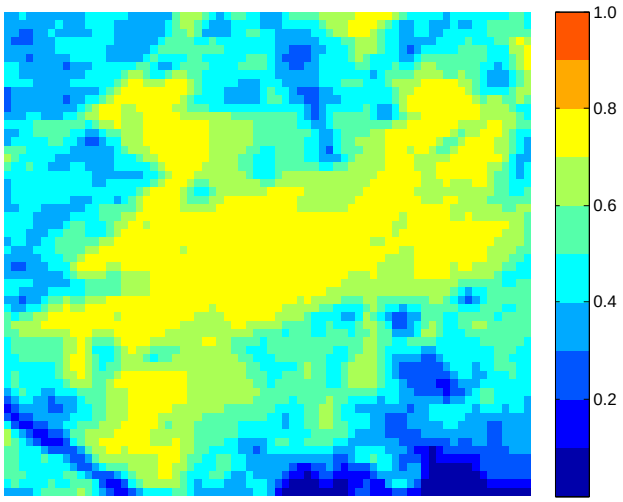

Figure 4.5: Averaged NDVI in the target area, with a similar crop as in Figure 4.3. The areas where the NDVI is 0.7 or higher are regarded as the pasture area in this thesis.

rapidly lost with time in the pasture area even in L-band. This means that temporal decorrelation is quite severe and conventional InSAR is unable to provide a significant signal of the long term subsidence.

I also applied InSAR time series analysis using StaMPS/MTI software (Hooper et al., 2007; Fukushima, 2010). Figure 4.7 shows the results of PSI, clearly showing that it is not possible to retrieve deformation estimates in the pasture area using PSI for any bands, due to the absence of long-term coherent scatterers. Only lineated features related to buildings are visible, but due to their particularly deep foundations, these may not be representative of the shallow subsidence in the peat areas as mentioned in Section 4.3 (Cuenca and Hanssen, 2007). Furthermore, the results of SBAS approach and combined approach of PSI and SBAS by StaMPS/MTI (Hooper, 2008) showed insignificant improvement in terms of distribution of PS in the pasture area.

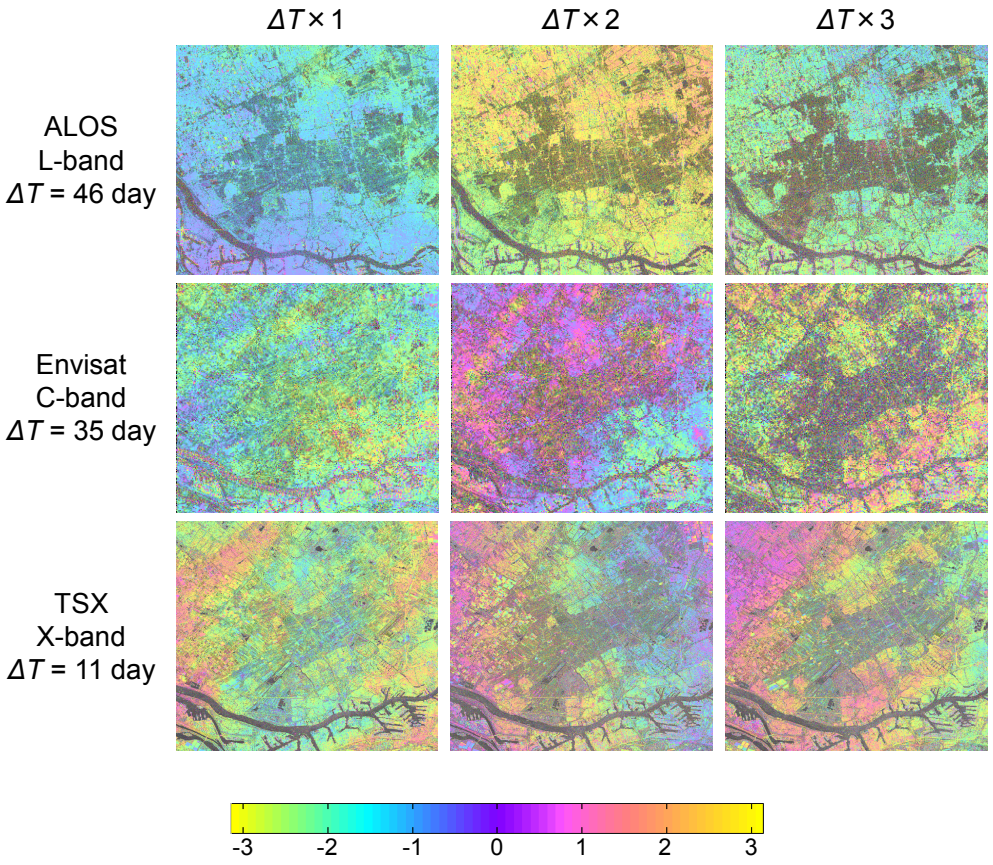

Figure 4.6: Interferograms with different time intervals and wavelengths (rad, wrapped, radar coordinate). Interferograms with the shortest time interval (left column) show coherent differential phases all over the area except water surfaces. Coherence is rapidly lost in the pasture area as the time interval increases for every wavelength, while adequate coherence is kept in the surrounding urban area.

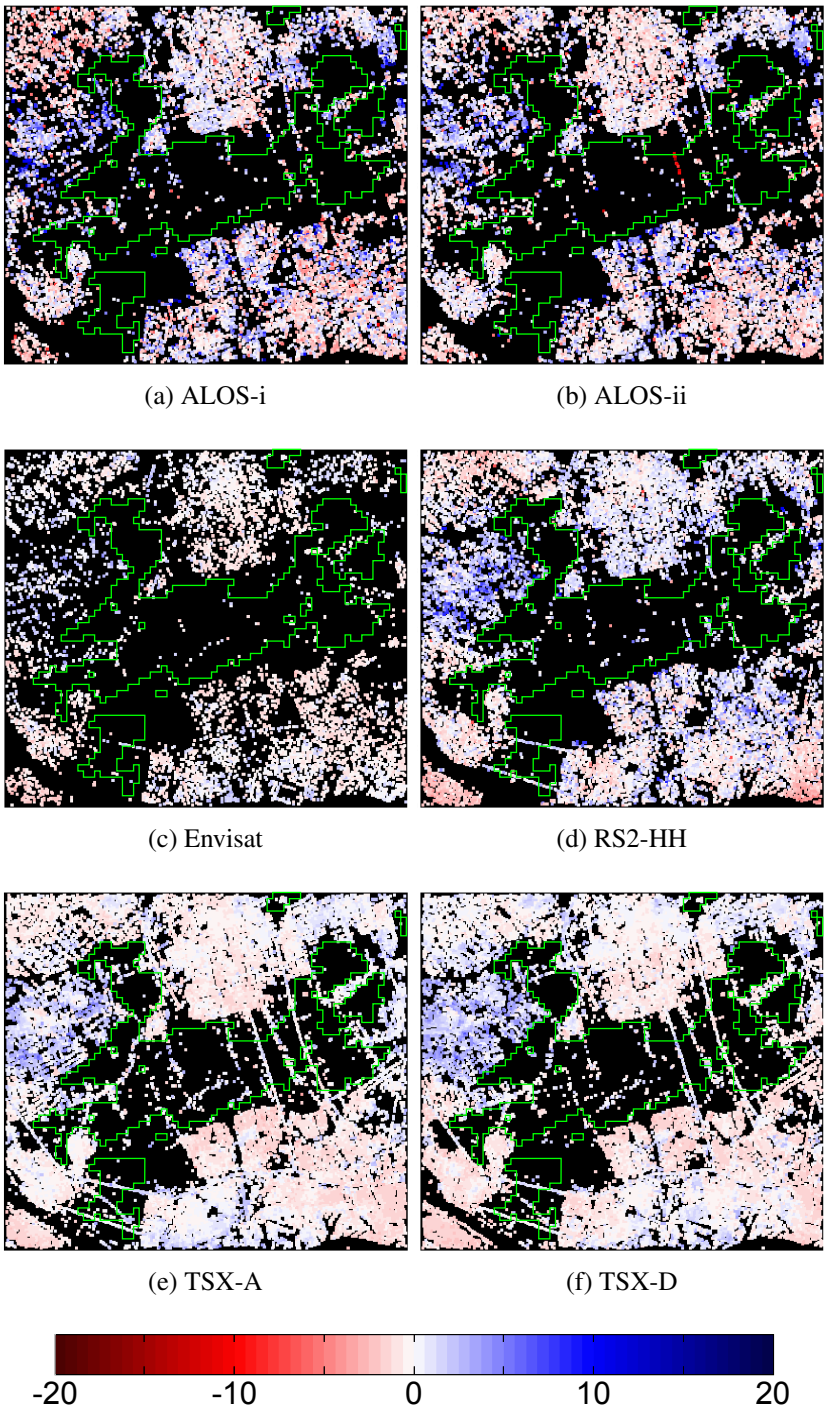

(a) ALOS-i (b) ALOS-ii

(c) Envisat (d) RS2-HH

(e) TSX-A (f) TSX-D

Figure 4.7: LOS velocity (mm/yr) estimated by PSI. Positive values mean subsidence. The center of the area delineated by the polygon with few PS corresponds to the pasture. While the middle west part (greenhouse area) shows slight subsidence, no significant deformation is detected in the other area.

Chapter 5

Quantitative assessment of temporal decorrelation in L-, C-, and X-band

Paper was published in *IEEE Transactions on Geoscience and Remote Sensing*

Morishita, Y. and R. F. Hanssen, 2015: Temporal Decorrelation in L-, C- and X-band Satellite Radar Interferometry for Pasture on Drained Peat Soils, *IEEE Trans. Geosci. Remote Sens.*, 53(2), 1096-1104, doi:10.1109/TGRS.2014.2333814.

5.1 Introduction

As shown in Section 4.5, temporal decorrelation is the main problem for InSAR measurements over pasture land. From a radar perspective, pasture land consists of distributed scatterers (DS) (Bamler and Hartl, 1998), from which interferometric information can be obtained —if necessary after multilooking— unless the area is decorrelated completely. In other words, DS can be exploited only if the minimum temporal sampling interval, i.e., repeat orbit, is significantly shorter than the decorrelation time. The decorrelation time depends on the wavelength of the radar and on the reflective characteristics of the area (Zebker and Villasenor, 1992).

For the last 25 years, spaceborne L-, C- and X-band SAR data have shown that temporal decorrelation increases with higher frequencies (Rosen et al., 1996; Parizzi et al., 2009; Wei and Sandwell, 2010). However, parameters of a generic temporal decorrelation model are unknown because properties of scatterers vary widely depending on the land use and the vegetation type. In order to estimate detectability of surface deformation using past, present and future satellites, it is important to assess the temporal decorrelation quantitatively, for the specific class of the land use. Here I analyze the temporal decorrelation in a peat meadow using data of ALOS, European Remote-Sensing Satellite 1 (ERS-1), Environmental Satellite (Envisat), RADARSAT-2 (RS2) and TerraSAR-X (TSX), which have different wavelengths and/or temporal sampling intervals.

First, a general concept of coherence is briefly described in Section 5.2. In Section 5.3, an advanced model for the temporal decorrelation is presented, using three specific parameters. The parameters are empirically estimated in Section 5.4 for all available satellite SAR sensors in the target area, followed by conclusions in Section 5.5.

5.2 Coherence

Coherence is used as a measure of similarity of phases between two SAR images forming a interferogram. Complex coherence γ between two complex stochastic values y_1 and y_2 at the same location in two coregistered SAR images is defined as

$$\gamma = \frac{E\{y_1 y_2^*\}}{\sqrt{E\{|y_1|^2\}E\{|y_2|^2\}}}, \tag{5.1}$$

where $E\{\cdot\}$ is the expectation operator and y_2^* is the complex conjugate of y_2 (Bamler and Hartl, 1998; Hanssen, 2001). It is not possible to calculate γ per pixel, as there is only one observed value y_1 and y_2 per pixel in the respective images, and therefore their expectations are not known. Alternatively, coherence estimator $\hat{\gamma}$ is calculated under the assumption of ergodicity by spatially averaging over N neighboring pixels,

$$\hat{\gamma} = |\hat{\gamma}|e^{i\hat{\phi}} = \frac{\sum_{n=1}^{N} y_{1n} y_{2n}^*}{\sqrt{\sum_{n=1}^{N} |y_{1n}|^2 \sum_{n=1}^{N} |y_{2n}|^2}}, \tag{5.2}$$

where $\hat{\phi}$ is corresponding to a multilooked differential phase. Practically, the absolute value $|\hat{\gamma}|$ is often used and simply referred to as coherence. In this thesis, I also use *coherence* as the absolute coherence estimator $|\hat{\gamma}|$, while *theoretical coherence* as the

original absolute coherence $|\gamma|$. The coherence ranges between 0 and 1, where a higher value denotes higher correlation, i.e., the phase is coherent and precise. If the coherence is used as a criterion for detectability of surface displacement, a systematic (linear) phase component ϕ_n in a estimation window should be removed by

$$|\hat{\gamma}| = \frac{|\sum_{n=1}^{N} y_{1n} y_{2n}^{*} \exp(-j\phi_n)|}{\sqrt{\sum_{n=1}^{N} |y_{1n}|^2 \sum_{n=1}^{N} |y_{2n}|^2}}. \tag{5.3}$$

Note that the estimated coherence has a bias with respect to the theoretical coherence. The expectation and the variance of the coherence are derived as

$$E\{|\hat{\gamma}|\} = \frac{\Gamma(L)\Gamma(3/2)}{\Gamma(L+1/2)} \, {}_3F_2(3/2, L, L; L+1/2, 1; |\gamma|^2)(1-|\gamma|^2)^L \tag{5.4}$$

and

$$\sigma^2_{|\hat{\gamma}|} = \left[\frac{\Gamma(L)\Gamma(2)}{\Gamma(L+1)} \, {}_3F_2(2, L, L; L+1, 1; |\gamma|^2)(1-|\gamma|^2)^L\right] - E\{|\hat{\gamma}|\}^2, \tag{5.5}$$

respectively, where $\Gamma(\cdot)$ is the Gamma function, ${}_pF_q(a; b; z)$ is the Generalized hypergeometric function and L is the number of independent samples (Touzi et al., 1999; Hanssen, 2001). Figure 5.1 shows that the lower the theoretical coherence value, the greater the bias is. Larger L, i.e., using a larger coherence estimation window reduces the bias and the variance of the coherence at the expense of resolution. Note that L is lower than N because a resolution cell is generally larger than a pixel in an image due to oversampling of SAR images (Hanssen, 2001). The ratio N/L is given by

$$N/L = \frac{\rho_{\text{azi}}}{\Delta_{\text{azi}}} \times \frac{\rho_{\text{gr}}}{\Delta_{\text{gr}}}, \tag{5.6}$$

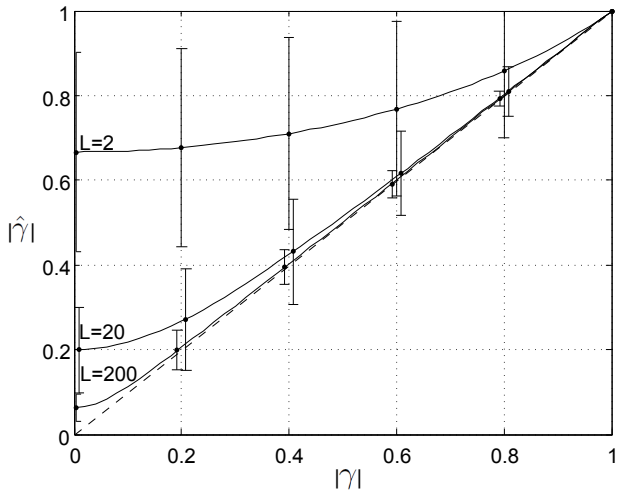

Figure 5.1: Expectation of coherence $|\hat{\gamma}|$ as a function of theoretical coherence $|\gamma|$ and the number of independent samples L. Error bars denote the standard deviation of the coherence $\sigma_{|\hat{\gamma}|}$.

where ρ_{azi} and ρ_{gr} are the spatial resolution of azimuth and ground range, and Δ_{azi} and Δ_{gr} are pixel spacing of azimuth and ground range, respectively (Swart, 2000; Laur et al., 2002). For example, N/L for ERS is approximately 1.5 (Table 4.1). Since resolution is inversely proportional to bandwidth, applying spectral filtering reduces the resolution (Gatelli et al., 1994).

Decorrelation is induced by several sources, such as spatial decorrelation γ_{spat}, volume decorrelation γ_{vol}, thermal noise γ_{therm}, processing errors γ_{proc}, and temporal decorrelation γ_{temp} (Zebker and Villasenor, 1992; Hanssen, 2001). Since these decorrelation sources are multiplicative, the total coherence is given by

$$|\gamma| = \gamma_{\text{spat}} \cdot \gamma_{\text{vol}} \cdot \gamma_{\text{therm}} \cdot \gamma_{\text{proc}} \cdot \gamma_{\text{temp}}. \tag{5.7}$$

The objective of this chapter is a quantitative assessment of the temporal decorrelation. Hence, the other decorrelation sources need to be excluded from the calculated

coherence. The spatial decorrelation is small if the perpendicular baseline of the interferometric pair is short and spectral filtering is applied. Since our target area is pasture with no trees, the volume decorrelation is assumed to be negligible. γ_{therm} is greater than 0.99 for all sensors used in this thesis according to their reported Noise Equivalent Sigma Zero values (NESZ). γ_{proc}, mainly caused by interpolation (resampling) and coregistration inaccuracies, is considered greater than 0.95 by applying an appropriate interpolation kernel and with better coregistration accuracy than 0.1 resolution cell (Hanssen, 2001). Consequently, the contribution of these decorrelation components is considered to be relatively small compared to the temporal decorrelation component.

5.3 Temporal decorrelation model

Temporal decorrelation results from changing physical properties of scatterers between acquisitions. Sudden and complete changes, e.g., due to cultivation or snow fall, are impossible to model. Therefore I assume that there are only gradual and natural changes. If motions of all scatterers in a resolution cell are independent and equally distributed, the temporal decorrelation can be expressed by

$$\gamma_{\text{temp}} = \exp\left(-\frac{1}{2}\left(\frac{4\pi}{\lambda}\right)^2 \sigma_r^2\right), \tag{5.8}$$

where λ is the radar wavelength and σ_r^2 is the variance of the motion of the scatterers along LOS (Zebker and Villasenor, 1992; Rocca, 2007; Lavalle et al., 2012). Whereas σ_r is zero if the two acquisitions are co-instantaneous, it would be nonzero due to, e.g., perturbation by wind if there is a time lag of even a few seconds (Lavalle

et al., 2012). Additionally, the variance smoothly increases with time because of vegetation growth (Rocca, 2007). Then I assume that the variance has two components; a near-instantaneous short term component $\sigma_{r,\mathrm{short}}$ (mm) and a time dependent long term component $\sigma_{r,\mathrm{long}}$ (mm $\cdot$ day$^{-1/2}$),

$$\sigma_r^2 = \sigma_{r,\mathrm{short}}^2 + \sigma_{r,\mathrm{long}}^2 \cdot t. \tag{5.9}$$

$\sigma_{r,\mathrm{long}}$ becomes a dominant source of the temporal decorrelation as time goes on, whereas $\sigma_{r,\mathrm{short}}$ is dominant only for a very short time interval. Since the time interval is three days or longer for repeat pass spaceborne SAR used in this study, I focus only on the long term component. From Equations (5.8) and (5.9), I obtain

$$\gamma_{\mathrm{temp}}(t) = \gamma_{t\_\mathrm{short}} \cdot e^{-t/\tau}, \text{ with} \tag{5.10}$$

$$\gamma_{t\_\mathrm{short}} = \exp\left(-\frac{1}{2}\left(\frac{4\pi}{\lambda}\right)^2 \sigma_{r,\mathrm{short}}^2\right), \text{ and} \tag{5.11}$$

$$\tau = \frac{2}{\sigma_{r,\mathrm{long}}^2}\left(\frac{\lambda}{4\pi}\right)^2, \tag{5.12}$$

where I refer to τ as *decorrelation rate*. Equation (5.12) implies that τ is proportional to λ^2, which means that τ for L-band would be 18 times larger than τ for C-band, and τ for C-band would be three times larger than τ for X-band.

As a model for the total coherence, in combination with the other decorrelation sources, I use

$$|\gamma|(t) = \gamma_0 \cdot e^{-t/\tau}, \tag{5.13}$$

where γ_0 is *initial coherence*, defined as

$$\gamma_0 = \gamma_{\text{others}} \cdot \gamma_{t\_\text{short}}, \text{ with} \tag{5.14}$$

$$\gamma_{\text{others}} = \gamma_{\text{spat}} \cdot \gamma_{\text{vol}} \cdot \gamma_{\text{therm}} \cdot \gamma_{\text{proc}}. \tag{5.15}$$

Note that this model is not for the coherence estimator $\hat{\gamma}$ but for the theoretical coherence. As zero coherence will never be observed even in a completely decorrelated area due to (i) the bias in the coherence mentioned in the previous section, and (ii) a possibility of presence of persistent dominant point scatterers in the coherence estimation windows, I modify the temporal decorrelation model Equation (5.13) to

$$|\hat{\gamma}|(t) = (\gamma_0 - \gamma_\infty)e^{-t/\tau} + \gamma_\infty, \tag{5.16}$$

following Parizzi et al. (2009), where *long term coherence* γ_∞, representing the minimum attainable coherence value, or the value to which observed coherence will converge over time, is introduced. Whereas τ in Equation (5.13) is the time for the coherence to drop down to $1/e$ of its initial value, τ in Equation (5.16) is its equivalent for $|\hat{\gamma}| - \gamma_\infty$. This means that not only γ_0 and τ but also γ_∞ need to be taken into account when the temporal decorrelation behavior is discussed. In the following I will estimate and analyze these parameters.

5.4 Parameter estimation at target area

5.4.1 Preliminary parameter estimation

Nine data sets with three different frequency bands are available in the target area (Table 4.1). All images were coregistered to a single master image per data set. Since Envisat and TSX have a large number of images (> 70), interferometric pairs with a longer time interval than 400 days for Envisat and 100 days for TSX were not processed. In order to mitigate the effect of the spatial decorrelation, spectral filtering was applied in both range and azimuth (Gatelli et al., 1994). Then, topographic phase components at every pixel for all interferograms were computed from SRTM DEM and geocoding was implemented. These processing steps were performed using Delft object-oriented radar interferometric software (Doris) (Kampes et al., 2003).

Coherence estimation windows were defined based on geographical coordinates, rather than common radar coordinates, to ensure the same location of the computed coherence values among different data sets; the location of the windows are geographically the same among different data sets (Figure 5.2). To detect subtle changes of low coherence, bias of the coherence must be small, hence, size of the coherence estimation windows should be large enough. Here I chose the minimum number of 300 independent samples per estimation window. Given the oversampling ratios (Table 4.1), for the poorest resolution (RS2), this is equivalent to about 500 pixels, or an area of about 230 m $\times$ 230 m. In this case the bias of the coherence is less than 0.06 which is small enough. By fixing this ground dimension of the window (instead of the amount of samples per window) it is guaranteed that the coherence properties of

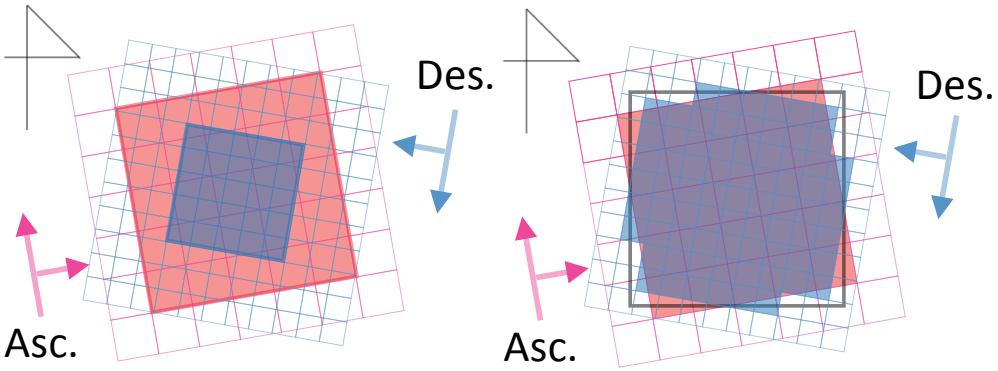

(a) Radar coordinates (b) Geographical coordinates

Figure 5.2: Example of configuration of coherence estimation window based on (a) radar coordinates (b) geographical coordinates. Red and blue grids represent pixel structure of a SAR image of ascending and descending, respectively, whose spatial resolution and orientation are different. Bold lines (red and blue in (a) and black in (b)) indicate frames of coherence estimation windows. Grids filled with color are pixels inside of the window. In the case of a common boxcar window based on radar coordinates (a), the areas covered by the windows are mismatched among different data sets because of different spatial resolution or orientation. Based on geographical coordinates (b), the locations of the pixels covered by the window are almost identical.

the same land area among different data sets is evaluated. Since RS2 has the poorest resolution, it is also guaranteed that the bias of the coherence is lower than 0.06 for the other data sets.

Figure 5.3 shows the calculated coherence which is the averaged value among all (nonoverlapping) coherence estimation windows over the pasture for all computed interferometric pairs. Diagonal elements have the coherence value of one as is obvious. While off-diagonal elements near the diagonal elements have relatively high values, there are very low values far from diagonal elements, which implies the coherence decreases with time.

Figure 5.4 is a different expression of Figure 5.3, clearly showing acquired seasons and time intervals. The coherence value is expressed by hue (color), whereas the ratio between the perpendicular baseline and the critical baseline ($B_{\perp}/B_{\mathrm{crit}}$) is

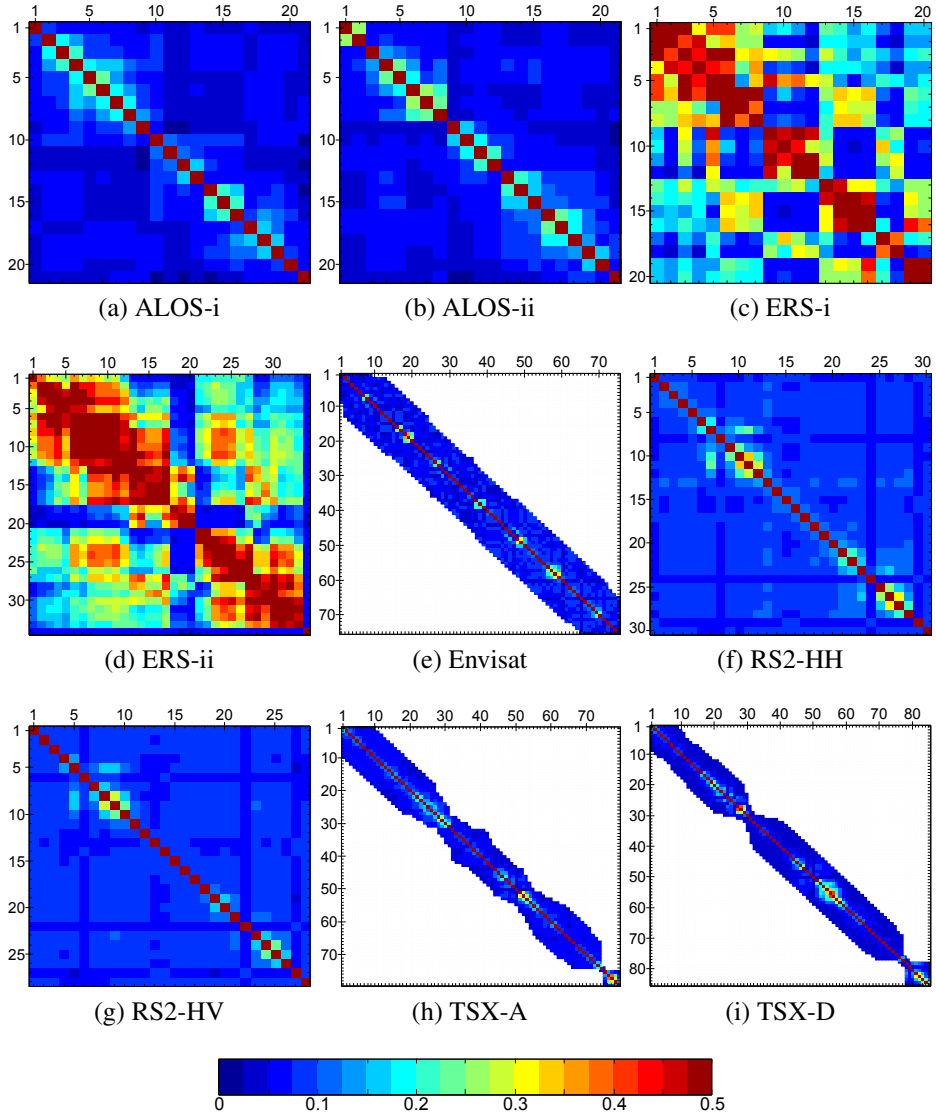

Figure 5.3: Coherence matrices in the pasture area. The numbers indicate the ordinal number of the acquisitions. Data are sorted by acquisition date. Diagonal elements have a value of one.

indicated by the brightness of the color. This helps in the interpretation, as interferograms with a large baseline ratio tend to have relatively low coherence due to spatial decorrelation even though the time interval is very short and spectral filtering is applied (Hanssen, 2001).

From the ERS 3-day repeat data sets (Figures 5.3(c)(d) and 5.4), it is evident that

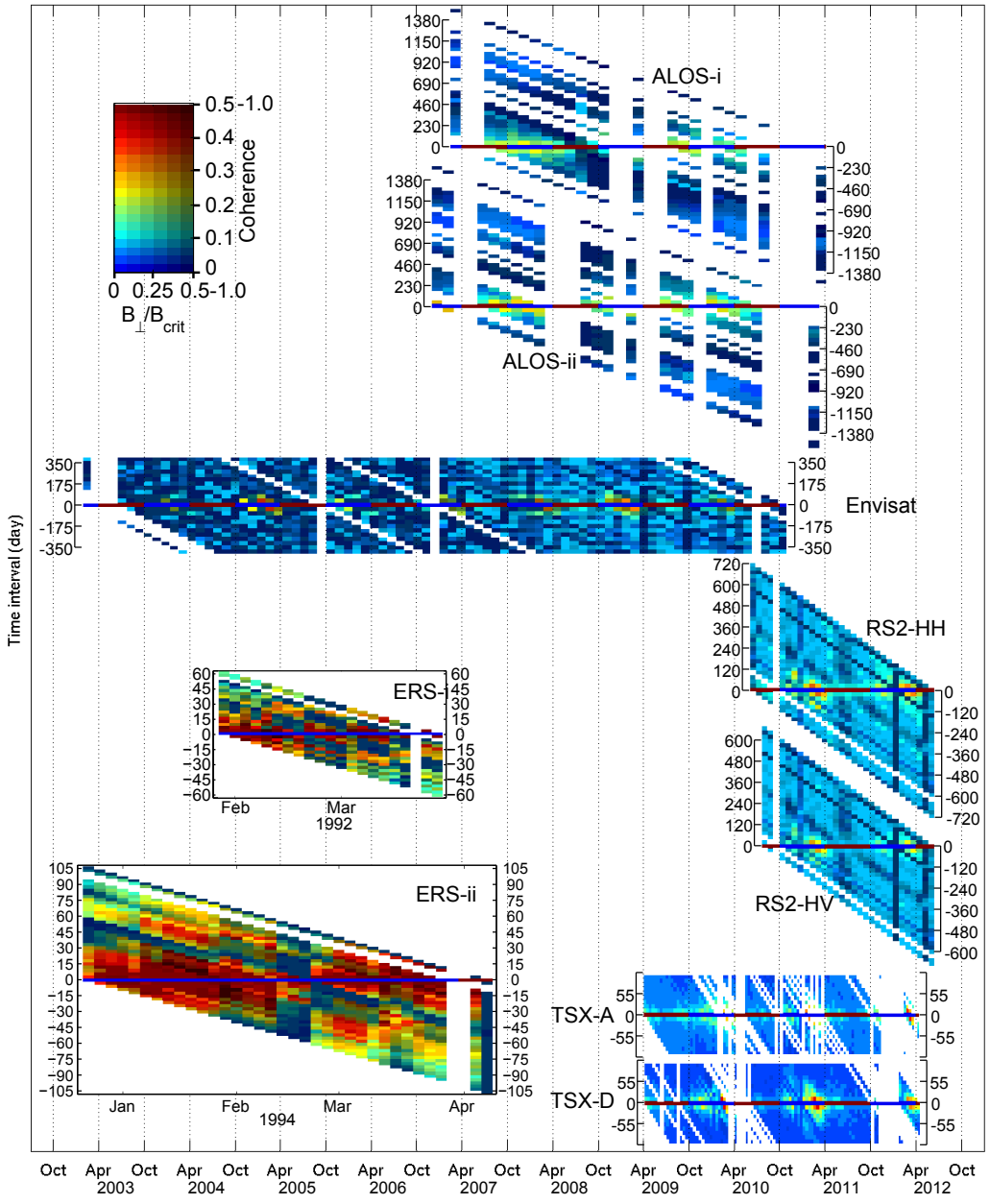

Figure 5.4: Calculated coherence in the pasture area. Hue and brightness represent the average of the coherence in the pasture area and the ratio between the perpendicular baseline and the critical baseline ($B_\perp/B_{\mathrm{crit}}$) of the interferogram, respectively. Note that the spectral filtering in range and azimuth has been applied. Colors on the horizontal axes ($dt = 0$) do not represent coherence but seasons (Apr-Sep: brown, Oct-Mar: blue).

the coherence decreases with time. For all data sets, interferograms only with a short time interval show a relatively high coherence, which implies that the scatterers in the pasture decorrelate quickly. Whereas L-band (ALOS) has adequate coherence throughout the year for a short time interval, C- and X-band (Envisat, RS2 and TSX) can obtain adequate coherence only during winter, with very low coherence during summer. Unfortunately, it is not possible to derive empirically whether a shorter repeat interval would yield a higher coherence using C-band during summer due to absence of 3-day repeat data during summer. In a comparison of polarimetry, RS2-HH shows slightly higher coherence than RS2-HV.

It seems that the temporal decorrelation behavior is not constant through the year but depends on seasons. I set up three data sets on the basis of acquisition date, i.e., 1) All dates, 2) Apr-Sep ('summer'), and 3) Oct-Mar ('winter') in order to compare seasonal effects. Interferograms with $B_\perp/B_{\mathrm{crit}} > 1/3$ were discarded to avoid the effect of spatial decorrelation. The two available data sets for ALOS, ERS and TSX, respectively, were integrated into one data set to make the parameter estimation more robust. Then, the three model parameters γ_0, γ_∞ and τ in Equation (5.16) were estimated for each data set at each coherence estimation window in a least-squares sense.

Figures 5.5 and 5.6 show maps of the estimated temporal decorrelation model parameters and the time dependency of the coherence for the ERS data set. It is clear that the temporal decorrelation behavior depends on the land use. An urban area (A) tends to have a higher γ_0 and γ_∞, whereas a pasture area (B) has a very low γ_∞, similar to a water area (C) where no coherent signal can be obtained. These indicate that the urban area can keep adequate coherence semipermanently, whereas the pasture

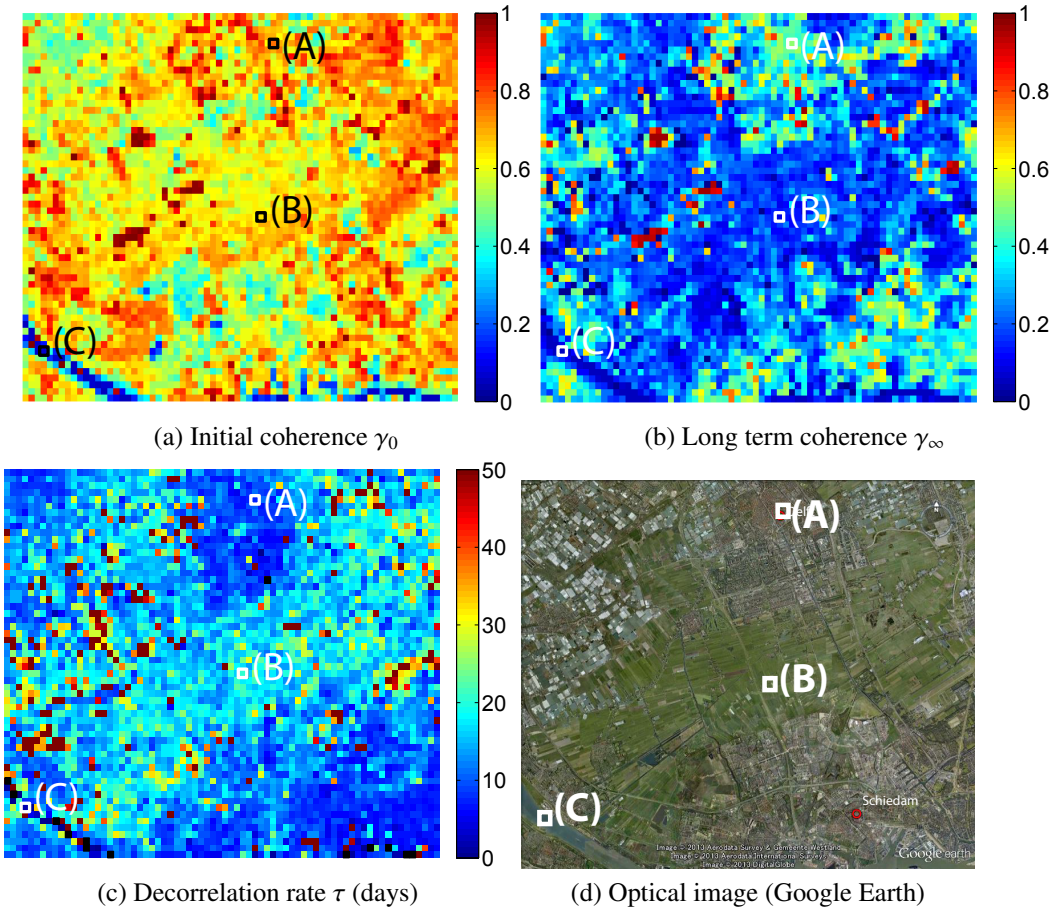

(a) Initial coherence γ_0

(b) Long term coherence γ_∞

(c) Decorrelation rate τ (days)

(d) Optical image (Google Earth)

Figure 5.5: Maps of the estimated temporal decorrelation model parameters γ_0, γ_∞ and τ for the ERS 3-day repeat data set. Areas (A), (B) and (C) indicate an urban area, pasture area, and water area, respectively.

area gets almost completely decorrelated sooner or later. An interpretation of decorrelation rate τ is less straightforward. In fact, τ can be shorter in an urban area than in a pasture area because γ_∞ remains very high in an urban area. Since the coherence in a pasture area decays exponentially (Figure 5.6 (B)), it seems that Equation (5.16) can adequately represent the temporal decorrelation behavior in the pasture area.

Figure 5.7 is a set of histograms of the estimated parameters in the pasture area. Seasonal dependence is seen in γ_0 and τ, not in γ_∞. γ_∞ only for ERS have higher peak (0.15 – 0.2) than the bias of the coherence (~0.05) because of the lack of the

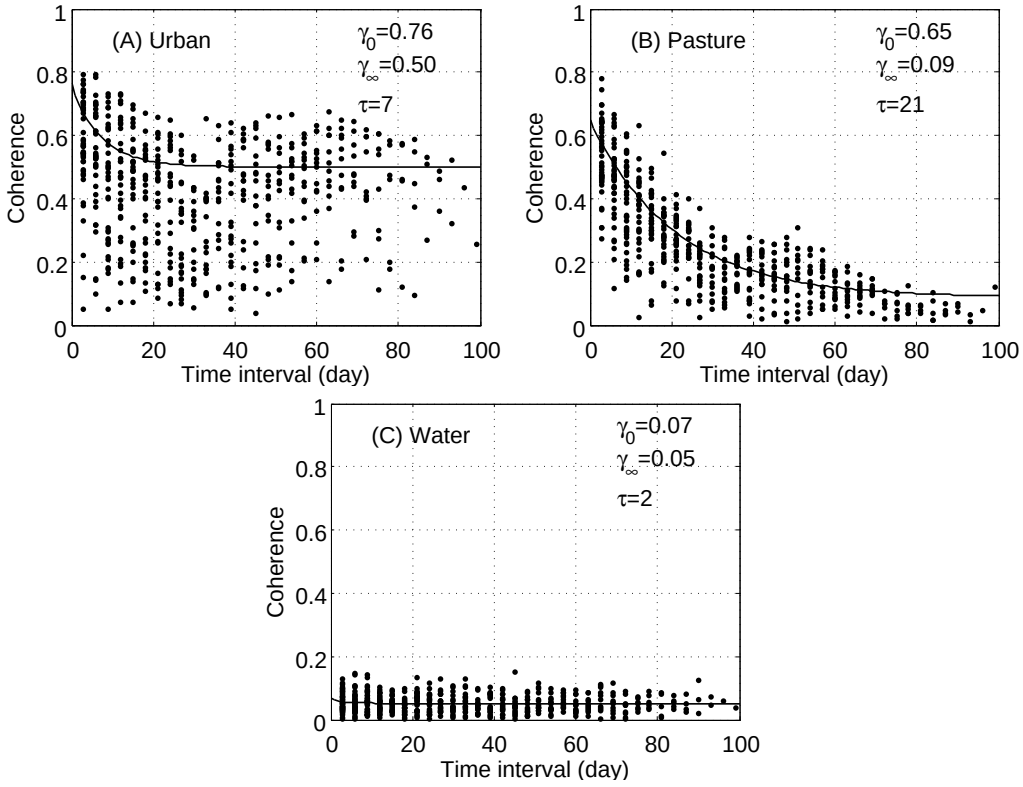

Figure 5.6: Estimated coherence (black dots) and time dependency of the estimated temporal decorrelation models (solid lines) at three different type of land use for the ERS data set. Locations of the points are plotted in Figure 5.5.

completely decorrelated interferograms, i.e., long time intervals. γ_∞ for the other satellites are almost equal to the bias of the coherence, implying the pasture area gets almost completely decorrelated regardless of seasons.

Figure 5.8 shows time dependency of the estimated temporal decorrelation model. One of the reasons why the coherence for C-band is higher than X-band is that the bias for C-band is larger than for X-band, resulting from the lower resolution of C-band. Therefore the magnitude of the coherence should not be solely focused on, but mainly on how it decays and converges. Since the pasture area seems to get decorrelated almost completely at a sufficiently long time interval, the speed of temporal

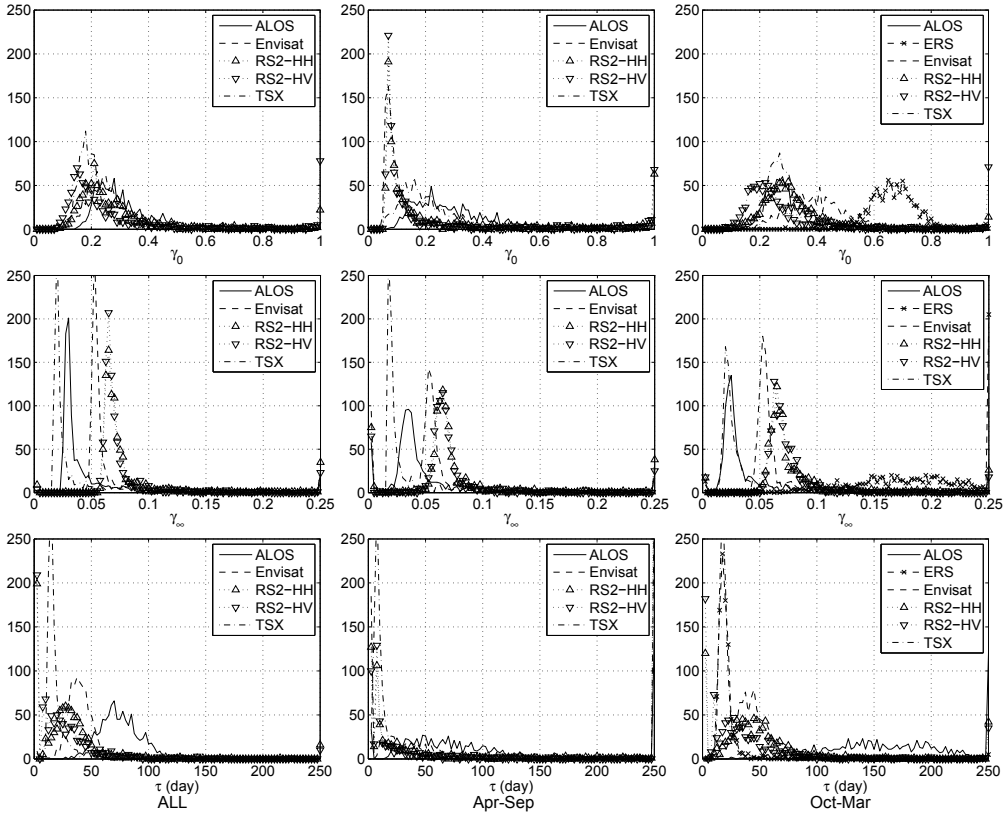

Figure 5.7: Histograms of the estimated parameters γ_0, γ_∞ and τ for the three time epochs in the three columns. Both γ_0 and τ tend to be higher during Oct-Mar than during ALL and Apr-Sep, which implies that the temporal decorrelation is slower in winter than in summer. The values of γ_∞ are comparable with the expected bias of the coherence and decrease with the resolution of the sensor. γ_0 seems to be underestimated for all data sets except ERS due to lack of the short time interval data whereas γ_0 for ERS is reasonable. Note that the ERS 3-day repeat data are only available during winter periods.

decorrelation can be simply evaluated by τ. ALOS has the longest τ and TSX the shortest, as expected (Figure 5.7). The winter months (Oct-Mar) show a larger γ_0 and τ compared with summer (Apr-Sep) and the entire year (ALL), which implies that the temporal decorrelation is slower in winter. During summer (Apr-Sep) I obtain almost a flat model for C-band (Figure 5.8 (Apr-Sep)) suggesting that a coherent interferogram with the repeat interval of Envisat and RS2 is never obtained. In terms of polarization, RS2-HH has a slightly larger γ_0 and τ than RS2-HV.

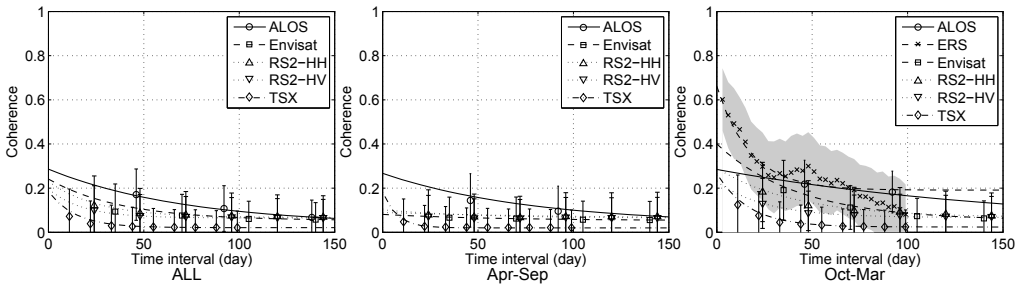

Figure 5.8: Time dependency of the coherence for each data set calculated from the median of the estimated temporal decorrelation model parameters in the pasture area. The symbols and error bars indicate the median and the standard deviation of the coherence at each time interval. To avoid clogging, a shadow region was used to indicate the standard deviations of the ERS data in Oct-Mar.

5.4.2 Approximating γ_0

From Figure 5.7 (Oct-Mar) it appears that only the 3-day ERS data shows reasonable initial coherence γ_0 of 0.5 – 0.8. All other satellites seem to significantly underestimate γ_0. This is mainly due to the lack of the short term interferometric combinations and the extrapolation to the zero day. Consequently, in order to estimate the temporal decorrelation behavior over time spans smaller than the repeat interval of the satellites, it is needed to approximate γ_0 via an alternative method. According to Equations (5.11) and (5.14), γ_0 depends on λ, $\sigma_{r,\mathrm{short}}$ and γ_{others}. Since the ERS data set has many coherent interferograms over short time spans, the estimated γ_0 is expected to be the most reliable. Thus, I approximate γ_0 for the other data sets using γ_0 for the ERS data set by assuming that $\sigma_{r,\mathrm{short}}$ is constant for all data sets at the same location. By inverting Equations (5.11) and (5.14), $\sigma^2_{r,\mathrm{short}}$ can be approximated by

$$\sigma'^2_{r,\mathrm{short}} = 2\left(\frac{\lambda_{\mathrm{ERS}}}{4\pi}\right)^2 \ln\left(\frac{\gamma_{\mathrm{others,\,ERS}}}{\gamma_{0,\mathrm{ERS}}}\right), \tag{5.17}$$

where $\{\cdot\}_{\mathrm{ERS}}$ denotes the parameters for the ERS data set. Substituting Equation (5.17) in Equations (5.11) and (5.14), the initial coherence γ_0 for the other data sets can be approximated by

$$\gamma_0' = \gamma'_{\mathrm{others}} \left(\frac{\gamma_{0,\mathrm{ERS}}}{\gamma_{\mathrm{others,\ ERS}}} \right)^{\left(\frac{\lambda_{\mathrm{ERS}}}{\lambda'}\right)^2}, \tag{5.18}$$

where $\{\cdot\}'$ denotes the parameters for another data set.

In an urban area, hardly affected by the temporal decorrelation, γ_0 will approximately equal to γ_{others}. An average of $\gamma_{0,\mathrm{ERS}}$ among the coherence estimation windows where $\gamma_{\infty,\mathrm{ERS}}$ is larger than 0.5 is 0.83. Therefore I conservatively assume $\gamma_{\mathrm{others,\ ERS}} = 0.83$ for all coherence estimation windows. For the other data sets $\gamma'_{\mathrm{others}}$ is also required to approximate γ_0'. As it is not possible to estimate $\gamma'_{\mathrm{others}}$ accurately, I use the same value as the ERS data set.

Figures 5.9 and 5.10 show the approximated $\sigma'_{r,\mathrm{short}}$ and γ_0' for the other wavelengths. X-band shows the lowest γ_0' due to its high sensitivity to surface perturbations. Given these updated and approximated initial coherence values γ_0', I recomputed the corresponding values for γ_∞ and τ using Equation (5.16).

5.4.3 Results and discussion

Figures 5.11 and 5.12 are the recomputed results of Figures 5.7 and 5.8, respectively. For all data sets, τ is shorter than the previous results, see Figure 5.7. In particular τ for C-band during summer (Apr-Sep) is about ten days or less, which implies that it was unlikely to obtain a coherent signal because the repeat intervals of past C-band satellites are much longer. The Sentinel-1 mission, however, will be able to satisfy this condition with its 6-day repeat interval with two satellites. RS2-HH

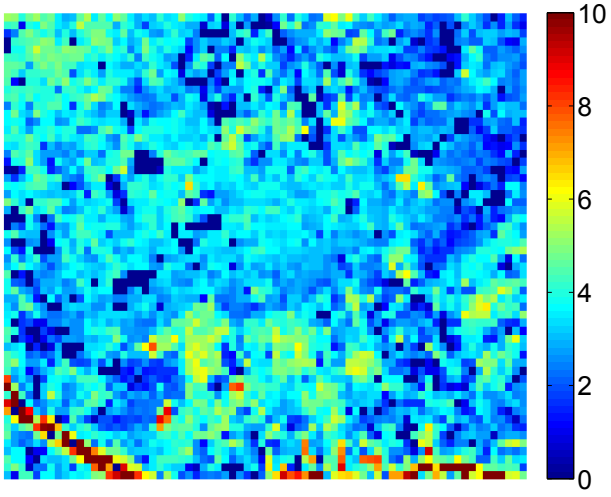

Figure 5.9: Approximated $\sigma'_{r,\text{short}}$ (mm) based on γ_0 for the ERS data set.

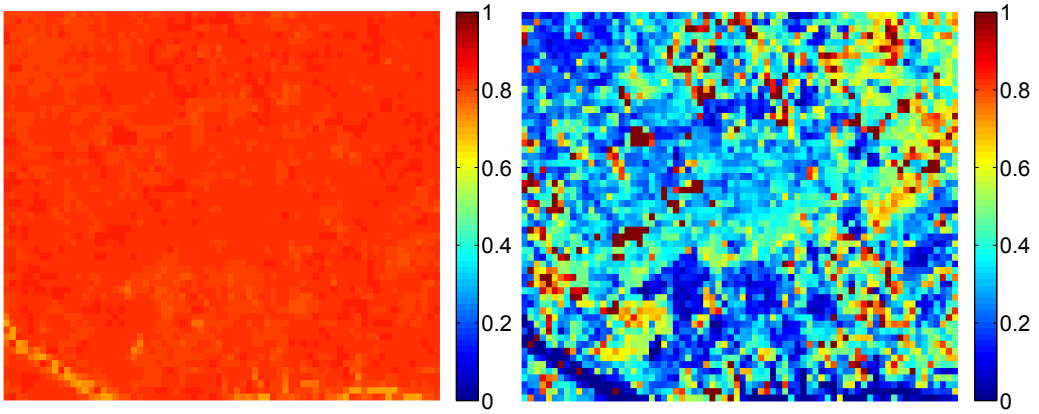

(a) L-band (b) X-band

Figure 5.10: Approximated γ'_0 based on the ERS based initialization. These are comparable with the result of C-band in Figure 5.5a.

shows longer τ values than RS2-HV, similar to the former results.

For L-band the decorrelation rate τ is considerably shorter than expected based on the proportionality to λ^2, predicting a factor 18 between C- and L-band (Equation (5.12)). Nevertheless, the subplots of Figure 5.11 show that L-band has the highest likelihood to obtain coherent signals regardless of seasons, and although the repeat interval of ALOS (46 days) may be not short enough, ALOS-2 (14 days) will surely be sufficient.

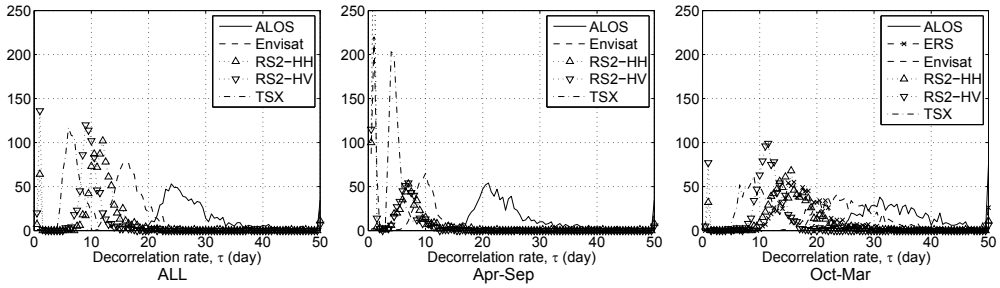

Figure 5.11: Histograms of the recomputed τ, tuned using the approximated γ'_0. The wavelength dependency is evident, as L-band data show significantly larger τ.

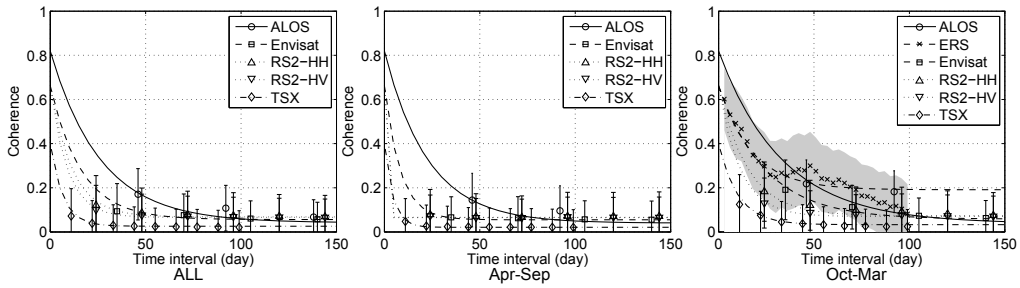

Figure 5.12: Recomputed time dependency of the coherence, tuned using the approximated γ'_0. The symbols and error bars indicate the median and standard deviation of the coherence at each time interval in the pasture area. To avoid clogging, a shadow region was used to indicate the standard deviations of the ERS data in Oct-Mar.

During winter, X-band has longer τ than expected, comparable to the repeat interval of TSX. This could be due to the high resolution of TSX, which leads to a large L and therefore a low bias in the coherence estimation. In other words, a larger multilook factor can be used compared to C-band. This means that a higher resolution would increase the chance to exploit low-coherent DS. This hypothesis is supported by the fact that Envisat with slightly higher resolution than RS2 has longer τ than RS2.

The models described here rely for the initial coherence γ_0 on the ERS result during winter periods and the assumption that these results may be used to approximate γ_0 for the missions with longer repeat orbits. It should be stressed that this assump-

tion will fail if the coherence factors due to spatial decorrelation, volume decorrelation, processing noise and thermal noise differ significantly between the different sensors. For pasture, however, it can be assumed these factors to be reasonably comparable. Secondly, the fact that the reference data from ERS were all acquired during winter may positively bias the approximation of γ_0. Moreover, these ERS reference data were all acquired during the early 1990's, more than a decade before the other data sets. Although some more urbanization may have occurred at the edges of the pasture areas, the main area did not change in terms of land use.

To analyze the practical implication of these models, I estimated decorrelation time, t_{td}, using the estimated temporal decorrelation models. I define $E\{|\hat{\gamma}|\} + \sigma_{|\hat{\gamma}|}$ at $|\gamma| = 0$ as a coherence associated with total decorrelation $\hat{\gamma}_{\mathrm{td}}$ calculated from Equations (5.4) and (5.5) for a given number of independent samples L. With $|\hat{\gamma}| = \hat{\gamma}_{\mathrm{td}}(L)$ in Equation (5.16), I find

$$t_{\mathrm{td}}(L) = \tau \ln\left(\frac{\gamma_0 - \gamma_\infty}{\hat{\gamma}_{\mathrm{td}}(L) - \gamma_\infty}\right) \tag{5.19}$$

for every sensor. The relationship between t_{td} and L is shown in Figure 5.13. These graphs show that in order to obtain a coherent signal during winter time (Oct-Mar), an averaging window with $L = 200$ would be sufficient for all sensors. However, in summer C- and X-band would not provide significant information with $L = 200$, whereas L-band can. Shorter repeat intervals or larger values of L are required. Sentinel-1, whose repeat interval is six days with two satellites, would enable coherent signals in summer with $L = 50$ or by averaging 20×4 pixels, assuming an oversampling rate of 1.5, equivalent to an area of 80×80 m.

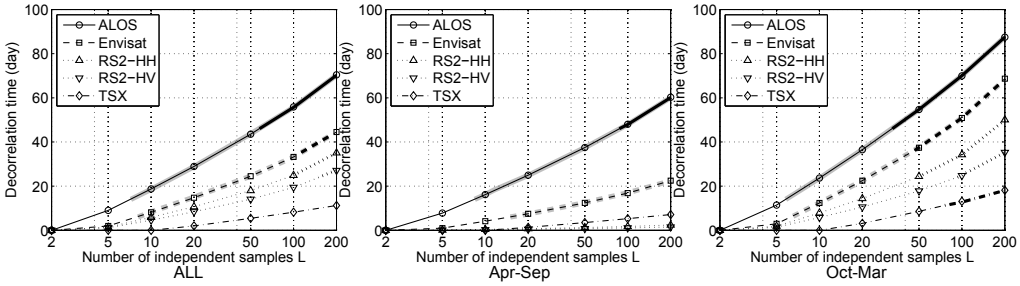

Figure 5.13: Decorrelation time t_{td} as a function of the number of independent samples L (log scale) for each data set. Black bold parts of the lines indicate that the repeat interval of the satellite is shorter than the decorrelation time, allowing for coherent observations. Gray bold parts indicate that the repeat intervals of the new satellites, ALOS-2 for ALOS and Sentinel-1 for Envisat, are shorter than the decorrelation time.

5.5 Conclusions

Given all available satellite SAR data, the decorrelation characteristics of pasture on drained peat soils were investigated and temporal decorrelation models were proposed for L-, C-, and X-band. The standard decorrelation model was extended to three parameters, including the effects of instantaneous decorrelation, termed the initial coherence, as well as the long-term coherence affected by the bias of the coherence estimation. The estimation of the initial coherence is hampered by the lack of the very short time interval interferometric combinations, producing a negatively biased result. This was solved by using C-band 3-day repeat interval data sets of ERS, forward propagating the variance of the motion of the scatterers to the approximated initial coherence for X- and L-band. Based thereupon, it was demonstrated that the combination of the repeat intervals and the coherence estimation windows enable the estimation of coherent signal over pasture on drained peat soils, particularly for the new satellite missions ALOS-2 and Sentinel-1. Although longer wavelengths are ad-

vantageous, it is the combination of longer wavelengths, shorter repeat intervals and higher spatial resolution that increases the likelihood to obtain a coherent signal.

Chapter 6

Displacement extraction by integrative InSAR analysis

Paper was published in *IEEE Transactions on Geoscience and Remote Sensing*

Morishita, Y. and R. F. Hanssen, 2015: Deformation Parameter Estimation in Low Coherence Areas Using a Multisatellite InSAR Approach, *IEEE Trans. Geosci. Remote Sens.*, 53(8), 4275-4283, doi:10.1109/TGRS.2015.2394394

6.1 Introduction

Chapter 5 revealed that pasture areas suffer from very quick temporal decorrelation. Although an interferogram with a very short time interval can have a coherent signal particularly in winter, it is not sufficient for a precise measurement of subsidence because the short time interval means small displacement, i.e., low SNR. SBAS, a useful technique to track a slow displacement using many coherent interferograms integrally, is not effectual either in this case because of too small available coherent interferograms. Displacement detected by PSI is unlikely to represent subsidence of peat meadow as mentioned in Sections 4.3 and 4.5. Consequently these existing InSAR techniques including time series analysis such as PSI and SBAS are not able to measure the displacement in the target area precisely.

Here I propose an approach to enhance the capability of SBAS in a quickly decorrelating area by integrally using multisatellite data sets. Whereas other studies have also proposed approaches to combine different data sets for improving the precision and temporal coverage (Pepe et al., 2005; Ozawa and Ueda, 2011), I focus on a more severely decorrelating area where the number of coherent interferograms is extremely limited. I also propose a precise and efficient method to estimate complex coherence using adjacent adaptive windows. I present the results in the target area covered with pasture on drained peat soils where significant subsidence has been suspected but could not have been detected by existing InSAR techniques.

Section 6.2 is dedicated to the explanation of adaptive coherence estimation to precisely estimate complex coherence. Basic and the advanced SBAS algorithms are described in Section 6.3. I test the advanced method using real data over the pasture on drained peat soils in the Netherlands in Section 6.4, followed by the result in Section 6.5 and the conclusion in Section 6.6.

6.2 Adaptive coherence estimation

As mentioned in Section 5.2, the complex coherence is calculated by

$$\hat{\gamma} = |\hat{\gamma}|e^{i\hat{\phi}} = \frac{\sum_{n=1}^{N} y_{1n} y_{2n}^{*}}{\sqrt{\sum_{n=1}^{N} |y_{1n}|^2 \sum_{n=1}^{N} |y_{2n}|^2}}. \tag{5.2}$$

Whereas homogeneity and ergodicity are assumed in this computation, in reality both assumptions may not be valid because within the estimation window there may be different pixels with different scattering characteristics, e.g., buildings, pasture and water. Consequently, an estimated coherence and a multilooked phase would be imprecise and biased.

One solution to estimate the complex coherence more precisely is the use of an adaptive window in contrast to a common boxcar window. Recently, Ferretti et al. (2011) proposed an algorithm to find statistically homogeneous pixels (SHP) based on amplitude statistics of a pixel evaluated over time series. Whether two specified pixels are SHP or not is evaluated by a goodness-of-fit testing. It was reported that the Anderson-Darling test (Pettitt, 1976; Scholz and Stephens, 1987) is the most appropriate test if a sufficiently large number of SAR images are available (Parizzi and Brcic, 2011).

The Anderson-Darling test can be performed for all pairs of pixels to preserve full resolution. However, when the area is large and/or the resolution is high, the computation time becomes infeasibly long. If the full resolution is not required, the computation time can be saved at the expense of resolution.

Firstly I allocate adjacent rectangular windows without overlapping. Given the incoherent average of amplitude over all acquisitions, I select a pixel closest to the median value over the window as a reference pixel for that window. Its scattering characteristic should be comparable to the majority of the scatterers in the window and therefore the reference pixel should have relatively a lot of SHP. Then the Anderson-Darling test is applied between the reference pixel and the other pixels in the window to identify SHP.

Figure 6.1 shows an example of distribution of the reference pixels (yellow stars) and SHP (red dots) for two adjacent windows. The reference pixels are located in the pasture which is a dominant surface type over the area. The water surface and man-made structures such as buildings, bridges and roads seem to be correctly rejected. This technique would also prevent underestimation of the deformation seen in the results of PSI (Cuenca and Hanssen, 2007) mentioned in Section 4.3. Estimating the coherence based on all SHP in the window will now give a coherence estimate that is closer to the true value.

(a) Optical image (Google Earth)

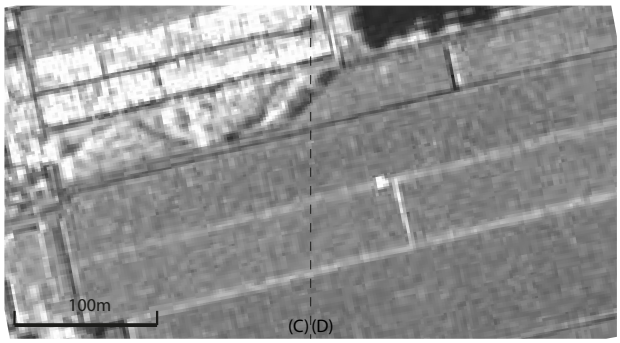

(b) Incoherent average of amplitude

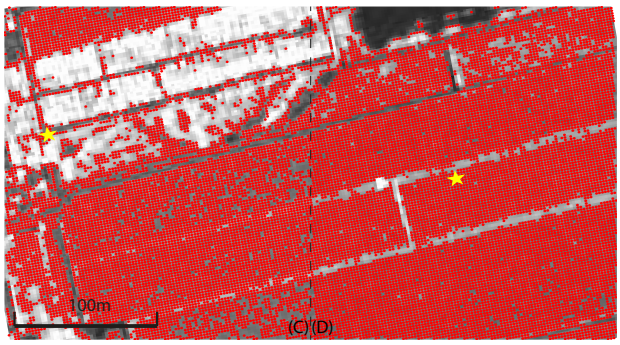

(c) Reference pixels and SHP

Figure 6.1: Two estimation windows, labeled (C) and (D), further used in Figure 6.6. (a) Optical image. (C) contains pasture, buildings and higher vegetation, whereas (D) dominantly contains pasture. (b) Incoherently averaged amplitude of TSX-A data set (Table 4.1). (c) Reference pixels and SHP. The reference pixels are indicated with the yellow stars, and the SHP related to those reference pixels indicated with the distribution of red dots. SHP appear to be selected correctly because buildings, trees and water surfaces are rejected.

6.3 Estimation method

6.3.1 Basic SBAS algorithm

Following the SBAS algorithm (Berardino et al., 2002; Casu et al., 2006; Lanari et al., 2007), I assume $n + 1$ SAR acquisitions, indicated by vector $\boldsymbol{\psi}$, and m multimaster, small baseline, interferograms, $\boldsymbol{\delta\phi}$, where

$$\boldsymbol{\delta\phi} = [\delta\phi_1, \ldots, \delta\phi_m]^T = \mathbf{A}\boldsymbol{\phi}, \text{ and} \tag{6.1}$$

$$\boldsymbol{\phi} = [\phi(t_1), \ldots, \phi(t_n)]^T \tag{6.2}$$

$$= \frac{4\pi}{\lambda}[d(t_1), \ldots, d(t_n)]^T, \tag{6.3}$$

where $\delta\phi_i$ is the observed unwrapped phase difference of the i^{th} interferometric combination which is sufficiently coherent, for a specific pixel. The design matrix $\mathbf{A}$ creates combinations of the single master temporal stack of interferograms $\boldsymbol{\phi}$, and $\phi(t_j) = \psi(t_j) - \psi(t_0)$ and $d(t_j)$ are the unknown unwrapped phase and LOS displacement of the j^{th} image with regards to $\psi(t_0)$ and $d(t_0)$ at a pixel respectively, at the time of the master t_0.

As mentioned in Section 2.2, the observed phase contains several phase components,

$$\delta\phi_i = \delta\phi_i^{\text{defo}} + \delta\phi_i^{\text{topo}} + \delta\phi_i^{\text{orb}} + \delta\phi_i^{\text{atm}} + \delta\phi_i^{\text{noise}}. \tag{6.4}$$

A temporally smooth deformation model is assumed, consisting of a linear (L) and a

seasonal periodic (P) component:

$$\begin{aligned}\phi^{\mathrm{LP}}(t_j) &= \frac{4\pi}{\lambda}[vt_j + S\,\sin 2\pi t_j + C(\cos 2\pi t_j - 1)] \\ &= \frac{4\pi}{\lambda}[vt_j + A\sin 2\pi(t_j - \Delta t) + A\sin 2\pi\Delta t], \end{aligned} \tag{6.5}$$

where v is the linear deformation rate, and S and C are the coefficients describing the seasonal periodic (annual) displacement (van Leijen and Hanssen, 2007). A and Δt are the amplitude and the time offset of the seasonal periodic displacement relative to the master acquisition, respectively, i.e.,

$$A = \sqrt{S^2 + C^2}, \text{ and} \tag{6.6}$$

$$\Delta t = -\,\mathrm{sgn}(C)\arccos(S/A)/2\pi. \tag{6.7}$$

The LP deformation is defined to be zero at the master acquisition ($t_0 = 0$). The phase difference due to the DEM error Δz, can be written as

$$\delta\phi_i^{\mathrm{topo}} = \frac{4\pi}{\lambda}\frac{B_{\perp i}}{r\sin\theta}\Delta z, \tag{6.8}$$

where $B_{\perp i}$ is the perpendicular baseline of the i^{th} interferogram, r is the range distance, and θ is the incidence angle (Hanssen, 2001). The residual orbital phase $\delta\phi_i^{\mathrm{orb}}$ can be estimated as a phase ramp using the unwrapped phase (Hanssen, 2001; González and Fernández, 2011).

After subtracting the residual orbital phase ramp, and assuming that the unmodeled deformation, atmospheric noise and the other error sources are independent of time and zero mean, the relation between the observed interferometric combinations

$\boldsymbol{\delta\phi}$, the LP deformation model parameters $\mathbf{x}$, and the DEM error Δz can be written as

$$\boldsymbol{\delta\phi} = \frac{4\pi}{\lambda}\left[\mathbf{AM}|\mathbf{c}\right]\begin{bmatrix}\mathbf{x}\\ \Delta z\end{bmatrix} + \boldsymbol{\epsilon}, \tag{6.9}$$

where $\mathbf{A}$ is the $m \times n$ design matrix describing the relation between $\boldsymbol{\phi}$ and $\boldsymbol{\delta\phi}$, see Equation (6.1),

$$\mathbf{M} = \begin{bmatrix} t_1 & \sin 2\pi t_1 & \cos 2\pi t_1 - 1 \\ \vdots & \vdots & \vdots \\ t_n & \sin 2\pi t_n & \cos 2\pi t_n - 1 \end{bmatrix} \tag{6.10}$$

relates these observations to the vector of unknown parameters $\mathbf{x} = [v, S, C]^T$, and a vector

$$\mathbf{c} = \left[\frac{B_{\perp 1}}{r \sin\theta}, \ldots, \frac{B_{\perp m}}{r \sin\theta}\right]^T \tag{6.11}$$

scales the DEM error Δz to the interferometric phase.

Equation (6.9) can be solved to minimize $\boldsymbol{\epsilon}$ by several approaches. The most common way is an ordinary least squares method (LS). An iteratively reweighted LS (IRLS) method, which minimize L_1-norm, might be better because it is more robust with respect to outliers possibly caused by unwrapping errors (Lauknes et al., 2011). Moreover, if a variance-covariance (VC) matrix of the observations $Q_{\boldsymbol{\delta\phi}}$ is available, the best linear unbiased estimator of unknowns $\hat{\mathbf{x}}$ and $\hat{\Delta z}$, and their VC matrix $Q_{\hat{\mathbf{x}},\hat{\Delta z}}$ are given by

$$\begin{bmatrix}\hat{\mathbf{x}}\\ \hat{\Delta z}\end{bmatrix} = \frac{\lambda}{4\pi}\left(\left[\mathbf{AM}|\mathbf{c}\right]^T Q_{\boldsymbol{\delta\phi}}^{-1}\left[\mathbf{AM}|\mathbf{c}\right]\right)^{-1}\left[\mathbf{AM}|\mathbf{c}\right]^T Q_{\boldsymbol{\delta\phi}}^{-1}\boldsymbol{\delta\phi}, \tag{6.12}$$

and

$$Q_{\hat{\mathbf{x}},\hat{\Delta z}} = \left(\frac{\lambda}{4\pi}\right)^2 \left(\left[\mathbf{AM}|\mathbf{c}\right]^T Q_{\delta\phi}^{-1} \left[\mathbf{AM}|\mathbf{c}\right]\right)^{-1}, \tag{6.13}$$

respectively, based on a generalized least squares method (GLS) (Hanssen, 2001). The advantage of this approach is that the errors of the observations and their correlations are taken into account and a posterior VC matrix of the estimator of unknowns is given. Here I use GLS because the variances of the observations are not equal and there is a correlation between them. Derivation of a VC matrix of the observations is described in Section 6.4.2 in detail.

Once the LP deformation model parameters $\hat{\mathbf{x}}$ and the DEM error $\hat{\Delta z}$ are estimated, the residual phase—calculated by subtracting the phase due to the LP deformation model and the DEM error from the wrapped phase—is unwrapped again to reduce the unwrapping errors, followed by retrieving the phase of the LP deformation model in a second iteration. This yields an improved unwrapped phase $\boldsymbol{\delta\phi}'$ without the DEM error.

As a next step, the unknown displacement, $\mathbf{d}$, cf. Equation (6.3), at each acquisition can be estimated by solving

$$\boldsymbol{\delta\phi}' = \frac{4\pi}{\lambda}\mathbf{Ad} + \boldsymbol{\epsilon}'. \tag{6.14}$$

Here, LS, IRLS or GLS can be applied as well, similar to the previous step. The estimator $\hat{\mathbf{d}}$ is independent of the LP deformation model and includes the unmodeled deformation and APS. Note that Equation (6.14) cannot be solved unless all interferograms are connected. This follows from the fact that disconnected subsets of

interferograms would result in a rank deficiency of the design matrix **A**, and a singular value decomposition (SVD) can be used to compute the pseudo inverse of **A**. Berardino et al. (2002) has shown that this would result in large discontinuities in the cumulative deformations, leading to solutions which are not physically realistic. This is solved by changing the formulation to estimate velocity between acquisitions, instead of phase differences, i.e., by changing **A** and replacing **d** by a vector of velocities per pixel, following Berardino et al. (2002).

Note that temporal overlap between the different subsets is required to obtain a reliable solution. Finally, the APS can be estimated using a spatio-temporal filter optionally (Ferretti et al., 2000; Hooper et al., 2007).

6.3.2 Combination of multiple data sets

Basically the greater the number of available data is, the more robust the estimation is. In this case the number of the available interferograms for each data set is not sufficient to get a reliable result due to the fast decorrelation as it will be shown in Figure 6.4. However the number of interferograms can be increased by combining independent data sets—perhaps with different wavelengths and incidence angles—given some assumptions. Assuming that the deformation has only a vertical component, i.e.,

$$\mathbf{x} = \mathbf{x}_{\mathrm{v}} \cos\theta = [v_{\mathrm{v}}, S_{\mathrm{v}}, C_{\mathrm{v}}]^T \cos\theta, \text{ and} \tag{6.15}$$

$$\mathbf{d} = \mathbf{d}_{\mathrm{v}} \cos\theta, \tag{6.16}$$

where $\{\cdot\}_{\mathrm{v}}$ denotes the vertical component, Equations (6.9) and (6.14) for independent data sets with different wavelengths and incidence angles can be expanded as

$$\begin{bmatrix} \boldsymbol{\delta\phi}^1 \\ \vdots \\ \boldsymbol{\delta\phi}^K \end{bmatrix} = \begin{bmatrix} \frac{4\pi}{\lambda^1}[\mathbf{A}^1\mathbf{M}^1\cos\theta^1|\mathbf{c}^1] \\ \vdots \\ \frac{4\pi}{\lambda^K}[\mathbf{A}^K\mathbf{M}^K\cos\theta^K|\mathbf{c}^K] \end{bmatrix} \begin{bmatrix} \mathbf{x}_{\mathrm{v}} \\ \Delta z \end{bmatrix} + \boldsymbol{\epsilon}, \tag{6.17}$$

and

$$\begin{bmatrix} \boldsymbol{\delta\phi'}^1 \\ \vdots \\ \boldsymbol{\delta\phi'}^K \end{bmatrix} = \begin{bmatrix} \frac{4\pi}{\lambda^1}\mathbf{A}^1\cos\theta^1 \\ \vdots \\ \frac{4\pi}{\lambda^K}\mathbf{A}^K\cos\theta^K \end{bmatrix} \mathbf{d}_{\mathrm{v}} + \boldsymbol{\epsilon}', \tag{6.18}$$

respectively, where $\{\cdot\}^K$ represents K^{th} data set.

Combining multiple data sets will improve the precision of the results due to the improved temporal sampling. Moreover, if the different data sets have different temporal coverage and if they are temporally overlapping, the time period of the estimated time series of the deformation is extended.

6.4 Validation with real data

I applied these methods to an area south of Delft, the Netherlands (Figure 4.3). The groundwater level in the area is monitored continuously and changes periodically—low in summer and high in winter (van Leijen and Hanssen, 2007). Past studies have suggested that the annual component of the surface displacement has a 1–2 month delay with respect to the groundwater level change (van Leijen and Hanssen, 2007; Cuenca and Hanssen, 2007).

I did not use the two ERS-1 data sets (Table 4.1) for the joint estimation due to their old acquisition date compared to the other data sets. The RS2-HV data set was not used either because RS2-HH showed higher coherence than RS2-HV according to Chapter 5. Consequently I use six data sets hereafter; ALOS-i, ALOS-ii, Envisat, RS2-HH (simply referred as RS2 from here), TSX-A and TSX-D in Table 4.1.

Figure 6.2 is the flowchart of the processing approach. In the SBAS processing, firstly all images in a single data set were coregistered to a single image and geocoded. Spectral filtering was applied to the possible interferometric combinations in order to mitigate spatial decorrelation (Gatelli et al., 1994). These processes were implemented using Doris (Kampes et al., 2003). I allocated adjacent rectangular windows based on geometrical coordinates to uniformize the location and the width of the windows between all data sets as is the case in Chapter 5. The dimension of the windows is about 230 m $\times$ 230 m. After the reference pixels were identified from the incoherent average of amplitude, SHP were selected in each window by applying the Anderson-Darling test, see Section 6.2. Distribution of the number of SHP for each data set is shown in Figure 6.3. Whereas the pasture has large number of SHP, in urbanized areas the number of SHP is small as expected (Ferretti et al., 2011). Finally complex coherence was computed using SHP by Equation (5.2).

In the computation of the complex coherence, I subtracted the orbital residual phase ramps estimated from the PSI results (Figure 4.7) as well as the topographic phase. The phase ramps for all single master interferograms were computed by LS from the unwrapped phase at PS using the PSI results. Then the phase ramps for multimaster interferograms were estimated from their appropriate combinations. The estimated orbital phase ramps are accurate enough because PS are distributed suffi-

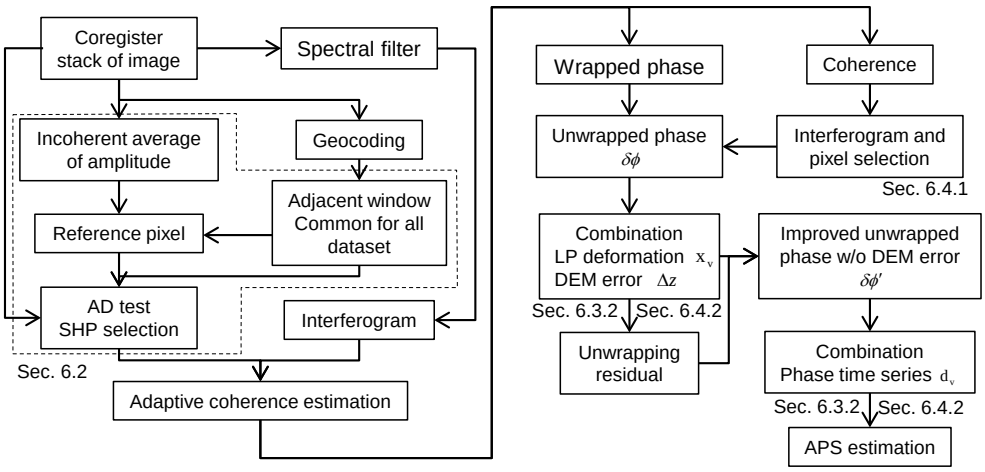

Figure 6.2: Flowchart of processing approach.

ciently dense and homogeneous and there seems to be no large deformation at all PS in the area (Figure 4.7). The bias of the phase for each image as a whole was also estimated simultaneously. By removing the orbital phase ramp and the bias, the phase for each image was adjusted with reference to the average of the PS. This means that it is not necessary to choose a particular point as a reference point where the phase is set to zero.

6.4.1 Selection of pixels and interferograms based on coherence

There are very few pixels with adequate coherence due to very fast temporal decorrelation over the pasture. These decorrelated pixels were discarded to avoid unwrapping errors. Similarly, interferograms with many decorrelated pixels were discarded since they increase computing time but hardly contribute to the final results. Conventionally, a coherence threshold has been used to discard decorrelated pixels (Berardino et al., 2002; González and Fernández, 2011; Lauknes et al., 2011). However, the calculated coherence is biased, and its bias and standard deviation depend

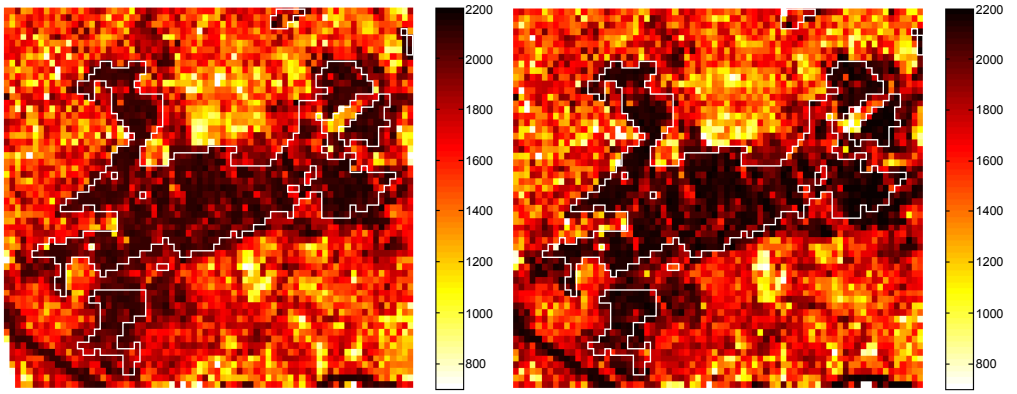

(a) ALOS-i (b) ALOS-ii

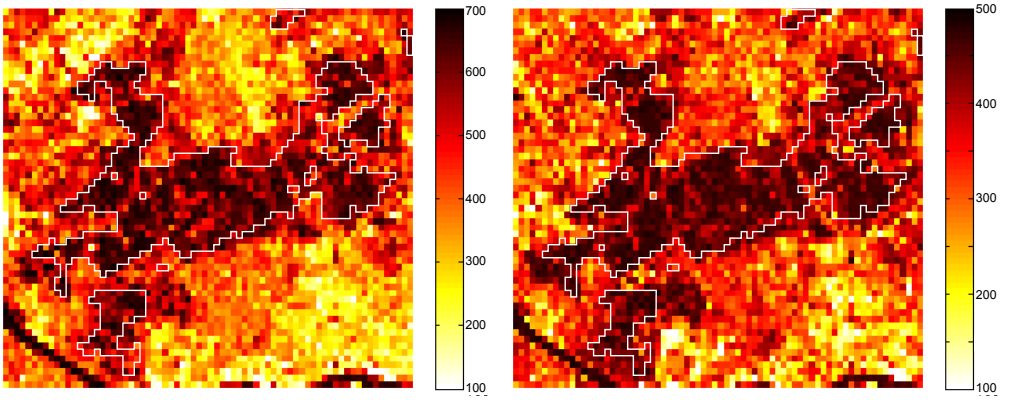

(c) Envisat (d) RS2

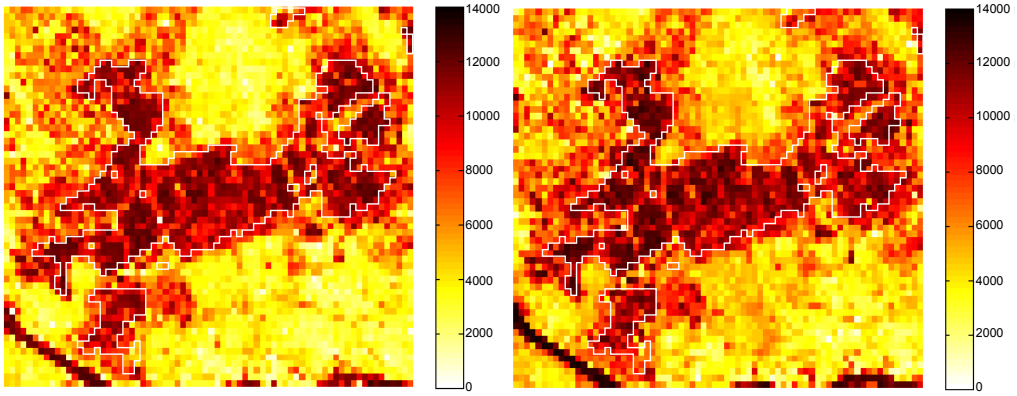

(e) TSX-A (f) TSX-D

Figure 6.3: Maps of the number of SHP. The areas delineated by white polygons correspond to pasture. Note that the color scales are different for each data set.

on the number of independent samples L and the coherence magnitude (Figure 5.1).

Additionally L varies depending on resolution (satellite-dependent) and on the ap-

plication of the adaptive coherence window (Figure 6.3). Therefore the coherence threshold should not be a common constant value.

I computed the coherence threshold by the same approach as the total decorrelation $\hat{\gamma}_{\mathrm{td}}$ in Section 5.4.3. The number of independent samples L was calculated from the number of SHP and the oversampling rate of the SAR image (Table 4.1). Note that this means each pixel in each data set will have a different coherence threshold. The pixels with the lower coherence than the calculated coherence threshold were discarded. The interferograms with more discarded pixels than 30% of all pixels were excluded from further processing.

As a result of selection of the pixels and the interferograms, only a limited number of the interferograms has been kept (Figure 6.4, Tables A.4–A.6 and Figures B.1–B.12). Since longer wavelengths are less affected by temporal decorrelation, ALOS data sets keep the interferograms with relatively long time intervals (Zebker and Villasenor, 1992; Rosen et al., 1996; Wei and Sandwell, 2010). There are more applicable interferograms in winter than in summer due to the slower temporal decorrelation in winter. There are only four interferograms with longer time intervals than a year. Whereas their wrapped phases in the pasture are almost decorrelated, they still seem to show an increase in the LOS (Figure B.1). For the ALOS-ii data set, the perpendicular baseline is correlated with time for consecutive images, which could result in the leaking of linear deformation signals into the estimation of DEM errors. TSX data sets show a lot of available interferograms due to their short revisit time interval.

Following the selection of pixels and interferograms, I unwrapped the phase by a statistical-cost approach, the same method as StaMPS/MTI (Hooper, 2010), and estimated LP deformation parameters using VC matrices described in the next section.

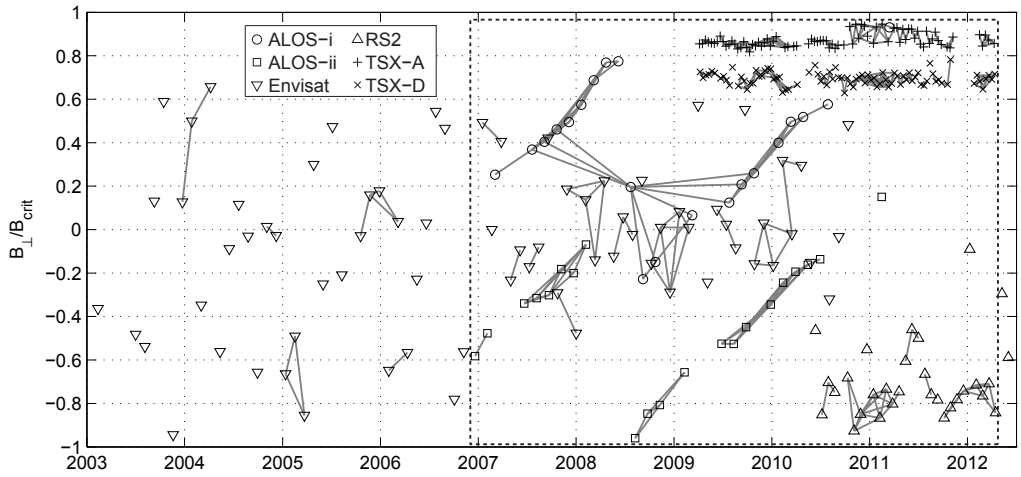

Figure 6.4: All available SAR images and baseline configuration. Perpendicular baselines are normalized to the critical baseline (Hanssen, 2001). The gray solid lines indicate selected interferograms based on coherence (Section 6.4.1). A box with a dashed line indicates the time period shown in Figure 6.8.

6.4.2 Estimation of VC matrix of observation

The VC matrix of the observations $Q_{\delta\phi}$ is necessary for GLS. Mainly $Q_{\delta\phi}$ contains the effects of APS and decorrelation (Samieie-Esfahany and Hanssen, 2011; Akbari and Motagh, 2012), i.e.,

$$Q_{\delta\phi} = Q_{\mathrm{APS}} + Q_{\mathrm{coh}}, \tag{6.19}$$

where Q_{APS} and Q_{coh} are the VC matrix of APS and the decorrelation effect, respectively.

Diagonal elements of Q_{APS} are the sum of the variance of APS for a master and a slave image. The variance of APS for the j^{th} image, $\sigma^2_{\mathrm{APS},t_j}$, was calculated from the estimated APS for each image, which were obtained from the PS results using temporal high-pass and spatial low-pass filtering (Hooper et al., 2007) (Fig-

ures B.13–B.30). Off-diagonal elements of Q_{APS} describe correlation between interferograms. If an image is commonly used in two interferograms, these interferograms are correlated. The covariance between them is the variance of the common image (Emardson et al., 2003; Akbari and Motagh, 2012). The covariance is positive if the common image is used as a master or a slave for both interferograms, whereas negative if used as a master for an interferogram and a slave for the other. For example, suppose that only three interferograms from two images are available, $\boldsymbol{\delta\phi} = [\phi(t_2) - \phi(t_1), \phi(t_3) - \phi(t_1), \phi(t_3) - \phi(t_2)]^T$, I get

$$Q_{\mathrm{APS}} = \begin{bmatrix} \sigma^2_{\mathrm{APS},t_1} + \sigma^2_{\mathrm{APS},t_2} & \sigma^2_{\mathrm{APS},t_1} & -\sigma^2_{\mathrm{APS},t_2} \\ \sigma^2_{\mathrm{APS},t_1} & \sigma^2_{\mathrm{APS},t_1} + \sigma^2_{\mathrm{APS},t_3} & \sigma^2_{\mathrm{APS},t_3} \\ -\sigma^2_{\mathrm{APS},t_2} & \sigma^2_{\mathrm{APS},t_3} & \sigma^2_{\mathrm{APS},t_2} + \sigma^2_{\mathrm{APS},t_3} \end{bmatrix}. \tag{6.20}$$

Q_{coh} has only diagonal elements derived from coherence. The phase variance σ^2_ϕ can be estimated from the theoretical coherence γ and the number of looks L (Hanssen, 2001),

$$\sigma^2_\phi = \int_{-\pi}^{+\pi} [\phi - \phi_0]^2 pdf(\phi) d\phi, \text{ with} \tag{6.21}$$

$$\begin{aligned} pdf(\phi; \gamma, L, \phi_0) = & \frac{(1-|\gamma|^2)^L}{2\pi} \left\{ \frac{\Gamma(2L-1)}{[\Gamma(L)]^2 2^{2(L-1)}} \right. \\ & \times \left[\frac{(2L-1)\beta}{(1-\beta^2)^{L+1/2}} \left(\frac{\pi}{2} + \arcsin\beta \right) + \frac{1}{(1-\beta^2)^L} \right] \\ & \left. + \frac{1}{2(L-1)} \sum_{r=0}^{L-2} \frac{\Gamma(L-1/2)}{\Gamma(L-1/2-r)} \frac{\Gamma(L-1-r)}{\Gamma(L-1)} \frac{1+(2r+1)\beta^2}{(1-\beta^2)^{r+2}} \right\}, \end{aligned} \tag{6.22}$$

where $\beta = |\gamma|\cos(\phi - \phi_0)$, see Figure 6.5. The theoretical coherence $|\gamma|$ was estimated from $|\hat{\gamma}|$ by numerically inverting Equation (5.4).

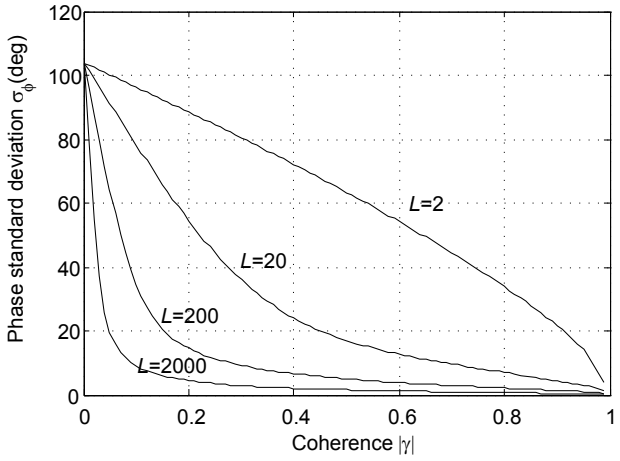

Figure 6.5: Phase standard deviation σ_ϕ as a function of the theoretical coherence $|\gamma|$ and the number of looks L. As might be expected, high coherence leads to low standard deviation. Note that a large number of looks also reduce the standard deviation.

6.5 Results of joint estimation

Table 6.1 shows the average of the estimated parameters and their posterior standard deviations for each single and combined data set, indicated by the radar bands of L, C, and X. Single data sets show relatively large standard deviations but reasonably consistent subsidence rates and annual deformation. In particular ALOS-ii and RS2 have very large standard deviations because ALOS-ii has a correlation between time and baseline as mentioned in Section 6.4.1 and RS2 has fewer and noisier interferograms (Figure B.7). By combining these data sets, however, the standard deviations become smaller, which means the results are more reliable. LCX combination is regarded as the final result because its standard deviations are small and temporal coverage is the longest, though the standard deviations of the other combinations are comparable with the LCX combination. With a standard deviation of 5.7 mm/yr, the estimated linear deformation rate 36.6 mm/yr is considered to be significant.

Table 6.1: Average of estimated parameters

Used data set	Band	$\bar{\hat{v}}_v$ [a] mm/yr	$\bar{\sigma}_{\hat{v}_v}$	$\bar{\hat{A}}_v$ mm	$\bar{\sigma}_{\hat{A}_v}$	$\bar{\hat{\Delta t}}$ [b] day	$\bar{\sigma}_{\hat{\Delta t}}$	$\bar{\hat{\Delta z}}$ m	$\bar{\sigma}_{\hat{\Delta z}}$
ALOS-i	L	21.5	8.4	14.8	4.1	-41	20	-1.0	1.1
ALOS-ii	L	24.2	34.3	13.0	5.7	-40	31	0.5	4.9
Envisat	C	32.7	19.4	9.1	3.7	-30	20	-1.4	1.5
RS2	C	32.4	39.4	6.3	6.9	-50	111	-0.8	6.6
TSX-A	X	54.4	10.2	13.1	2.9	-31	14	-0.7	1.8
TSX-D	X	37.5	12.7	9.4	2.8	-45	24	-2.7	1.3
ALOS-i and -ii	L	20.3	7.1	14.3	3.1	-40	16	-0.7	1.0
Envisat and RS2	C	33.2	16.5	8.3	3.1	-33	20	-1.4	1.5
TSX-A and -D	X	47.0	8.0	11.0	1.9	-36	11	-2.1	1.0
ALOS-i, -ii, Envisat and RS2	LC	22.7	5.6	10.0	2.3	-49	20	0.3	0.6
ALOS-i, -ii, TSX-A and -D	LX	36.7	6.1	10.8	1.8	-45	13	-0.7	0.7
Envisat, RS2, TSX-A and -D	CX	46.5	7.2	10.9	1.7	-35	10	-2.0	0.9
ALOS-i, -ii, Envisat, RS2, TSX-A and -D	LCX	36.6	5.7	10.6	1.6	-44	12	-0.8	0.7

[a] Positive values mean subsidence [b] With reference to 1 January

The results for single-band estimations are quite different, both considering numerical values as well as in terms of significance. Although this demonstrates the need to improve quality by combining data sets, differences can also be due to differences in observation period, e.g., for L-band December 2006 - July 2010 and X-band April 2009 - April 2012, in combination with possible non-linear behavior. Variations in the effective scattering center height for different wavelengths could also influence the results, especially the seasonal periodic signal. Yet, the interannual subsidence rate would be unaffected because it covers a whole year or longer. Based on all results, it seems safe to conclude that this area is subsiding faster than 20

mm/yr on average.

Figures 6.6 and 6.7 show the maps of the estimated parameters and their standard deviations of the joint (combined) adjustment based on all data sets, respectively. In the pasture area, outlined by the polygon, a significant subsidence rate is visible, spatially variable and with an average subsidence value of $\bar{\hat{v}}_v = 36.6$ mm/yr. For comparison, the middle west part around (B), which is an area of greenhouses, shows slow subsidence in Figure 6.6a, in agreement with the PSI results of Figure 4.7. The average amplitude within the pasture is $\bar{\hat{A}}_v = 10.6$ mm (Figure 6.6b), and the time offset $\bar{\hat{\Delta}}t = -44$ days with reference to 1 January (Figure 6.6c), corresponding with a maximum at 17 February and a minimum at 18 August, consistent with previous studies (Cuenca and Hanssen, 2007; van Leijen and Hanssen, 2007).

Figure 6.8 shows the estimated time series of the displacement at the positions (A)–(E) in Figure 6.6, between December 2006 and April 2012 (used interferograms can be seen in Figure 6.4). Position (A) is in the urban area, and can be considered as stable, whereas position (B) (greenhouse area) shows slow subsidence, as discussed above. Position (C) and (D) are in the pasture area, exhibit a linear subsidence rate of 25 and 31 mm/yr, respectively. Position (E) shows one of the maximum subsidence signals, with more than 400 mm over the time period, equivalent to 89 mm/yr. The densely sampled time series in Figure 6.8 show that by combining multiple data sets the estimation becomes more robust. It has to be noted that, however, the estimated time series of the displacement might not be sufficiently reliable because the number of the used interferograms is not large compared with the number of the estimated parameters and there are few temporally overlapping interferograms, see Figure 6.4, whereas there are plenty of redundant interferograms in the estimation of the LP

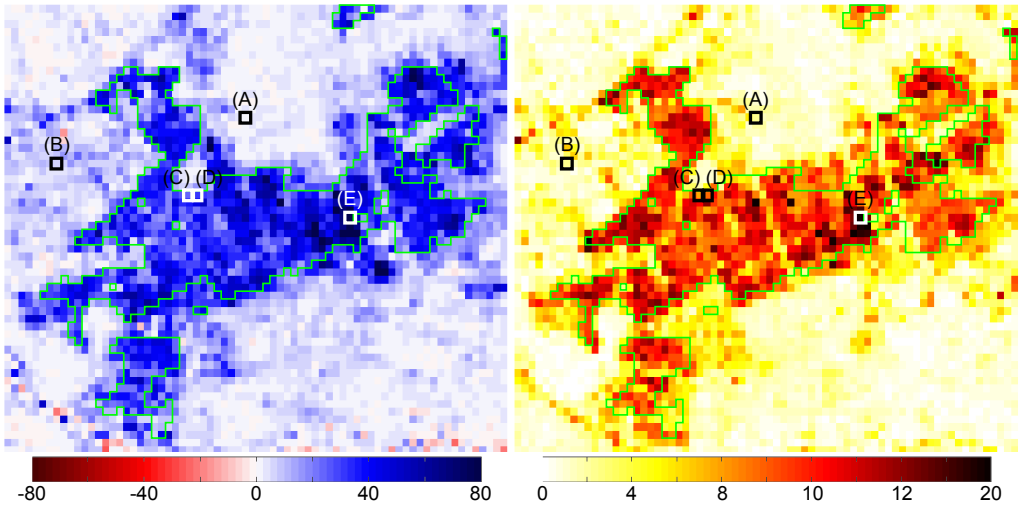

(a) Linear subsidence rate $\hat{v}_v$ (mm/yr)

(b) Amplitude of the periodic annual signal $\hat{A}_v$ (mm)

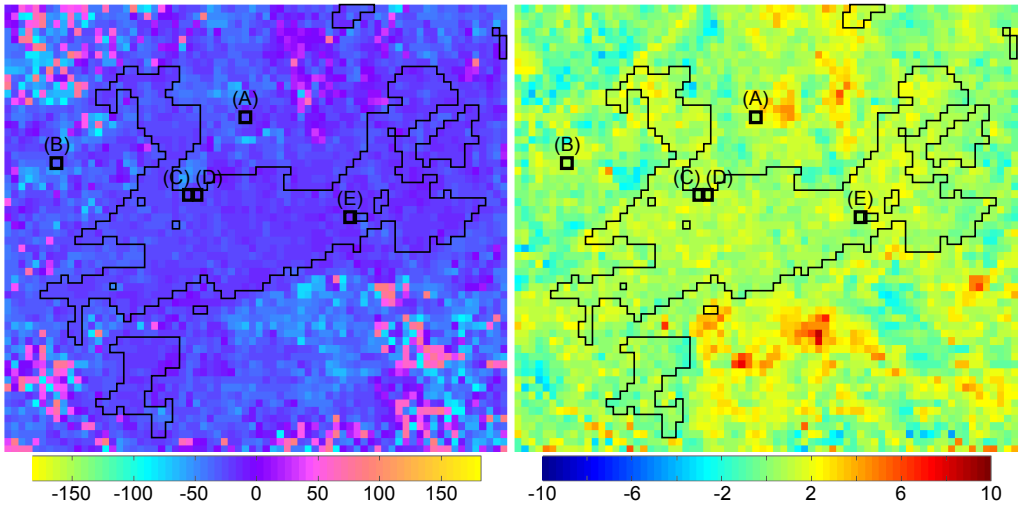

(c) Time offset $\hat{\Delta t}$ of the sinusoidal signal (day) with reference to 1 January

(d) DEM error $\hat{\Delta z}$ (m)

Figure 6.6: Maps of the estimated LP deformation parameters and DEM error for combined data set using all data sets. Positive values of $\hat{v}_v$ indicate subsidence. The areas with large deformation, delineated by the polygons, correspond to the pasture. Deformation time series at (A)–(E) are shown in Figure 6.8.

components. Therefore $\hat{\mathbf{d}}_v$ could be easily affected by phase noises such as decorrelation and APS unlike $\hat{\mathbf{x}}_v$ and $\hat{\Delta z}$, which might be the cause of the jump of the height change seen in Figure 6.8.

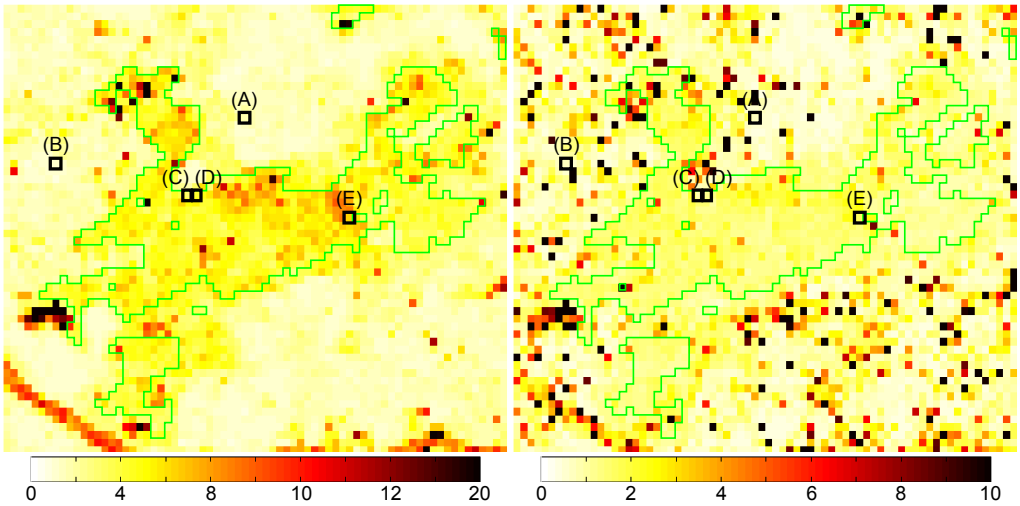

(a) $\sigma_{\hat{v}_v}$ (mm/yr) (b) $\sigma_{\hat{A}_v}$ (mm)

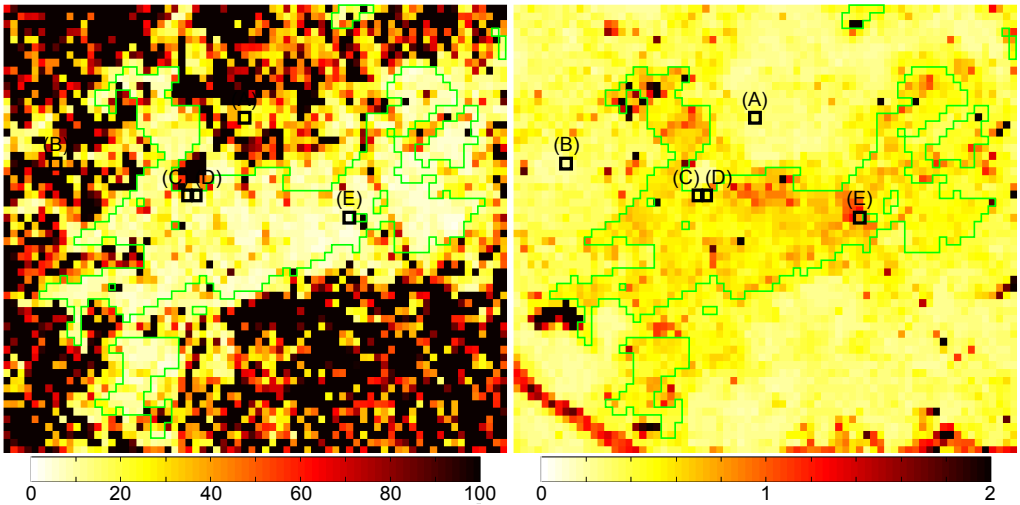

(c) $\sigma_{\hat{\Delta t}}$ (day) (d) $\sigma_{\hat{\Delta z}}$ (m)

Figure 6.7: Maps of the standard deviations of the model parameters for combined data set using all data sets. The areas delineated by the polygons correspond to the pasture.

The seasonal periodic deformation (Figure 6.6b) has spatially variable amplitude but is strongly correlated with the subsidence rates. This is expected, since volume change of peat occurs mainly due to two causes; consolidation and oxidation (Nieuwenhuis and Schokking, 1997). Consolidation is partly reversible and affected by groundwater levels—generally low in summer and high in winter. Oxidation

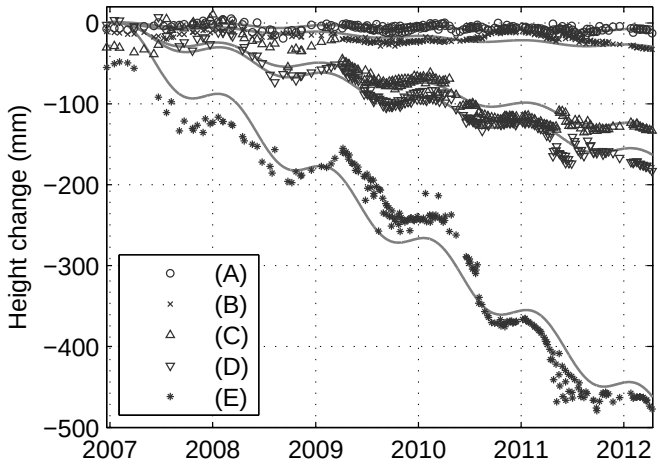

Figure 6.8: Time series of displacement at (A)–(E) in Figure 6.6. Lines are the best fit LP deformation and symbols are the estimated height change at each acquisition. The height changes are adjusted to equalize the LP deformations at 20 December 2006. (C)–(E) in pasture have large annual and linear deformation, whereas (A) in the urban area is almost stable. (B) shows slow subsidence, corresponding to the PSI result (Figure 4.7).

happens when the peat is exposed to the air, and is irreversible, leading to interannual subsidence. The amplitude of the volume change caused by either phenomenon would be proportional to the volume of the exposed peat. Therefore the more peat in the vadose zone, the faster the subsidence rate and the larger the amplitude of the seasonal deformation. In other words, the area with large linear and periodic deformation may have thicker peat. Another possible interpretation of the correlation between $\hat{v}_\mathrm{v}$ and $\hat{A}_\mathrm{v}$ is that the motion might be stepwise; subsidence only in summer (Figure 6.8). A large subsidence rate only in summer would yield a pseudo large amplitude in the seasonal periodic function.

Such a large deformation can generally yield phase unwrapping errors, especially for X-band and C-band. In this case, however, this is not likely because the used interferograms have very short time intervals (Figures 6.4, 6.9 and Tables A.4– A.6).

Although in winter the time intervals are relatively long, the deformation is very small due to high ground water level, as also seen in Figure 6.8. In summer the longest time interval of the used interferograms is 33 days for X-band. Even if there is a 50 mm/yr displacement rate difference between adjacent pixels, which seems to be possible at the border between pasture and another no deformation area, there is only 4.5 mm gap for 33 days, much less than 7.75 mm equivalent to π rad for X-band.

To assess the influence of the filtering of nonrepresentative pixels with the adaptive coherence estimation window, I also performed the joint estimation without applying the adaptive filtering. From the results (Figure 6.10), it appears that windows with mixed contents (e.g. buildings and pasture) may result in a significantly underestimated subsidence rate. This is an expected effect, since the buildings usually have a dominant amplitude and do not exhibit the deformation rates of the pasture. From this comparison, I conclude that the adaptive coherence window filtering plays an important role in the applied methodology.

6.6 Conclusions

For areas with fast temporal decorrelation, such as pasture, conventional time series InSAR methods such as PSI and SBAS are not able to detect small deformation signals. Here I have demonstrated that it is still possible to estimate such deformation by (1) spatial averaging of SHP using nonoverlapping estimation windows, (2) a parametric deformation model and an GLS method, and (3) a combination of all available satellite SAR data derived from different sensors. Application of the method on the real data has shown that the pasture near Delft is subsiding on aver-

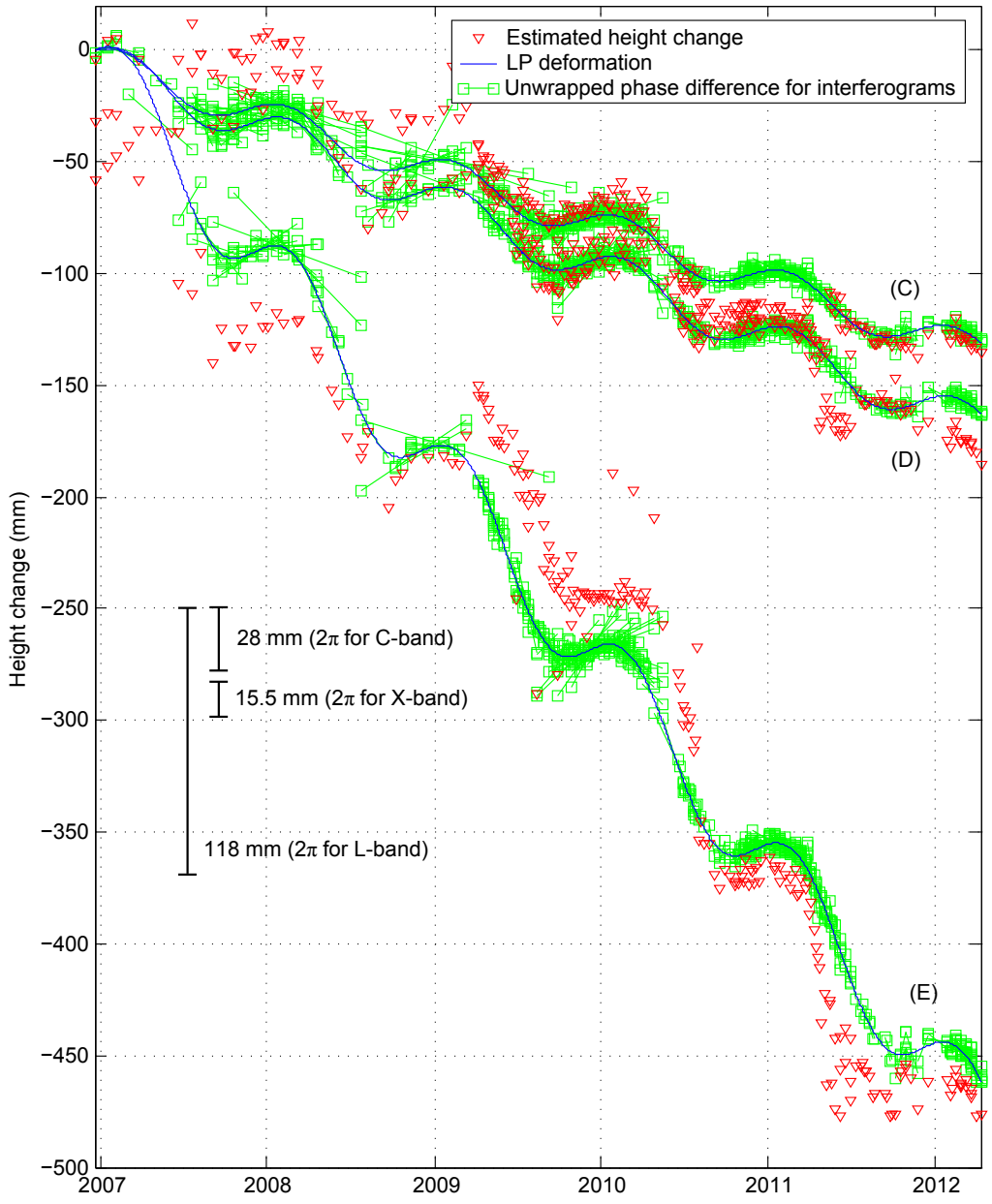

Figure 6.9: Time series of the estimated deformation at (C), (D) and (E) with unwrapped phase difference of the used interferograms. There seems no phase difference larger than 2 π for each wavelength, implying improbable unwrapping errors.

age 36.6 mm/yr, albeit with significant local variability, that seasonal variation has an amplitude of 10.6 mm, and that the maximum of the seasonal height occurs very homogeneously in time. Application of this technique over larger areas in the Nether-

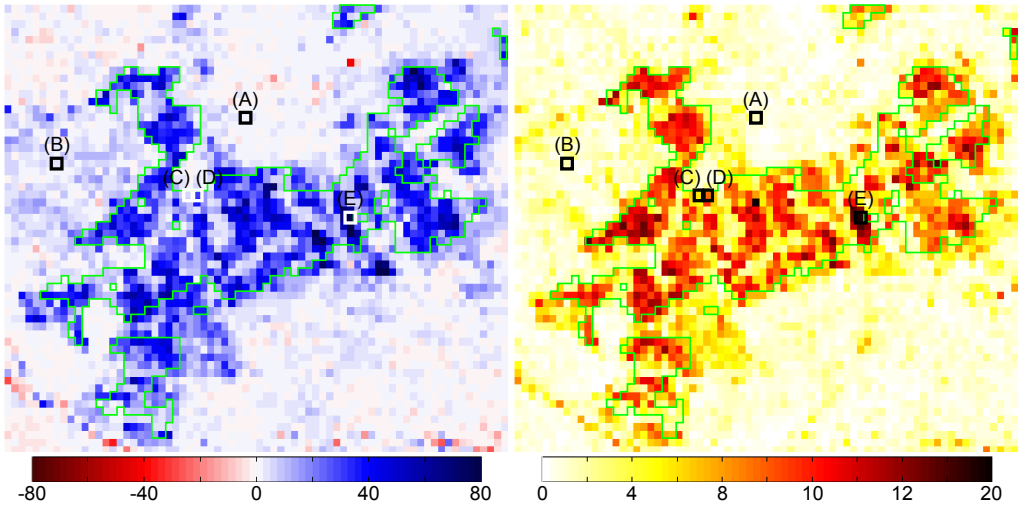

(a) $\hat{v}_v$ (mm/yr) (b) $\hat{A}_v$ (mm)

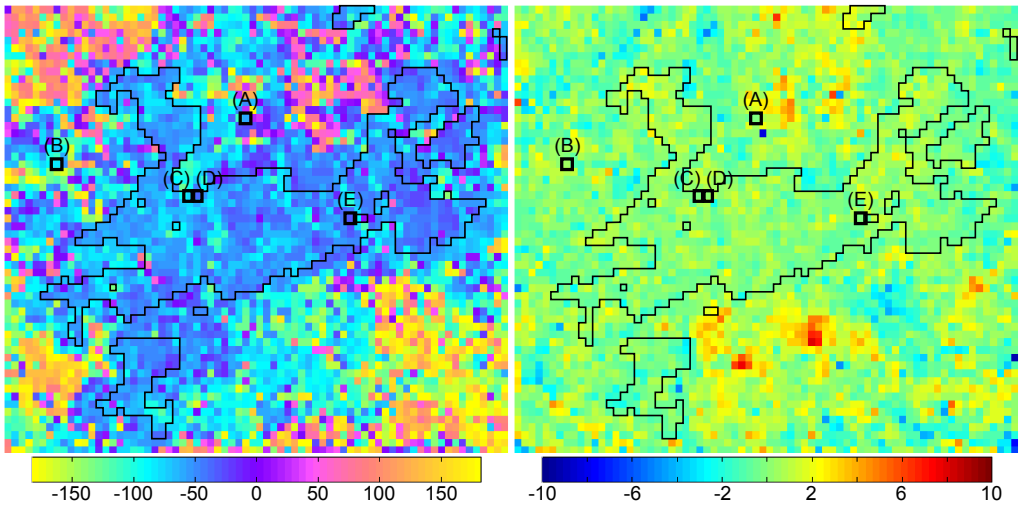

(c) $\hat{\Delta}t$ (day) (d) $\hat{\Delta}z$ (m)

Figure 6.10: Maps of the estimated LP deformation parameters and a DEM error for combined data set using all data sets without applying the adaptive windows.

lands will have important consequences for water management.

Chapter 7

Conclusion

Whereas InSAR is a powerful tool to detect ground surface displacement, it suffers from temporal decorrelation and conventional approaches have not succeeded in detecting subsidence precisely over pasture. It is important to measure height changes of peat meadows for water management. I studied temporal decorrelation behavior and displacement in a pasture area on drained peat soils in the Netherlands. I also investigated measuring capability of PSI using L- and C-band which is important for using PSI as a deformation monitoring method. I summarize the main conclusions of this thesis as follows:

Chapter 3: Comparison of PSI measuring capability of L- and C-band

(1) Density of identified PS points depends on the inherent spatial resolution of the used data in urban areas.

(2) L-band has a better capability to detect PS points in vegetated areas than C-band.

(3) Measuring precision of an individual PS point is about 8-11 mm and 2-3 mm for L- and C-band, respectively, almost proportional to the wavelength, suggesting that the shorter wavelength is more suitable for pointwise usage such as infrastructure monitoring.

(4) Measuring accuracy of spatially averaged PS points is about 4-6 mm and 2 mm/yr, and does not have a significant dependency on the wavelength, which means L-band has a comparable capability of detecting spatially distributed deformation to C-band.

Chapter 5: Quantitative assessment of temporal decorrelation in L-, C-, and X-band

(1) Temporal decorrelation behavior in a specific peat meadow area has been quantitatively assessed for three kinds of wavelengths; L-, C- and X-band.

(2) It has been quantitatively proven that a longer wavelength has longer decorrelation time.

(3) Decorrelation speed has seasonal dependence; slower in winter than in summer.

(4) Not only a wavelength and revisit time of a satellite but also spatial resolution is a critical factor to obtain a coherent signal.

(5) New SAR satellites with short revisit time or high spatial resolution will enhance the chance to detect displacement.

Chapter 6: Displacement extraction by integrative InSAR analysis

(1) A new multisatellite InSAR approach has been proposed to overcome severe temporal decorrelation.

(2) It has been shown by validation with real data that integrative use of multisatellite data makes parameter estimation more robust.

(3) Subsidence of 36.6 mm/yr and annual vertical fluctuations with an amplitude of 10.6 mm, a maximum at 17 February and a minimum at 18 August on average have been significantly detected in the target area.

(4) An adaptive coherence estimation method helps to avoid underestimation of displacement possibly due to stable buildings with deep foundations.

Appendix A

Used SAR data and interferograms in Chapter 5 and 6

Table A.1: List of acquisition date (yyyymmdd) of SAR images (ALOS and ERS-1)

ALOS-i		ALOS-ii		ERS-i		ERS-ii	
1	20070305	1	20061220	1	19920129	1	19931225
2	20070721	2	20070204	2	19920201	2	19931228
3	20070905	3	20070622	3	19920204	3	19931231
4	20071021	4	20070807	4	19920207	4	19940103
5	20071206	5	20070922	5	19920210	5	19940106
6	20080121	6	20071107	6	19920213	6	19940109
7	20080307	7	20071223	7	19920216	7	19940112
8	20080422	8	20080207	8	19920219	8	19940115
9	20080607	9	20080809	9	19920222	9	19940118
10	20080723	10	20080924	10	19920225	10	19940121
11	20080907	11	20081109	11	19920228	11	19940124
12	20081023	12	20090209	12	19920302	12	19940127
13	20090310	13	20090627	13	19920305	13	19940130
14	20090726	14	20090812	14	19920308	14	19940202
15	20090910	15	20090927	15	19920311	15	19940205
16	20091026	16	20091228	16	19920314	16	19940208
17	20100126	17	20100212	17	19920317	17	19940211
18	20100313	18	20100330	18	19920320	18	19940214
19	20100428	19	20100515	19	19920326	19	19940217
20	20100729	20	20100630	20	19920329	20	19940220
21	20110316	21	20110215			21	19940223
						22	19940226
						23	19940301
						24	19940304
						25	19940307
						26	19940310
						27	19940313
						28	19940316
						29	19940319
						30	19940322
						31	19940325
						32	19940328
						33	19940406
						34	19940409

Table A.2: List of acquisition date (yyyymmdd) of SAR images (Envisat and RS2)

Envisat						RS2	
1	20030212	31	20060517	61	20090506	1 [a]	20100613
2	20030702	32	20060621	62	20090610	2 [a]	20100707
3	20030806	33	20060726	63	20090715	3	20100731
4	20030910	34	20060830	64	20090819	4	20100824
5	20031015	35	20061004	65	20090923	5	20101011
6	20031119	36	20061108	66	20091028	6	20101104
7	20031224	37	20070117	67	20091202	7	20101128
8	20040128	38	20070221	68	20100106	8	20101222
9	20040303	39	20070328	69	20100210	9	20110115
10	20040407	40	20070502	70	20100317	10	20110208
11	20040512	41	20070606	71	20100421	11	20110304
12	20040616	42	20070711	72	20100526	12	20110328
13	20040721	43	20070815	73	20100804	13	20110421
14	20040825	44	20070919	74	20100908	14	20110515
15	20040929	45	20071024	75	20101013	15	20110608
16	20041103	46	20071128			16	20110702
17	20041208	47	20080102			17	20110726
18	20050112	48	20080206			18	20110819
19	20050216	49	20080312			19	20110912
20	20050323	50	20080416			20	20111006
21	20050427	51	20080521			21	20111030
22	20050601	52	20080625			22	20111123
23	20050706	53	20080730			23	20111217
24	20050810	54	20080903			24	20120110
25	20051019	55	20081008			25	20120203
26	20051123	56	20081112			26	20120227
27	20051228	57	20081217			27	20120322
28	20060201	58	20090121			28	20120415
29	20060308	59	20090225			29	20120509
30	20060412	60	20090401			30	20120602

[a] Only HH data; no HV data

Table A.3: List of acquisition date (yyyymmdd) of SAR images (TSX)

TSX-A				TSX-D			
1	20090406	44	20101019	1	20090408	44	20101021
2	20090417	45	20101030	2	20090419	45	20101101
3	20090428	46	20101110	3	20090430	46	20101112
4	20090509	47	20101121	4	20090511	47	20101123
5	20090520	48	20101202	5	20090522	48	20101204
6	20090531	49	20101213	6	20090602	49	20101215
7	20090611	50	20100224	7	20090624	50	20101226
8	20090622	51	20110115	8	20090705	51	20110106
9	20090703	52	20110126	9	20090716	52	20110117
10	20090714	53	20110217	10	20090727	53	20110128
11	20090725	54	20110311	11	20090807	54	20110208
12	20090805	55	20110402	12	20090829	55	20110219
13	20090816	56	20110413	13	20090909	56	20110302
14	20090827	57	20110424	14	20090920	57	20110313
15	20090907	58	20110505	15	20091001	58	20110324
16	20090918	59	20110516	16	20091012	59	20110404
17	20090929	60	20110527	17	20091023	60	20110415
18	20091010	61	20110607	18	20091103	61	20110426
19	20091021	62	20110618	19	20091114	62	20110507
20	20091101	63	20110629	20	20091125	63	20110518
21	20091112	64	20110710	21	20091206	64	20110529
22	20091123	65	20100721	22	20091217	65	20110609
23	20091204	66	20110801	23	20091228	66	20110620
24	20091215	67	20110812	24	20100108	67	20110701
25	20091226	68	20110823	25	20100119	68	20110712
26	20100106	69	20110903	26	20100130	69	20110723
27	20100117	70	20110914	27	20100210	70	20110803
28	20100219	71	20110925	28	20100221	71	20110814
29	20100302	72	20111017	29	20100304	72	20110825
30	20100324	73	20111028	30	20100406	73	20110905
31	20100404	74	20111108	31	20100520	74	20110916
32	20100518	75	20120215	32	20100611	75	20110927
33	20100529	76	20120226	33	20100622	76	20111019
34	20100609	77	20120308	34	20100703	77	20111030
35	20100620	78	20120319	35	20100714	78	20120126
36	20100701	79	20120410	36	20100725	79	20120206
37	20100712			37	20100805	80	20120217
38	20100723			38	20100816	81	20120228
39	20100803			39	20100827	82	20120310
40	20100814			40	20100907	83	20120321
41	20100825			41	20100918	84	20120401
42	20100905			42	20100929	85	20120412
43	20100927			43	20101010		

Table A.4: Selected interferograms based on coherence (ALOS)

ALOS-i					ALOS-ii				
#	M [a]	S [b]	dt [c]	$B_\perp$	#	M	S	dt	$B_\perp$
1	1	2	138	807	1	1	2	46	734
2	2	3	46	249	2	3	4	46	175
3	2	4	92	649	3	3	5	92	270
4	2	5	138	888	4	3	6	138	1110
5	2	6	184	1443	5	4	5	46	95
6	2	10	368	-1205	6	4	6	92	935
7	3	4	46	401	7	4	8	184	1727
8	3	5	92	639	8	5	6	46	840
9	3	6	138	1194	9	5	7	92	712
10	3	7	184	1986	10	5	8	138	1632
11	3	10	322	-1454	11	6	7	46	-127
12	4	5	46	238	12	6	8	92	792
13	4	6	92	793	13	7	8	46	920
14	4	7	138	1585	14	9	10	46	787
15	4	8	184	2154	15	9	11	92	1067
16	4	10	276	-1855	16	10	11	46	280
17	5	6	46	555	17	10	12	138	1334
18	5	7	92	1347	18	11	12	92	1054
19	6	7	46	792	19	13	14	46	-6
20	6	8	92	1361	20	13	15	92	534
21	7	8	46	569	21	13	16	184	1263
22	7	9	92	608	22	14	15	46	540
23	8	9	46	39	23	14	16	138	1269
24	10	11	46	-2971	24	14	17	184	1971
25	10	12	92	-2419	25	15	16	92	729
26	10	13	230	-912	26	15	17	138	1431
27	10	14	368	-504	27	15	18	184	1785
28	10	15	414	82	28	15	19	230	2009
29	10	16	460	439	29	16	17	46	702
30	11	12	46	552	30	16	18	92	1056
31	12	13	138	1507	31	16	19	138	1279
32	14	15	46	585	32	17	18	46	354
33	14	16	92	943	33	17	19	92	577
34	15	16	46	357	34	18	19	46	223
35	15	18	184	2018	35	19	20	46	181
36	15	19	230	2173					
37	16	17	92	988					
38	16	18	138	1661					
39	16	19	184	1816					
40	17	18	46	672					
41	17	19	92	828					
42	18	19	46	155					
43	19	20	92	410					

[a] The number of master image in Table A.1

[b] The number of slave image in Table A.1

[c] Time interval

Table A.5: Selected interferograms based on coherence (Envisat and RS2)

Envisat					RS2				
#	M [a]	S [b]	dt [c]	$B_\perp$	#	M	S	dt	$B_\perp$
1	7	8	35	410	1	2	3	24	192
2	8	10	70	174	2	3	4	24	-59
3	16	17	35	-46	3	5	6	24	-318
4	18	19	35	190	4	5	7	48	-218
5	18	20	70	-210	5	6	7	24	100
6	19	20	35	-401	6	6	9	72	218
7	25	26	35	207	7	6	10	96	77
8	26	27	35	21	8	7	9	48	117
9	26	29	105	-134	9	7	10	72	-24
10	27	29	70	-155	10	7	11	96	150
11	28	30	70	91	11	7	12	120	61
12	37	39	70	-96	12	9	10	24	-141
13	40	41	35	153	13	9	11	48	33
14	42	43	35	99	14	9	12	72	-56
15	45	47	70	-205	15	10	11	24	174
16	46	48	70	-54	16	10	12	48	85
17	46	50	140	42	17	11	12	24	-89
18	48	49	35	-304	18	12	13	24	73
19	48	50	70	97	19	14	15	24	189
20	49	50	35	401	20	15	16	24	-52
21	51	52	35	199	21	17	18	24	-123
22	52	53	35	-89	22	20	21	24	61
23	55	56	35	182	23	20	22	48	110
24	55	57	70	-146	24	21	22	24	49
25	56	57	35	-328	25	21	23	48	100
26	56	58	70	79	26	22	23	24	51
27	56	59	105	0	27	23	25	48	36
28	57	58	35	407	28	23	26	72	-30
29	57	59	70	328	29	23	27	96	44
30	58	59	35	-79	30	25	26	24	-65
31	62	63	35	-76	31	25	27	48	8
32	63	64	35	-120	32	26	27	24	73
33	66	67	35	206	33	26	28	48	-100
34	66	68	70	-9	34	27	28	24	-173
35	67	68	35	-215					
36	67	70	105	-55					
37	68	70	70	160					
38	69	70	35	-372					
39	69	71	70	-25					

[a] The number of master image in Table A.2

[b] The number of slave image in Table A.2

[c] Time interval

Table A.6: Selected interferograms based on coherence (TSX-A)

TSX-A														
#	M [a]	S [b]	*dt* [c]	$B_\perp$	#	M	S	*dt*	$B_\perp$	#	M	S	*dt*	$B_\perp$
1	1	2	11	6	42	24	27	33	58	83	48	49	11	-45
2	2	3	11	90	43	24	28	66	-215	84	48	52	55	-66
3	2	4	22	43	44	24	29	77	-189	85	49	52	44	-22
4	3	4	11	-47	45	24	30	99	-186	86	51	52	11	401
5	4	5	11	-27	46	25	26	11	115	87	51	53	33	476
6	4	6	22	-37	47	25	27	22	230	88	51	54	55	37
7	5	6	11	-9	48	25	28	55	-43	89	52	53	22	75
8	8	9	11	-136	49	25	29	66	-17	90	52	54	44	-363
9	9	10	11	-114	50	26	27	11	114	91	53	54	22	-438
10	9	11	22	-75	51	26	28	44	-158	92	53	55	44	-106
11	10	11	11	39	52	26	29	55	-132	93	54	55	22	332
12	11	12	11	91	53	27	28	33	-273	94	55	56	11	15
13	11	13	22	14	54	27	29	44	-246	95	56	57	11	-362
14	12	13	11	-76	55	28	29	11	26	96	56	58	22	-39
15	12	14	22	-197	56	28	30	33	29	97	57	58	11	323
16	13	14	11	-121	57	28	31	44	43	98	58	59	11	-253
17	13	15	22	-89	58	29	30	22	3	99	58	60	22	9
18	13	16	33	57	59	29	31	33	17	100	58	61	33	4
19	14	15	11	31	60	30	31	11	14	101	59	60	11	262
20	14	16	22	177	61	33	34	11	-57	102	60	61	11	-5
21	15	16	11	146	62	34	35	11	-9	103	61	62	11	-223
22	15	17	22	6	63	35	36	11	29	104	62	63	11	172
23	16	17	11	-140	64	36	37	11	-1	105	63	64	11	-324
24	16	19	33	-69	65	36	38	22	-8	106	66	67	11	-302
25	17	18	11	-110	66	37	38	11	-6	107	67	68	11	110
26	17	19	22	71	67	38	39	11	-177	108	69	70	11	-210
27	18	19	11	181	68	38	40	22	-84	109	70	71	11	-99
28	19	20	11	-33	69	39	40	11	92	110	71	72	22	-59
29	19	21	22	57	70	41	42	11	77	111	72	73	11	-26
30	20	21	11	90	71	44	45	11	-431	112	72	74	22	244
31	21	22	11	-99	72	44	46	22	58	113	73	74	11	271
32	21	23	22	-8	73	45	46	11	489	114	75	76	11	-278
33	21	24	33	82	74	45	47	22	146	115	75	77	22	-6
34	22	23	11	91	75	46	47	11	-343	116	76	77	11	273
35	22	24	22	181	76	46	48	22	-2	117	76	78	22	150
36	22	25	33	9	77	46	49	33	-46	118	76	79	44	65
37	23	24	11	90	78	46	52	77	-68	119	77	78	11	-123
38	23	25	22	-82	79	47	48	11	342	120	77	79	33	-207
39	23	27	44	148	80	47	49	22	297	121	78	79	22	-84
40	24	25	11	-172	81	47	51	55	-126					
41	24	26	22	-57	82	47	52	66	275					

[a] The number of master image in Table A.3

[b] The number of slave image in Table A.3

[c] Time interval

Table A.7: Selected interferograms based on coherence (TSX-D)

TSX-D														
#	M [a]	S [b]	dt [c]	$B_\perp$	#	M	S	dt	$B_\perp$	#	M	S	dt	$B_\perp$
1	1	2	11	-102	53	34	35	11	86	105	54	57	33	-54
2	1	3	22	-53	54	34	36	22	-65	106	54	58	44	10
3	2	3	11	49	55	35	36	11	-151	107	55	56	11	-130
4	2	4	22	59	56	36	37	11	231	108	55	57	22	-253
5	3	4	11	10	57	37	38	11	-124	109	55	58	33	-189
6	3	5	22	65	58	40	41	11	-7	110	55	59	44	-10
7	4	5	11	54	59	41	42	11	-264	111	56	57	11	-123
8	4	6	22	24	60	41	43	22	0	112	56	58	22	-59
9	5	6	11	-31	61	42	43	11	264	113	56	59	33	120
10	6	7	22	-91	62	43	44	11	-101	114	57	58	11	64
11	7	8	11	34	63	44	45	11	-59	115	57	59	22	243
12	7	9	22	-31	64	44	46	22	79	116	58	59	11	179
13	8	9	11	-65	65	44	47	33	117	117	58	60	22	130
14	9	10	11	-94	66	45	46	11	138	118	59	60	11	-49
15	12	13	11	157	67	45	47	22	176	119	60	61	11	-151
16	12	15	33	-60	68	46	47	11	38	120	60	62	22	2
17	13	14	11	-70	69	46	48	22	74	121	61	62	11	153
18	14	15	11	-147	70	46	51	55	-15	122	61	63	22	82
19	15	16	11	109	71	46	52	66	21	123	62	63	11	-71
20	16	17	11	-3	72	46	54	88	-82	124	62	64	22	54
21	16	18	22	225	73	47	48	11	36	125	63	64	11	125
22	17	18	11	227	74	47	49	22	-107	126	63	65	22	-16
23	17	19	22	121	75	47	51	44	-53	127	64	65	11	-141
24	18	19	11	-106	76	47	52	55	-17	128	65	66	11	63
25	18	20	22	-101	77	47	54	77	-120	129	66	67	11	75
26	18	21	33	-4	78	47	55	88	79	130	68	69	11	-16
27	19	20	11	5	79	47	56	99	-51	131	69	70	11	77
28	19	21	22	101	80	48	49	11	-142	132	72	73	11	-133
29	20	21	11	97	81	48	52	44	-52	133	73	74	11	27
30	20	22	22	137	82	48	53	55	-208	134	74	75	11	-60
31	20	23	33	127	83	49	51	22	54	135	75	76	22	-20
32	20	25	55	-32	84	49	52	33	90	136	76	77	11	433
33	21	22	11	40	85	49	53	44	-66	137	78	80	22	36
34	21	23	22	30	86	51	52	11	36	138	78	81	33	-100
35	21	25	44	-129	87	51	53	22	-120	139	78	82	44	82
36	22	23	11	-10	88	51	54	33	-67	140	78	83	55	143
37	22	25	33	-169	89	51	55	44	131	141	79	80	11	-108
38	23	25	22	-159	90	51	56	55	2	142	79	82	33	-63
39	24	25	11	17	91	51	57	66	-122	143	79	83	44	-1
40	24	27	33	-237	92	52	53	11	-156	144	80	81	11	-137
41	24	28	44	-193	93	52	54	22	-104	145	80	82	22	45
42	24	29	55	-182	94	52	55	33	95	146	80	83	33	107
43	25	26	11	17	95	52	56	44	-35	147	81	82	11	182
44	25	27	22	-253	96	52	57	55	-158	148	81	83	22	243
45	25	28	33	-209	97	52	58	66	-94	149	81	84	33	172
46	25	29	44	-199	98	53	54	11	52	150	82	83	11	61
47	27	28	11	44	99	53	55	22	251	151	82	84	22	-10
48	27	29	22	54	100	53	56	33	121	152	82	85	33	82
49	28	29	11	10	101	53	57	44	-2	153	83	84	11	-71
50	28	30	44	95	102	53	58	55	62	154	83	85	22	21
51	29	30	33	85	103	54	55	11	199	155	84	85	11	92
52	33	34	11	-125	104	54	56	22	69					

[a] The number of master image in Table A.3

[b] The number of slave image in Table A.3

[c] Time interval

Appendix B

Supplementary figures

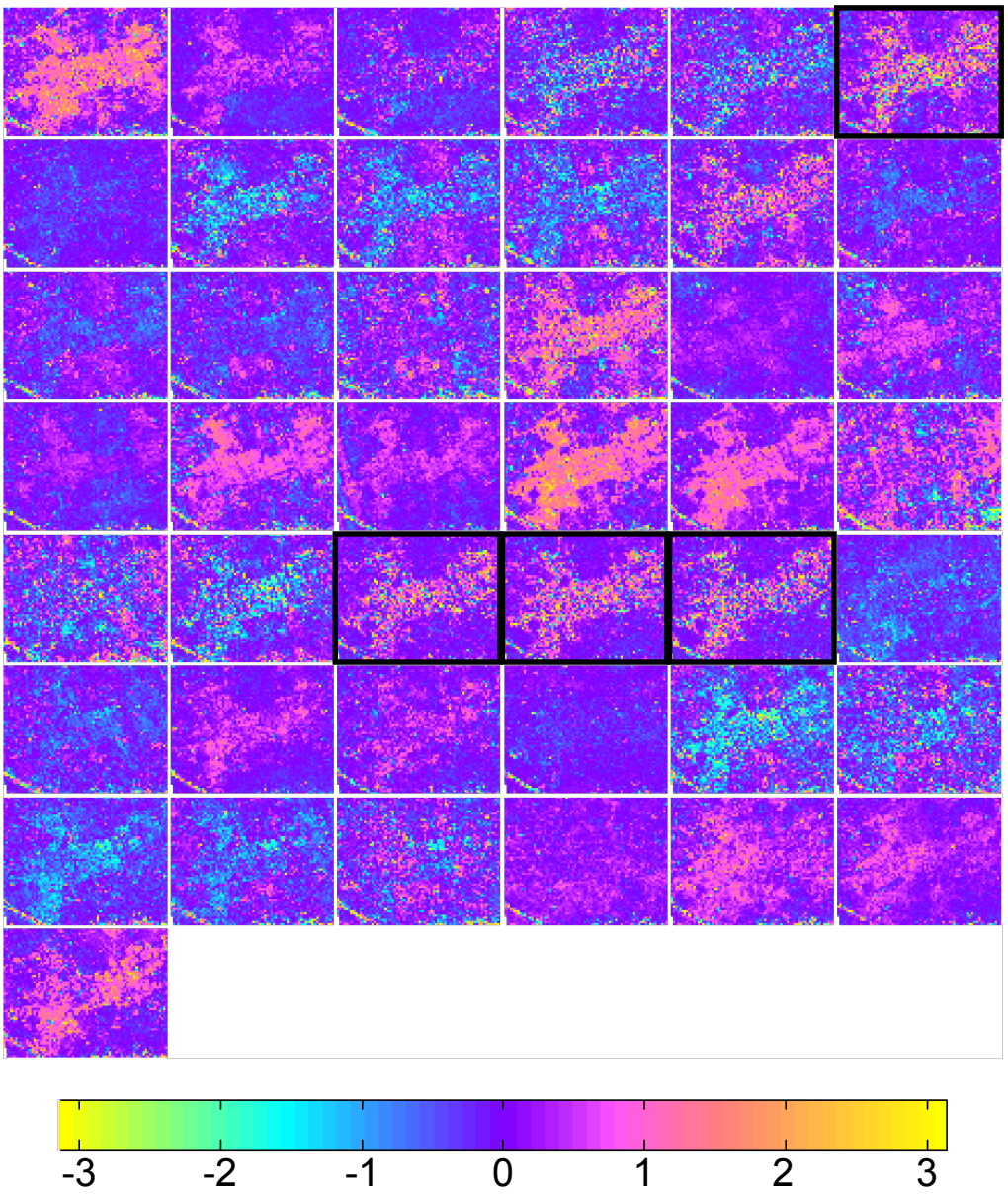

Figure B.1: Wrapped phase (rad) of ALOS-i. Information of the interferograms are in Table A.1 and A.4. Interferograms framed by black line have longer time interval than a year.

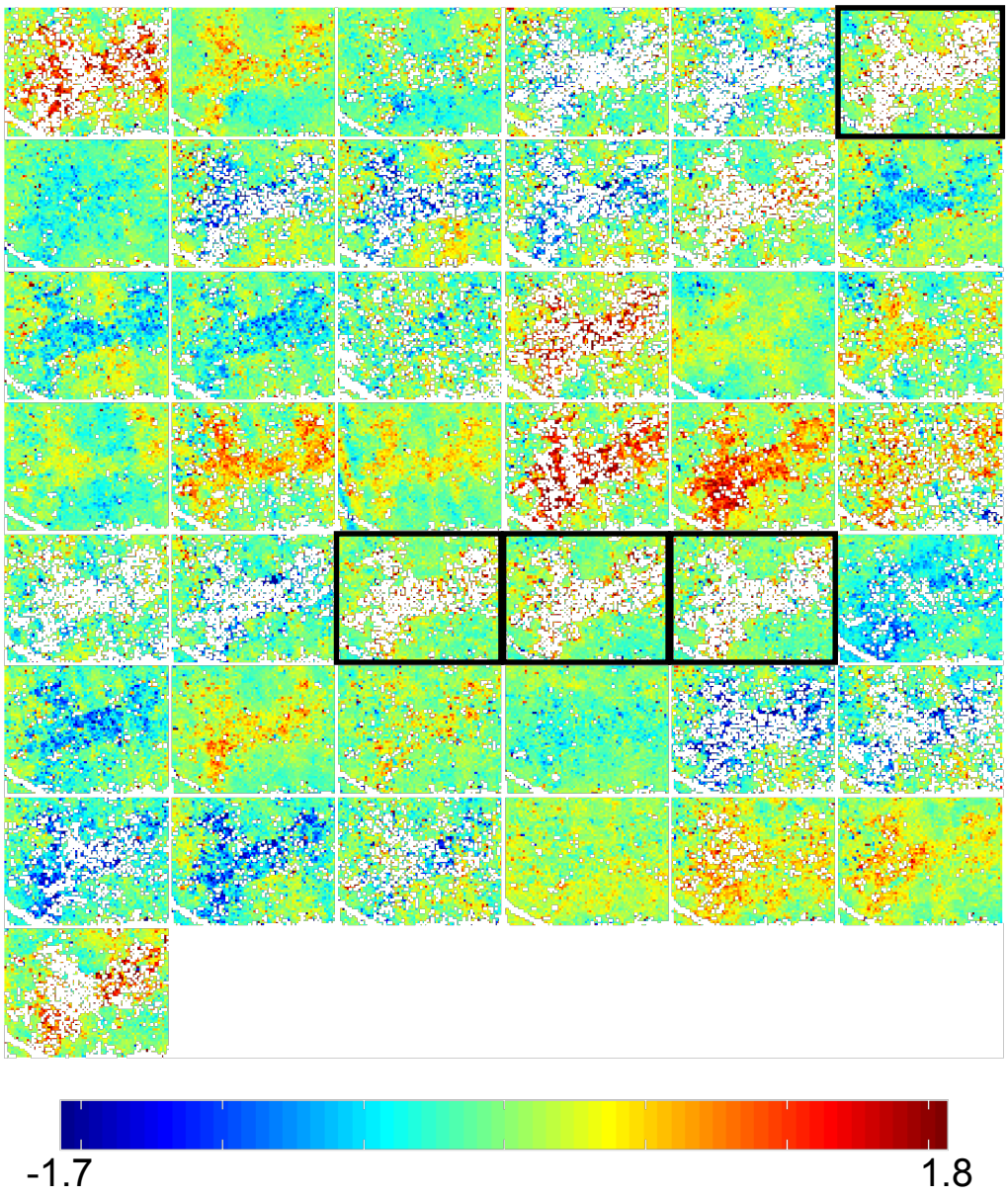

Figure B.2: Unwrapped phase (rad) of ALOS-i. Information of the interferograms are in Table A.1 and A.4. White area is masked because of low coherence. Interferograms framed by black line have longer time interval than a year.

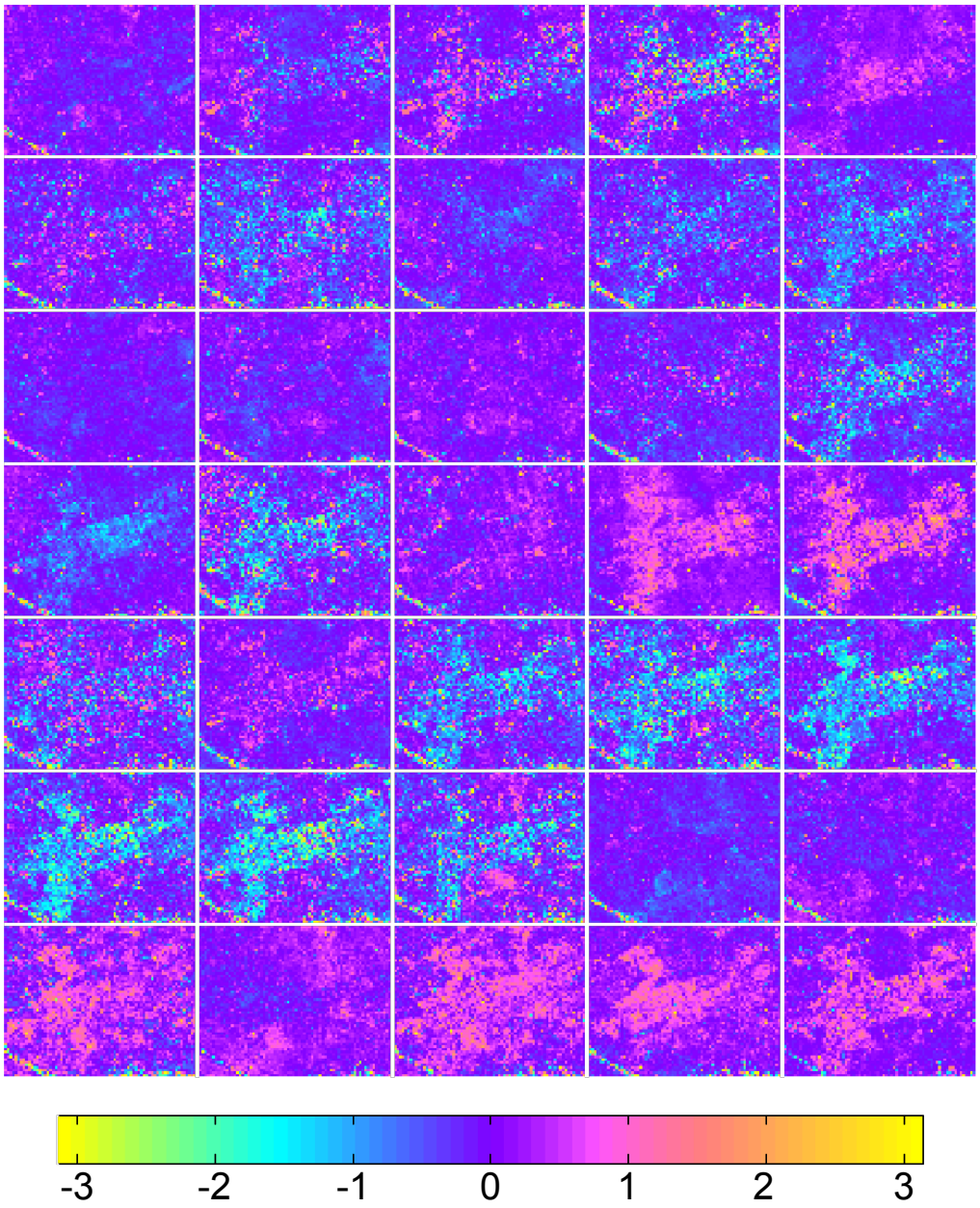

Figure B.3: Wrapped phase (rad) of ALOS-ii. Information of the interferograms are in Table A.1 and A.4.

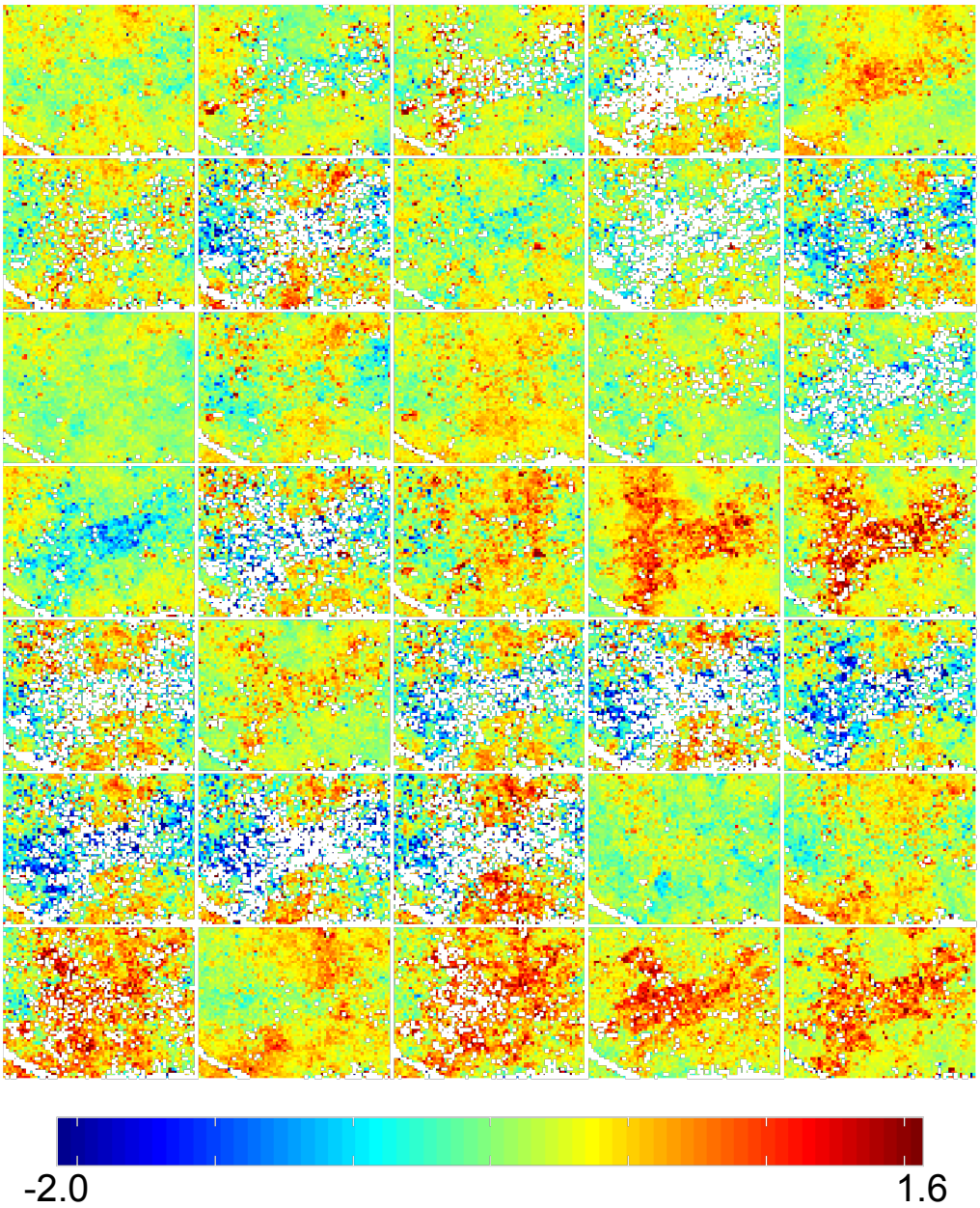

Figure B.4: Unwrapped phase (rad) of ALOS-ii. Information of the interferograms are in Table A.1 and A.4.

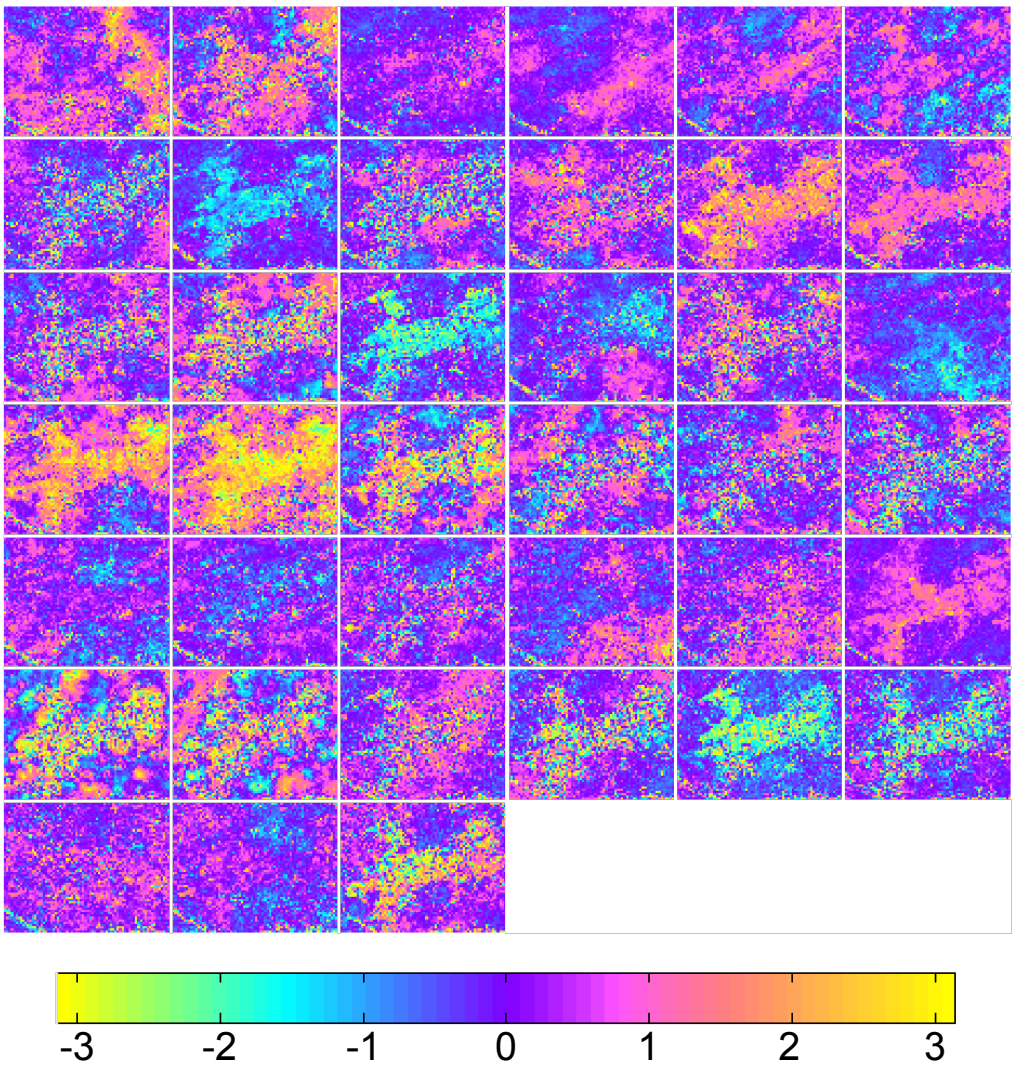

Figure B.5: Wrapped phase (rad) of Envisat. Information of the interferograms are in Table A.2 and A.5.

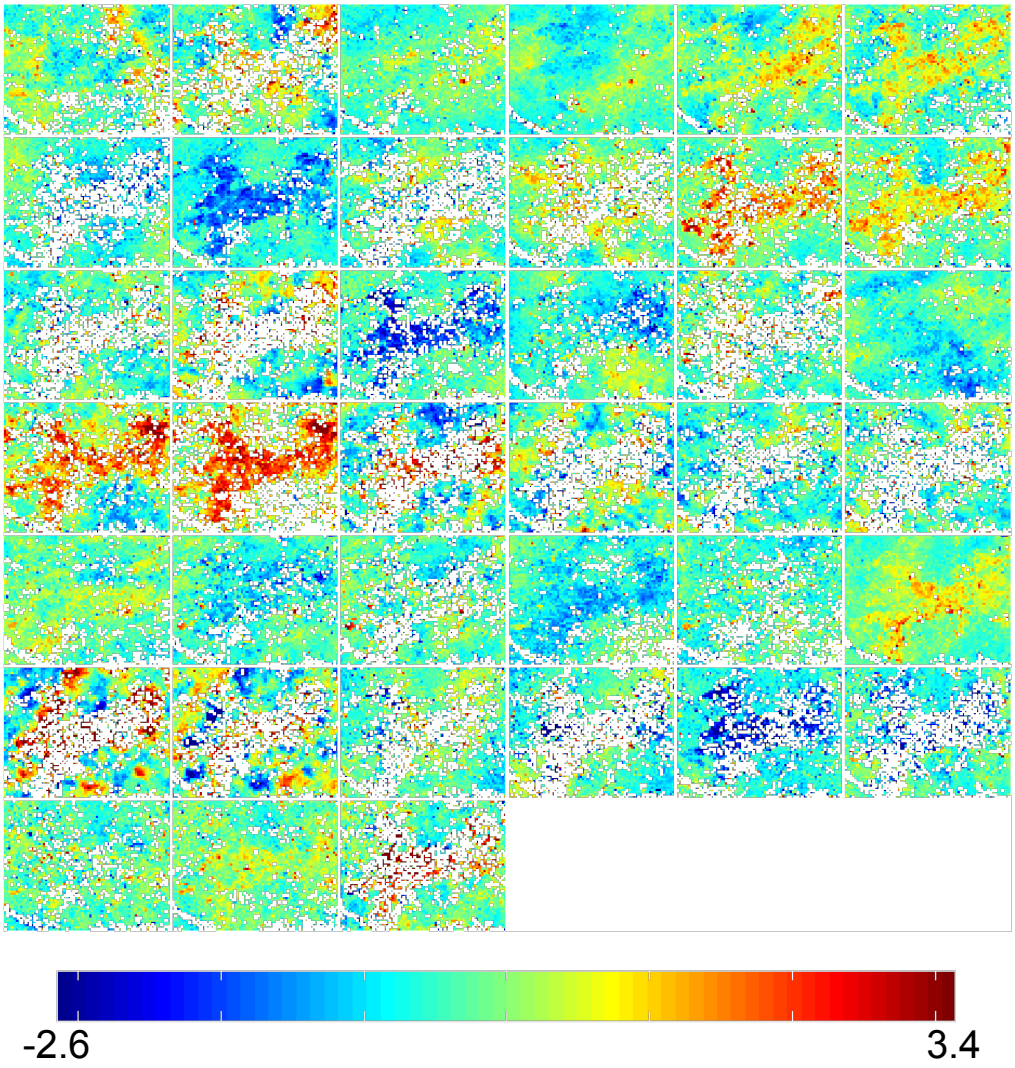

Figure B.6: Unwrapped phase (rad) of Envisat. Information of the interferograms are in Table A.2 and A.5.

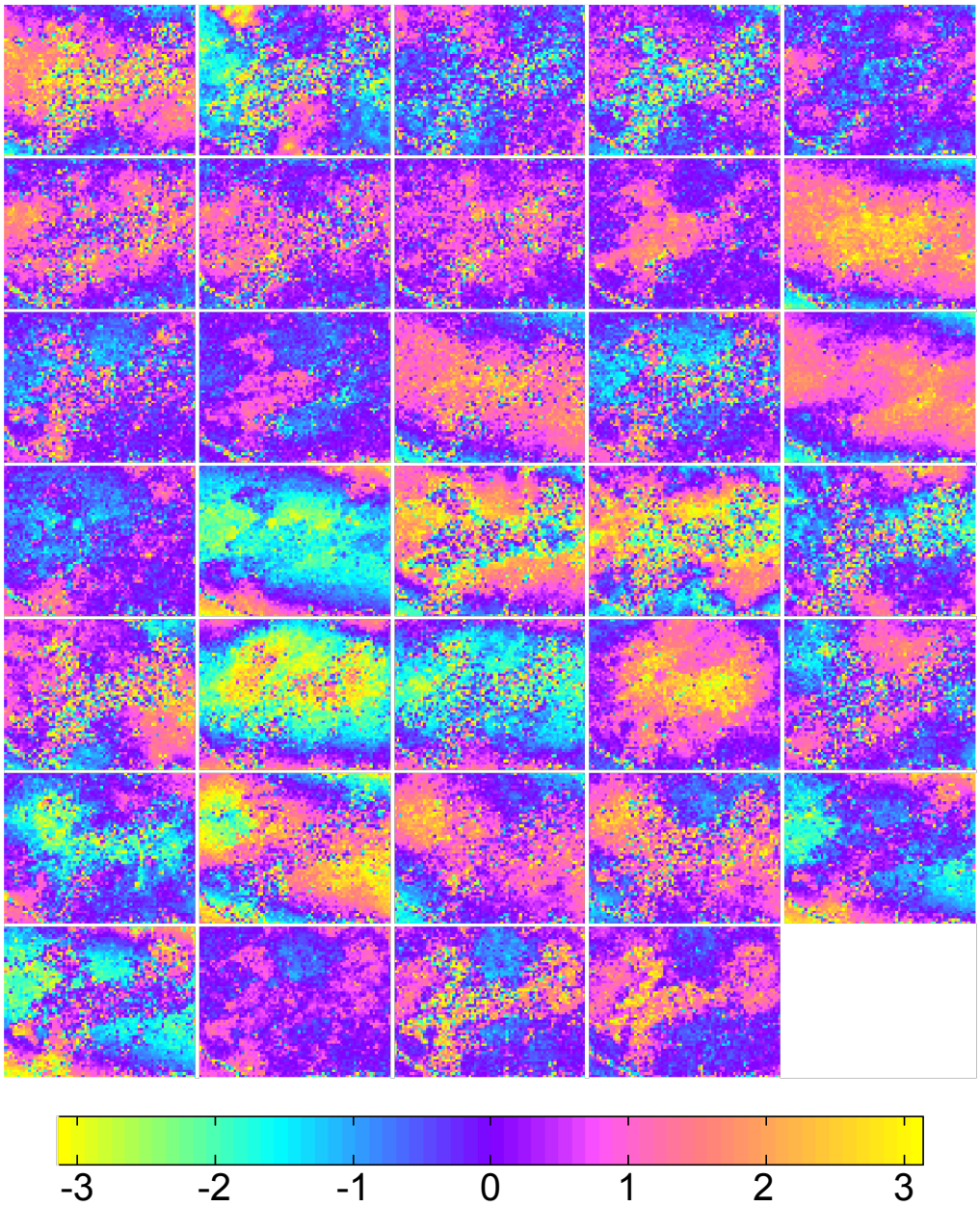

Figure B.7: Wrapped phase (rad) of RS2. Information of the interferograms are in Table A.2 and A.5.

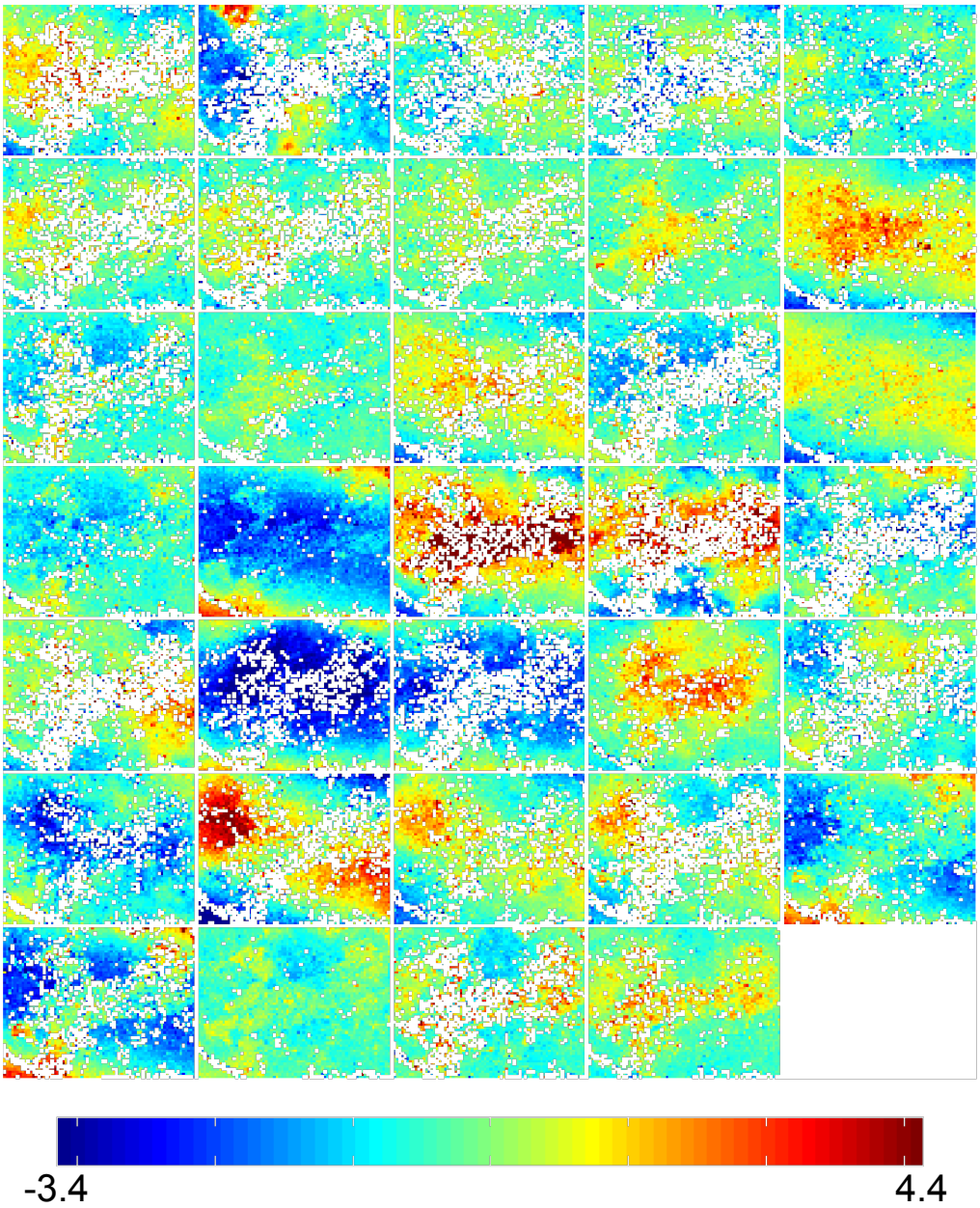

Figure B.8: Unwrapped phase (rad) of RS2. Information of the interferograms are in Table A.2 and A.5.

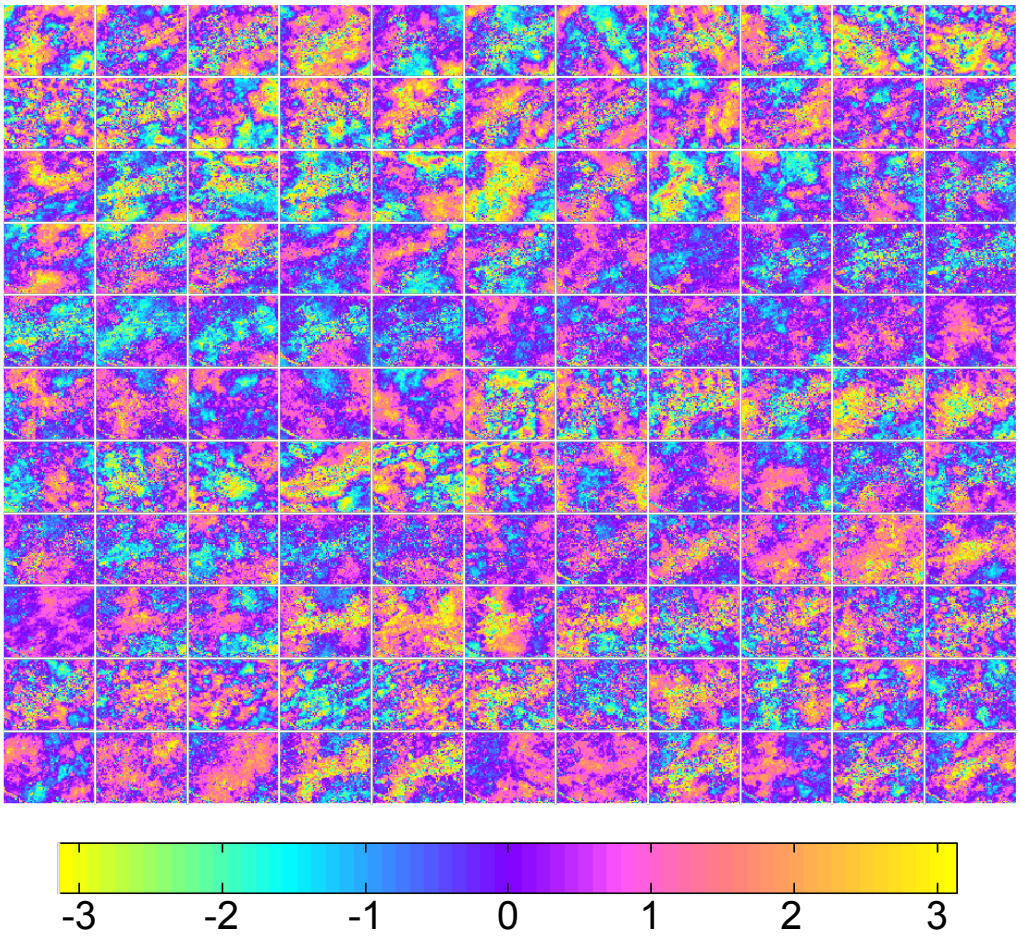

Figure B.9: Wrapped phase (rad) of TSX-A. Information of the interferograms are in Table A.3 and A.6.

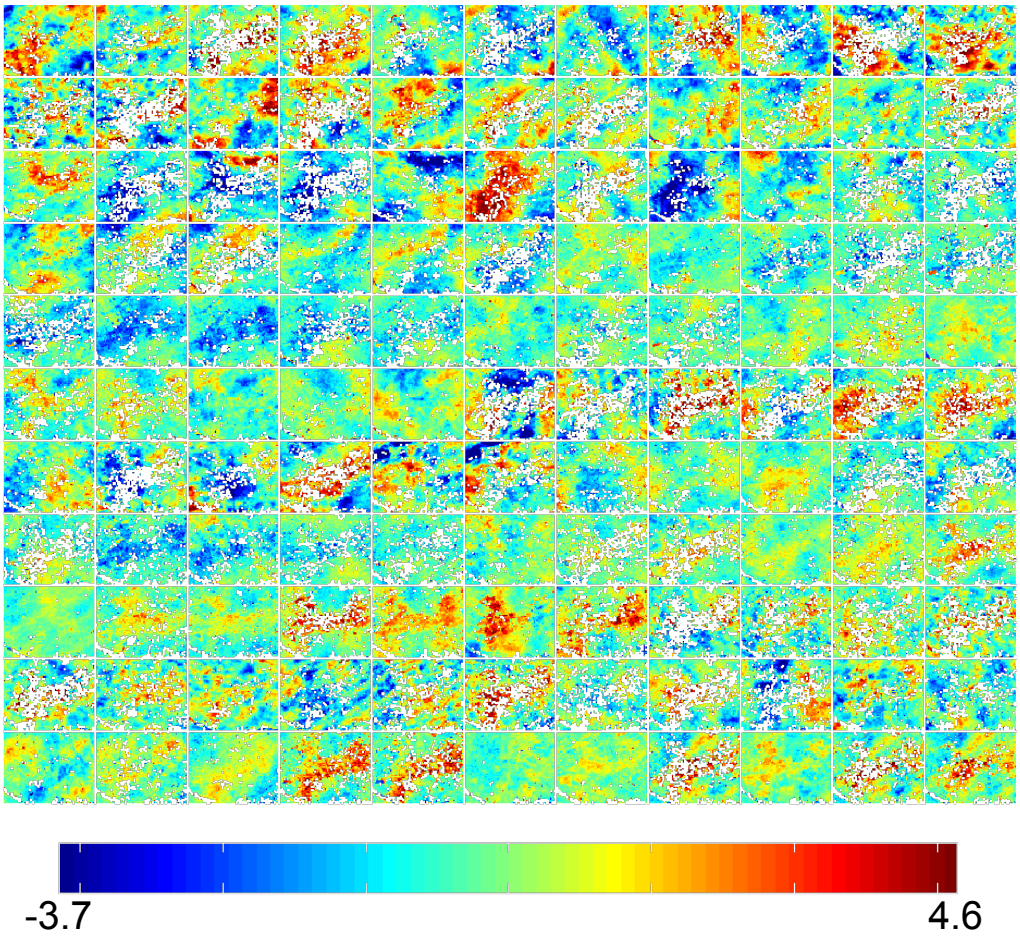

Figure B.10: Unwrapped phase (rad) of TSX-A. Information of the interferograms are in Table A.3 and A.6.

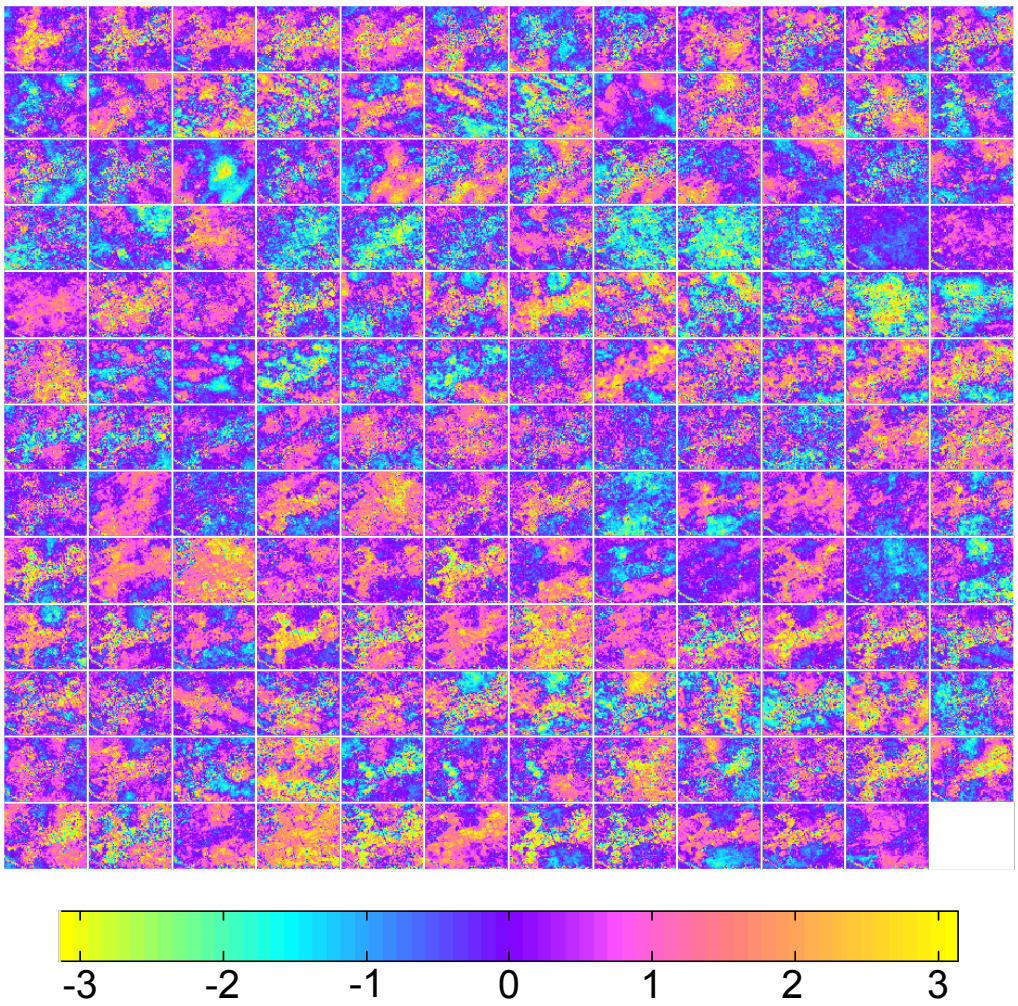

Figure B.11: Wrapped phase (rad) of TSX-D. Information of the interferograms are in Table A.3 and A.7.

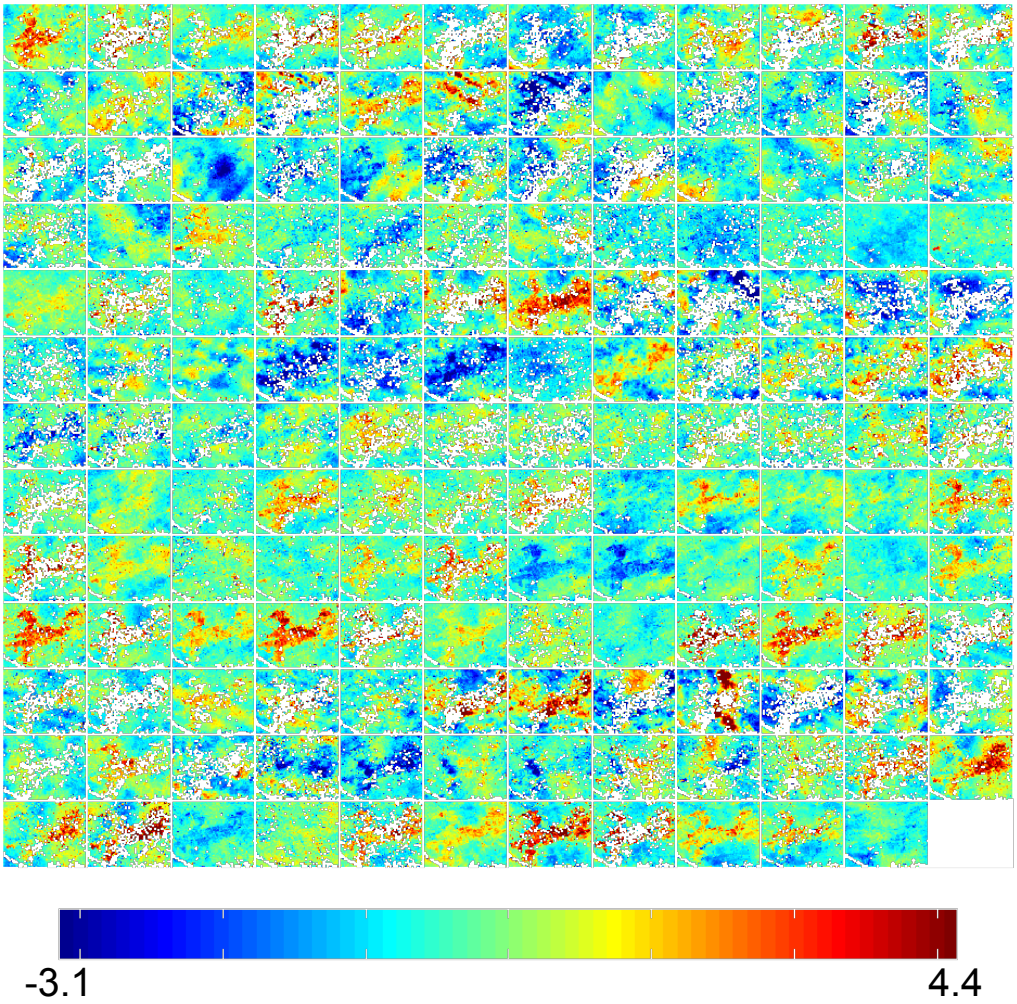

Figure B.12: Unwrapped phase (rad) of TSX-D. Information of the interferograms are in Table A.3 and A.7.

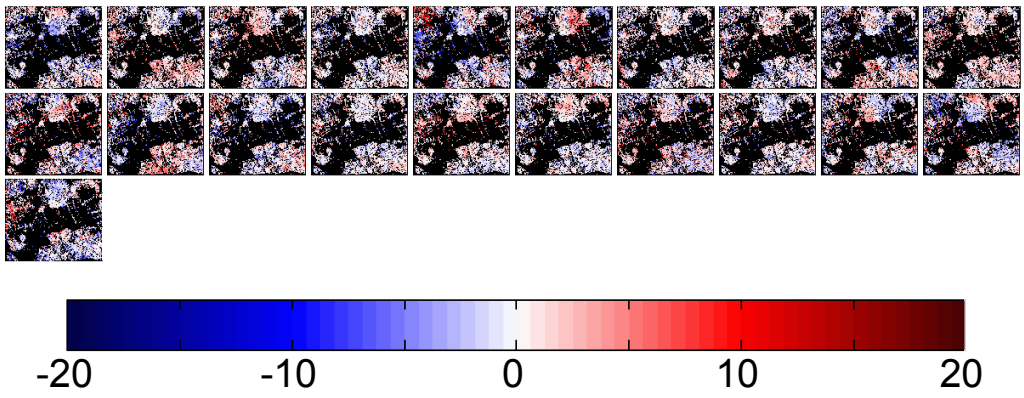

Figure B.13: Estimated APS (mm) of ALOS-i by PSI.

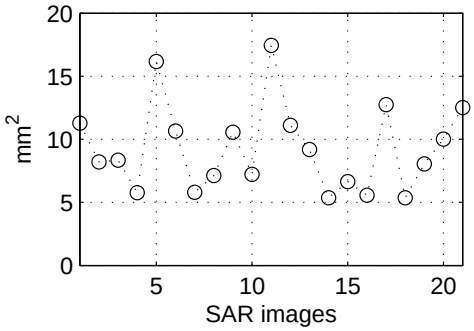

Figure B.14: Variance of APS for each image of ALOS-i.

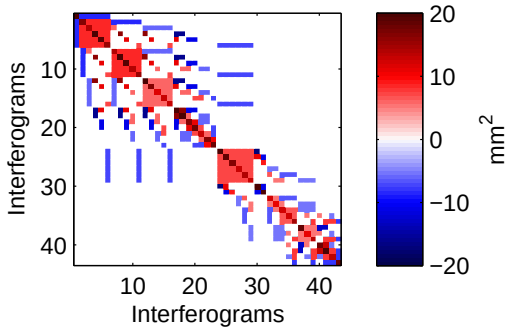

Figure B.15: Variance-covariance matrix of APS of ALOS-i

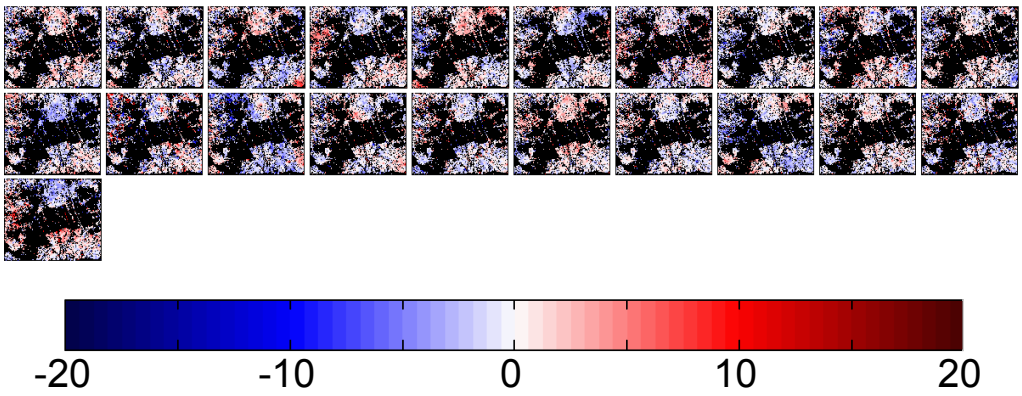

Figure B.16: Estimated APS (mm) of ALOS-ii by PSI.

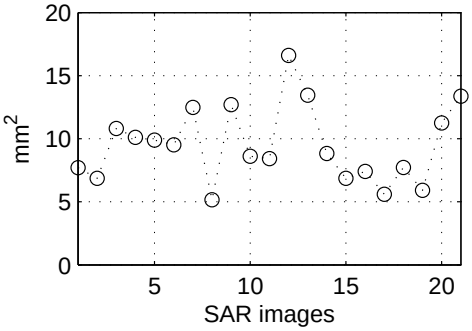

Figure B.17: Variance of APS for each image of ALOS-ii.

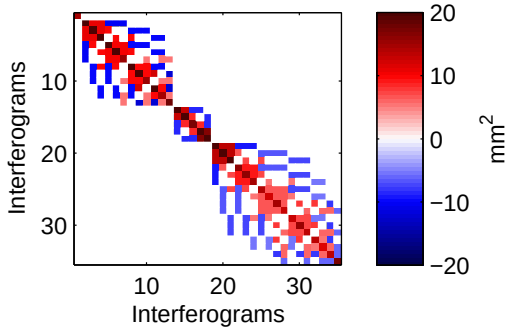

Figure B.18: Variance-covariance matrix of APS of ALOS-ii.

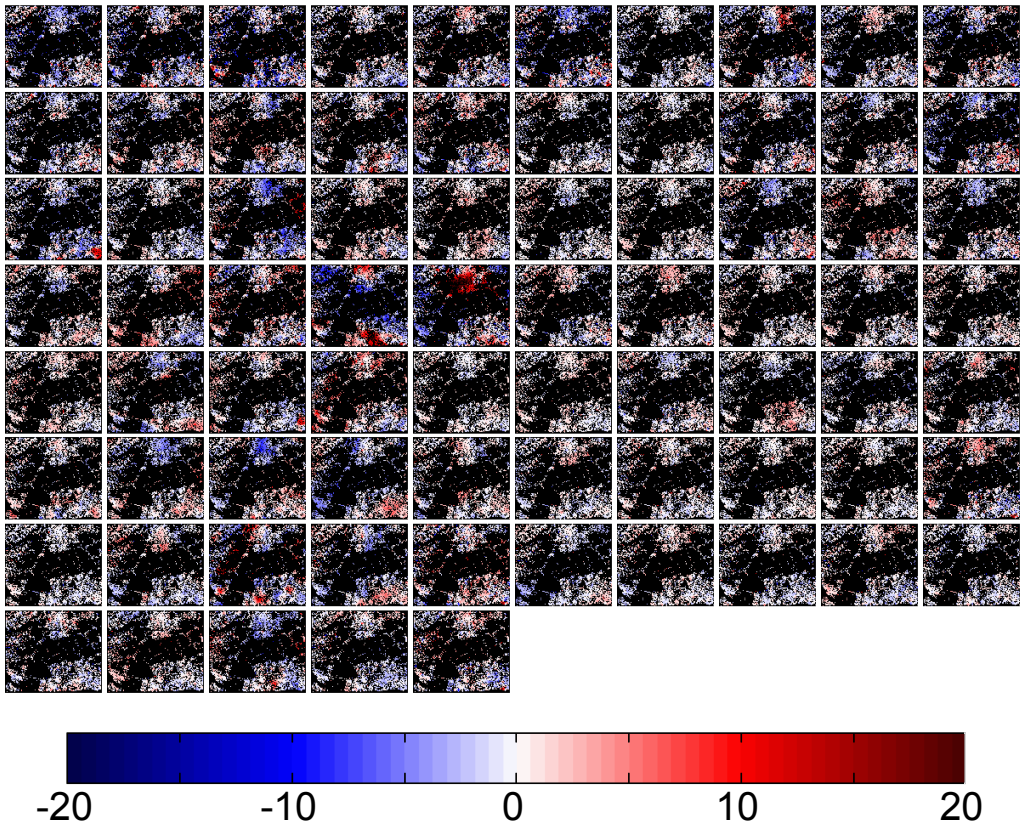

Figure B.19: Estimated APS (mm) of Envisat by PSI.

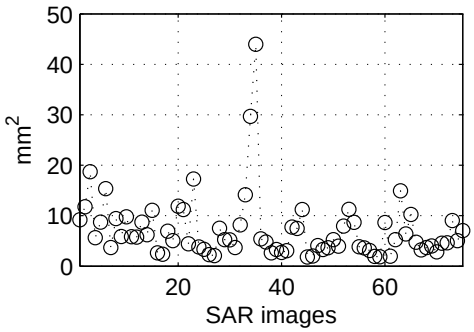

Figure B.20: Variance of APS for each image of Envisat.

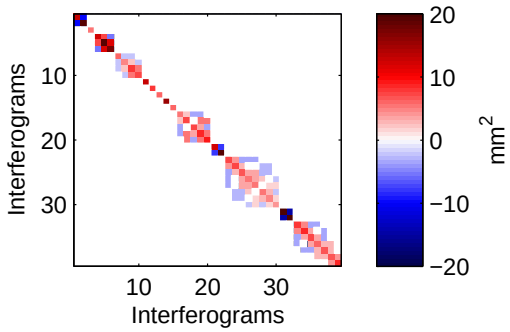

Figure B.21: Variance-covariance matrix of APS of Envisat.

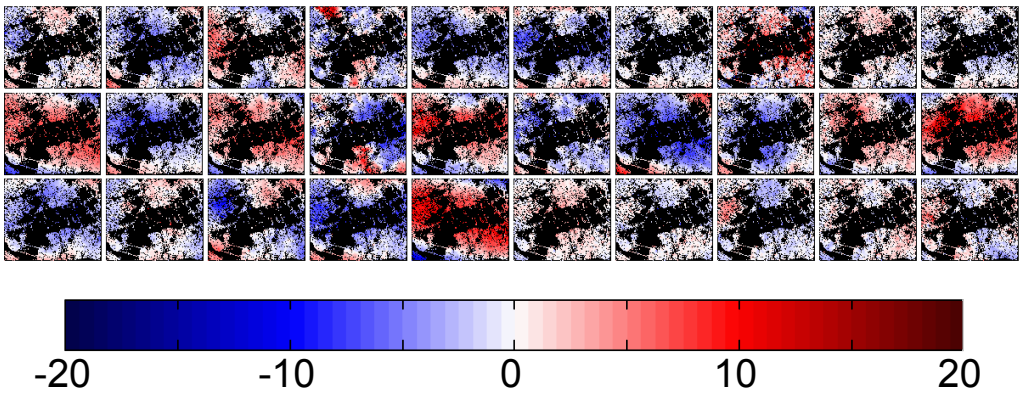

Figure B.22: Estimated APS (mm) of RS2 by PSI.

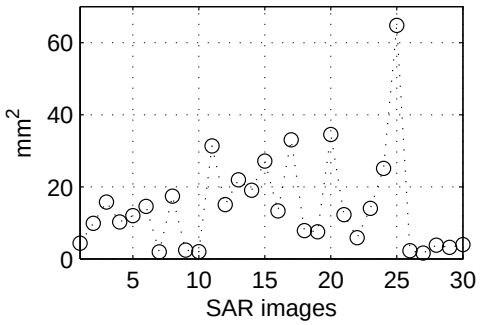

Figure B.23: Variance of APS for each image of RS2.

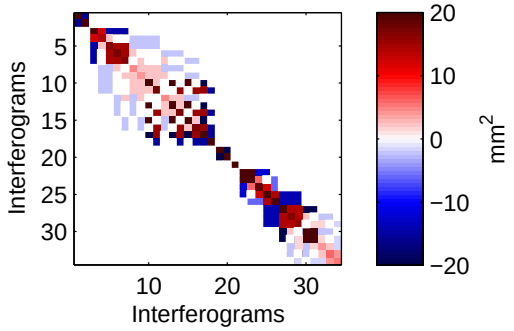

Figure B.24: Variance-covariance matrix of APS of RS2.

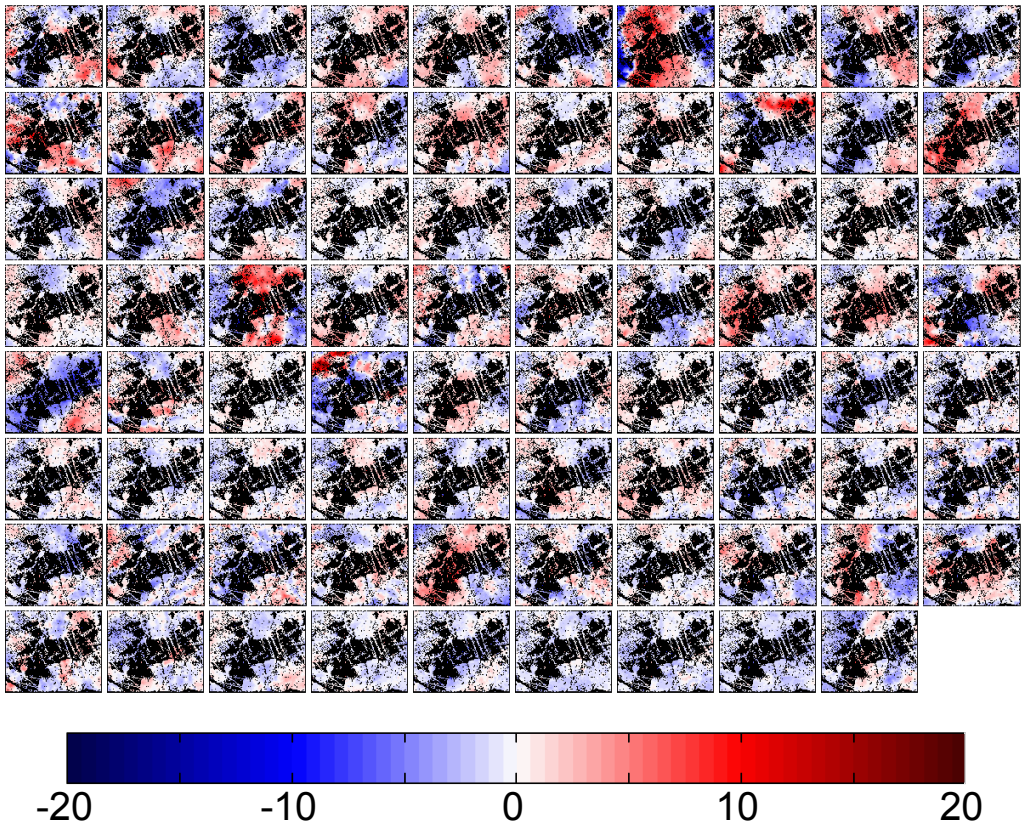

Figure B.25: Estimated APS (mm) of TSX-A by PSI.

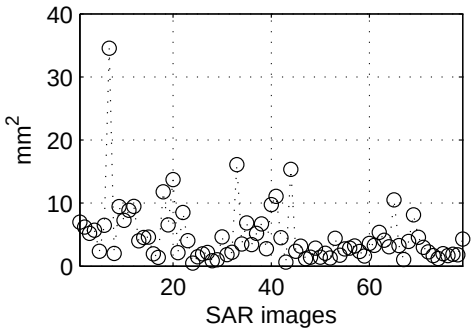

Figure B.26: Variance of APS for each image of TSX-A.

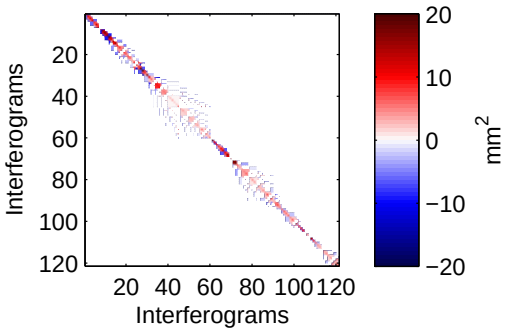

Figure B.27: Variance-covariance matrix of APS of TSX-A.

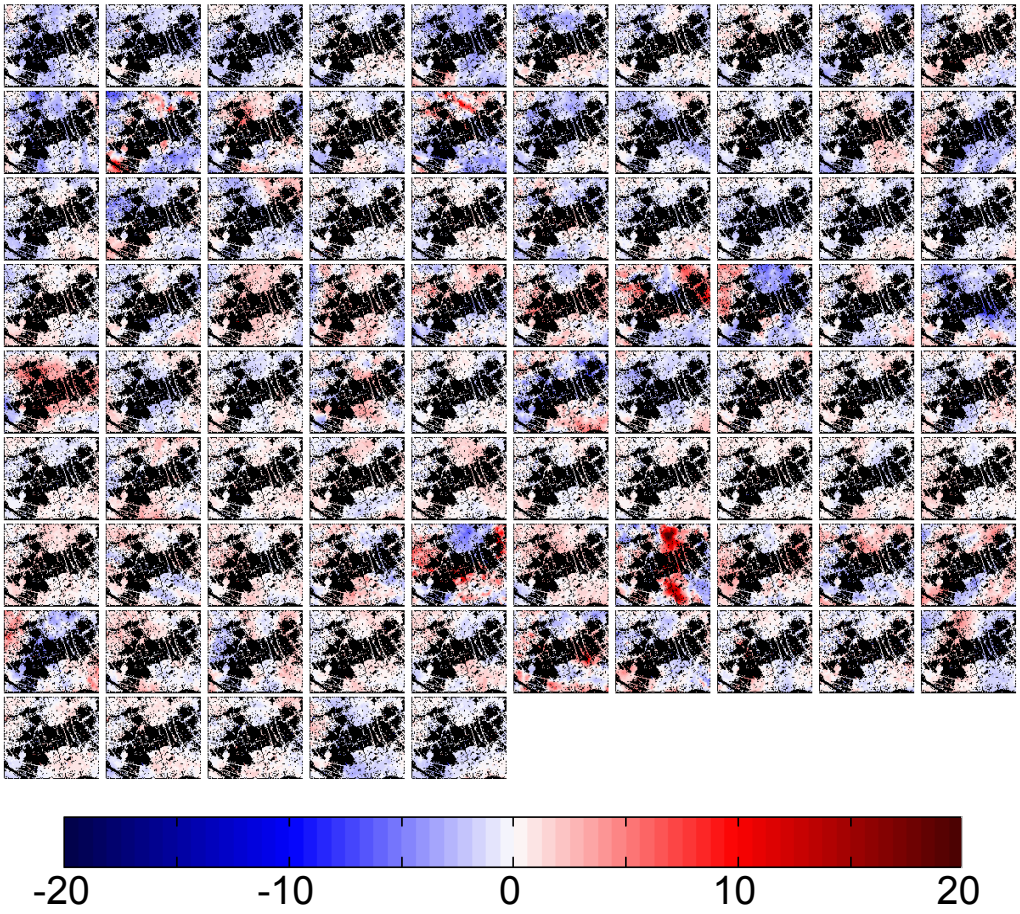

Figure B.28: Estimated APS (mm) of TSX-D by PSI.

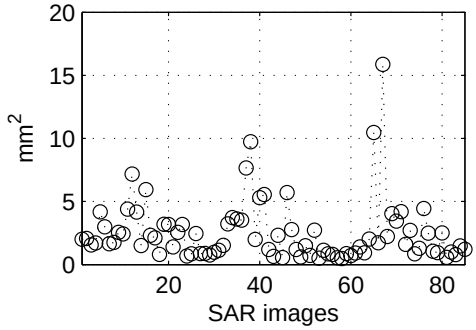

Figure B.29: Variance of APS for each image of TSX-D.

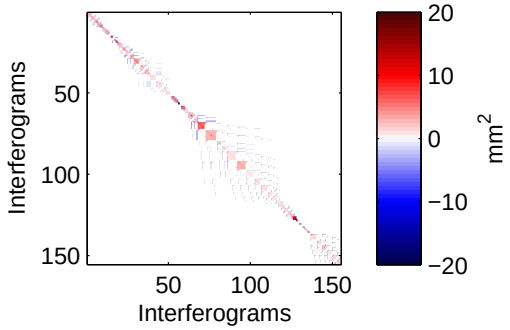

Figure B.30: Variance-covariance matrix of APS of TSX-D.

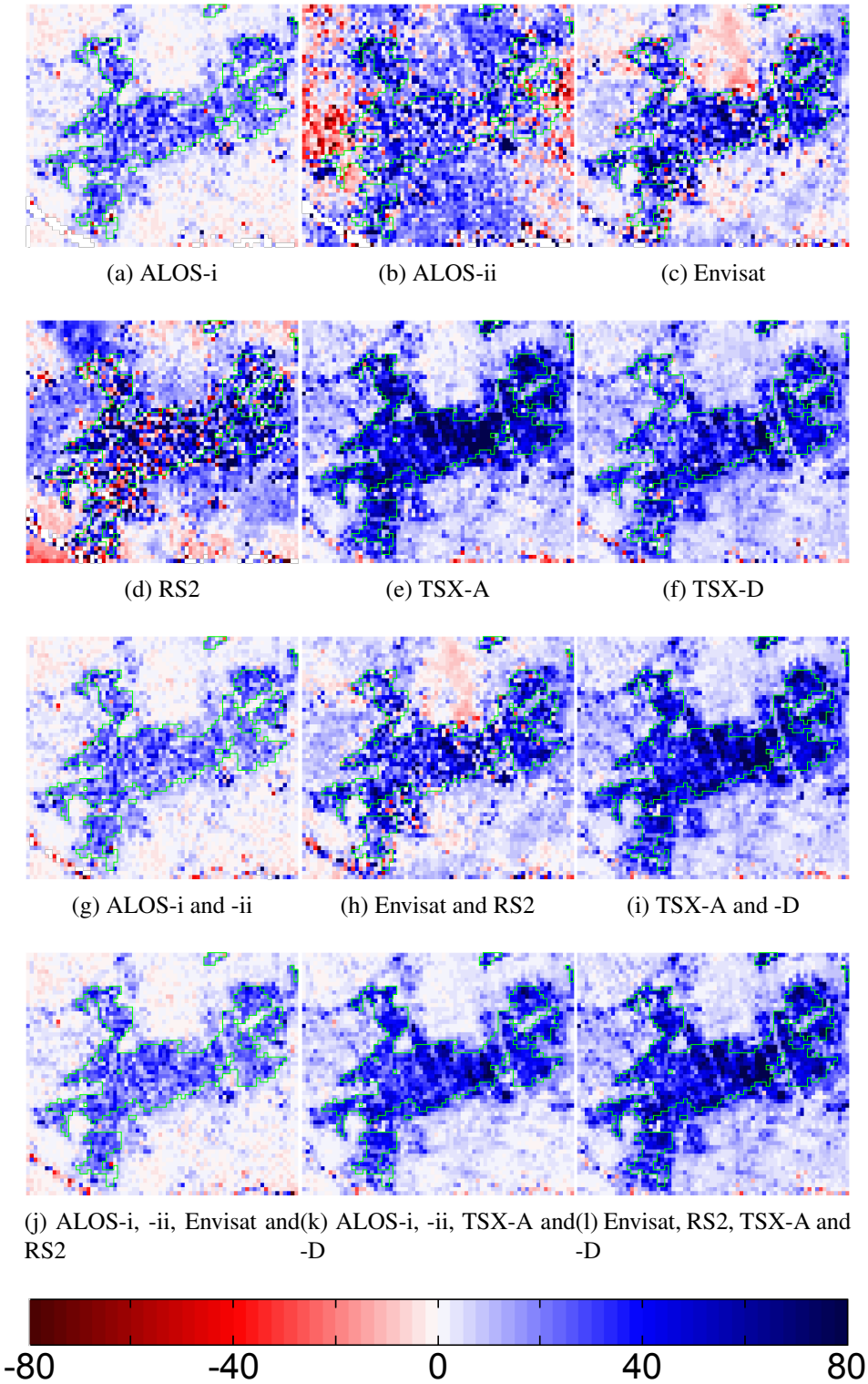

(a) ALOS-i (b) ALOS-ii (c) Envisat

(d) RS2 (e) TSX-A (f) TSX-D

(g) ALOS-i and -ii (h) Envisat and RS2 (i) TSX-A and -D

(j) ALOS-i, -ii, Envisat and RS2 (k) ALOS-i, -ii, TSX-A and -D (l) Envisat, RS2, TSX-A and -D

Figure B.31: Maps of the estimated linear subsidence rate $\hat{v}_v$ (mm/yr) for each and combined data set. Positive values mean subsidence. The area delineated by the polygon corresponds to the pasture.

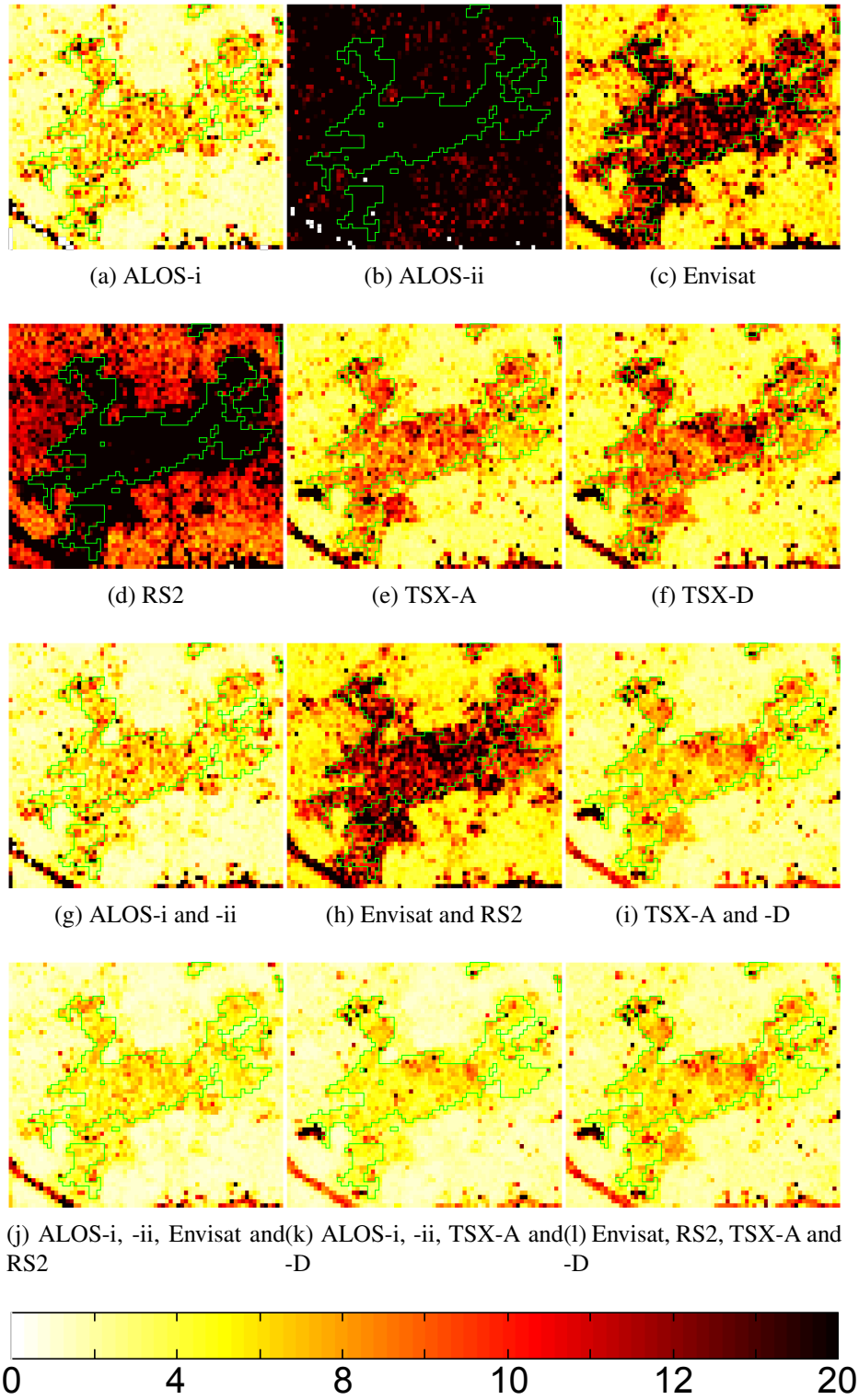

(a) ALOS-i (b) ALOS-ii (c) Envisat

(d) RS2 (e) TSX-A (f) TSX-D

(g) ALOS-i and -ii (h) Envisat and RS2 (i) TSX-A and -D

(j) ALOS-i, -ii, Envisat and RS2 (k) ALOS-i, -ii, TSX-A and -D (l) Envisat, RS2, TSX-A and -D

Figure B.32: Maps of the standard deviations of linear subsidence rate $\sigma_{\hat{v}_v}$ (mm/yr) for each and combined data set. The area delineated by the polygon corresponds to the pasture.

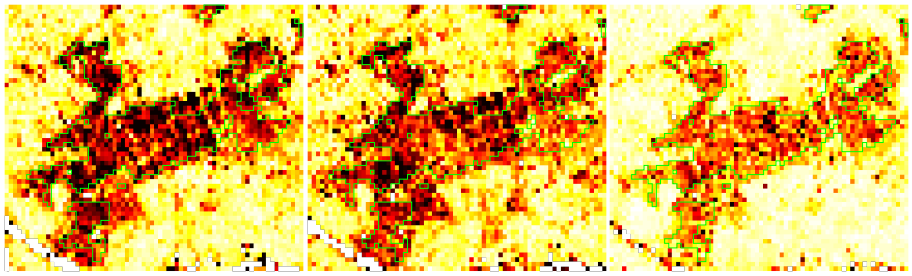

(a) ALOS-i (b) ALOS-ii (c) Envisat

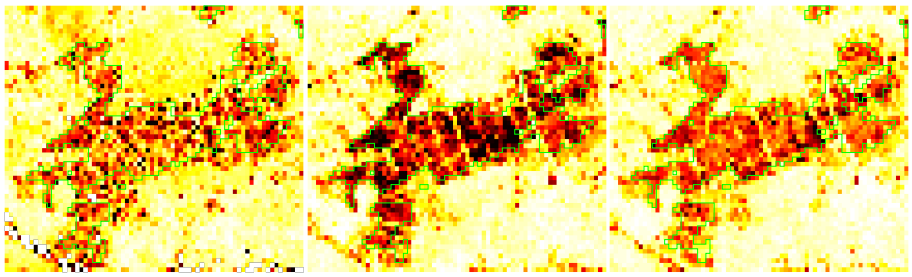

(d) RS2 (e) TSX-A (f) TSX-D

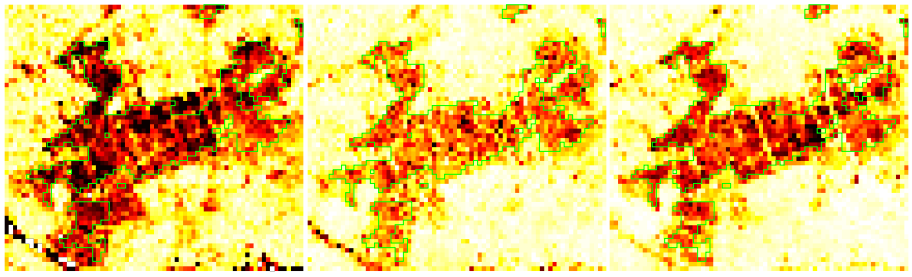

(g) ALOS-i and -ii (h) Envisat and RS2 (i) TSX-A and -D

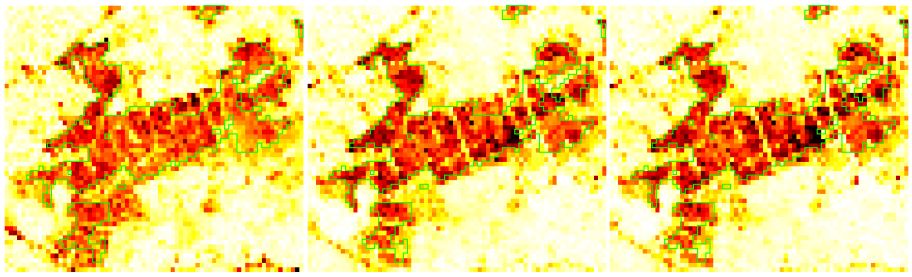

(j) ALOS-i, -ii, Envisat and RS2 (k) ALOS-i, -ii, TSX-A and -D (l) Envisat, RS2, TSX-A and -D

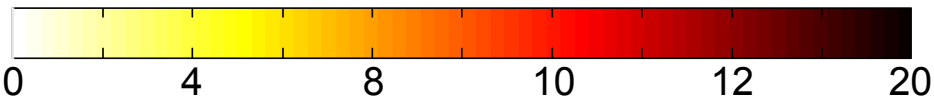

Figure B.33: Maps of the estimated amplitude of the seasonal periodic deformation $\hat{A}_{\mathrm{v}}$ (mm) for each and combined data set. The area delineated by the polygon corresponds to the pasture.

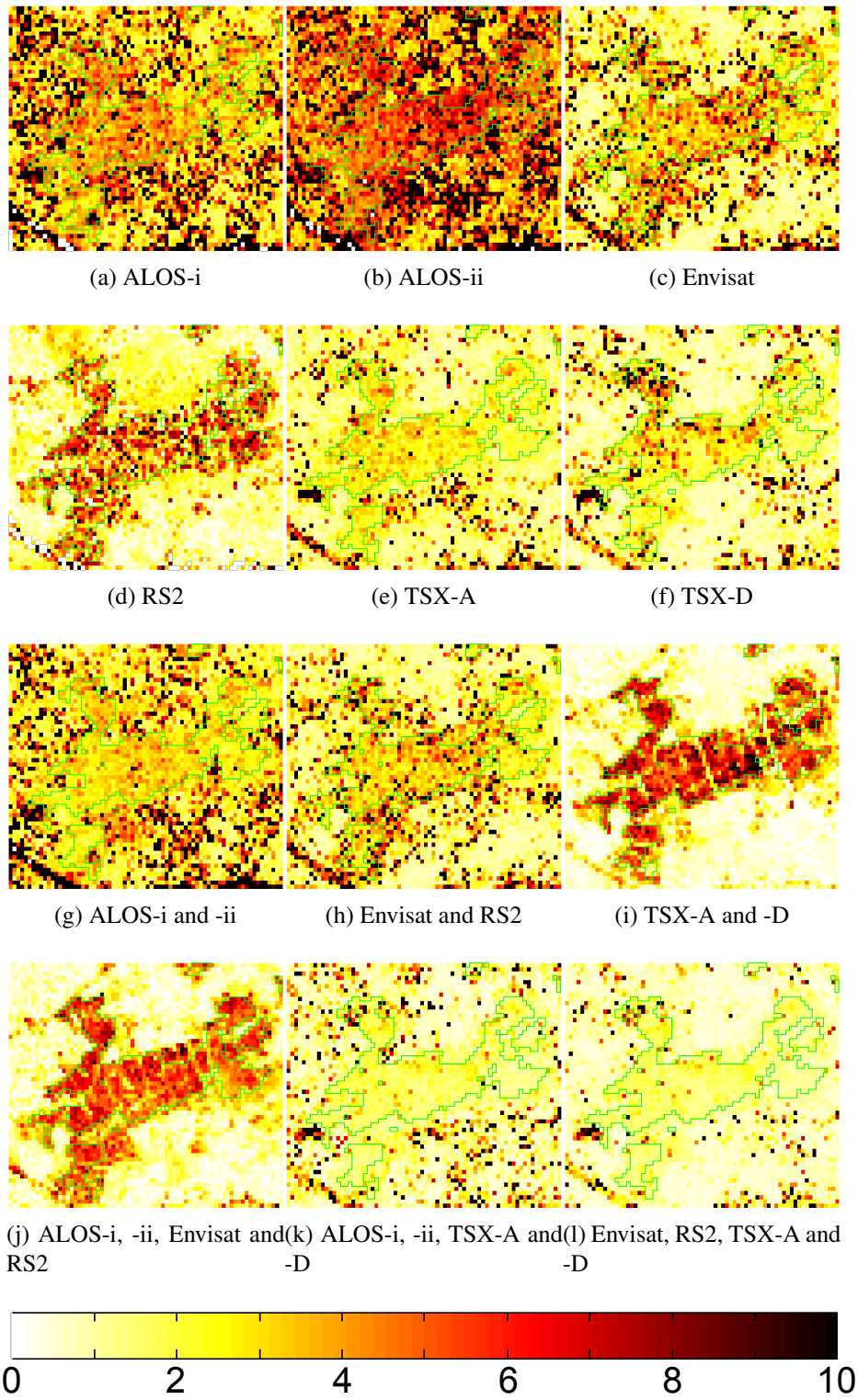

(a) ALOS-i (b) ALOS-ii (c) Envisat

(d) RS2 (e) TSX-A (f) TSX-D

(g) ALOS-i and -ii (h) Envisat and RS2 (i) TSX-A and -D

(j) ALOS-i, -ii, Envisat and RS2 (k) ALOS-i, -ii, TSX-A and -D (l) Envisat, RS2, TSX-A and -D

Figure B.34: Maps of the standard deviations of the amplitude of the seasonal periodic deformation $\sigma_{\hat{A}_v}$ (mm) for each and combined data set. The area delineated by the polygon corresponds to the pasture.

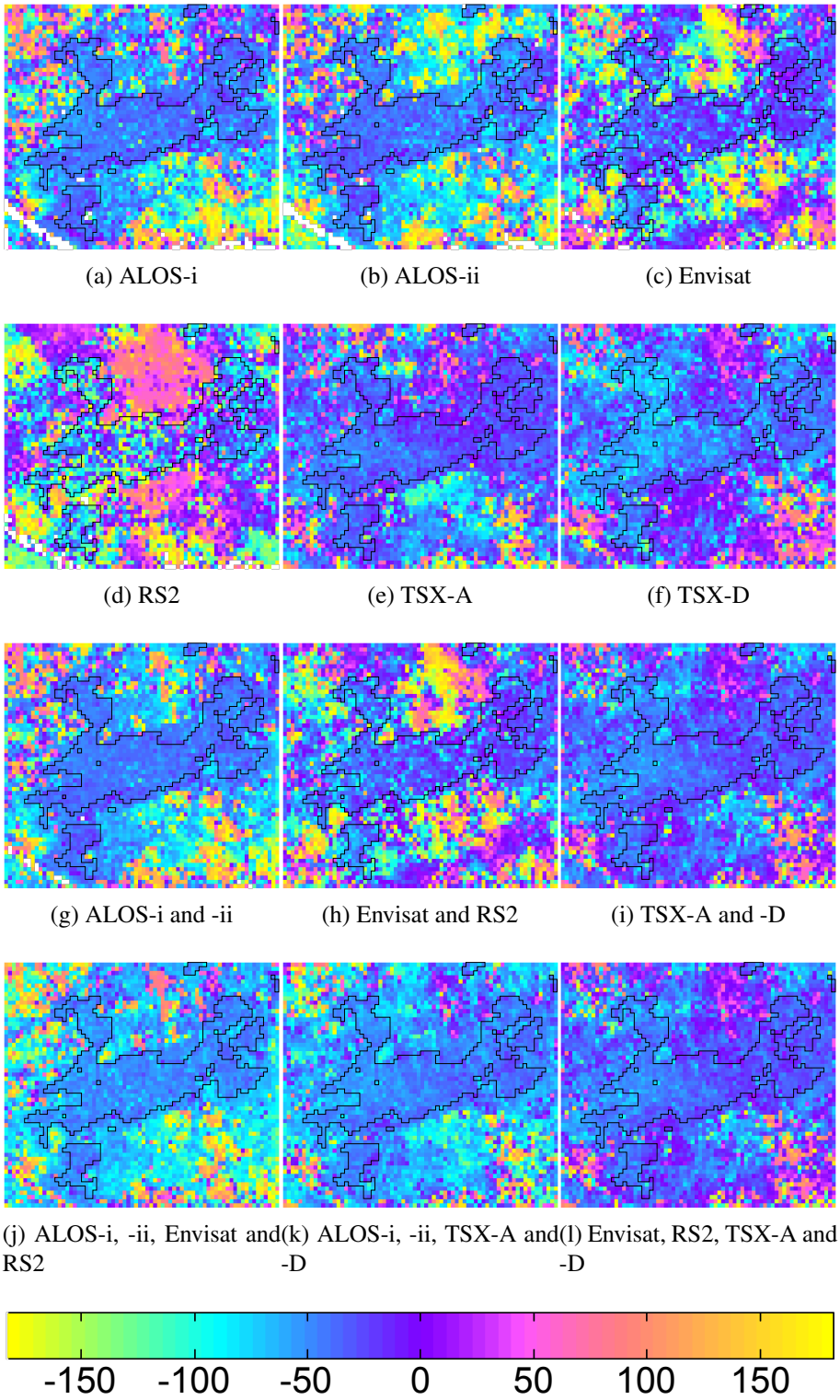

(a) ALOS-i (b) ALOS-ii (c) Envisat

(d) RS2 (e) TSX-A (f) TSX-D

(g) ALOS-i and -ii (h) Envisat and RS2 (i) TSX-A and -D

(j) ALOS-i, -ii, Envisat and RS2 (k) ALOS-i, -ii, TSX-A and -D (l) Envisat, RS2, TSX-A and -D

Figure B.35: Maps of the estimated time offset of the seasonal periodic deformation $\hat{\Delta t}$ (day) with reference to 1 January for each and combined data set. The area delineated by the polygon corresponds to the pasture.

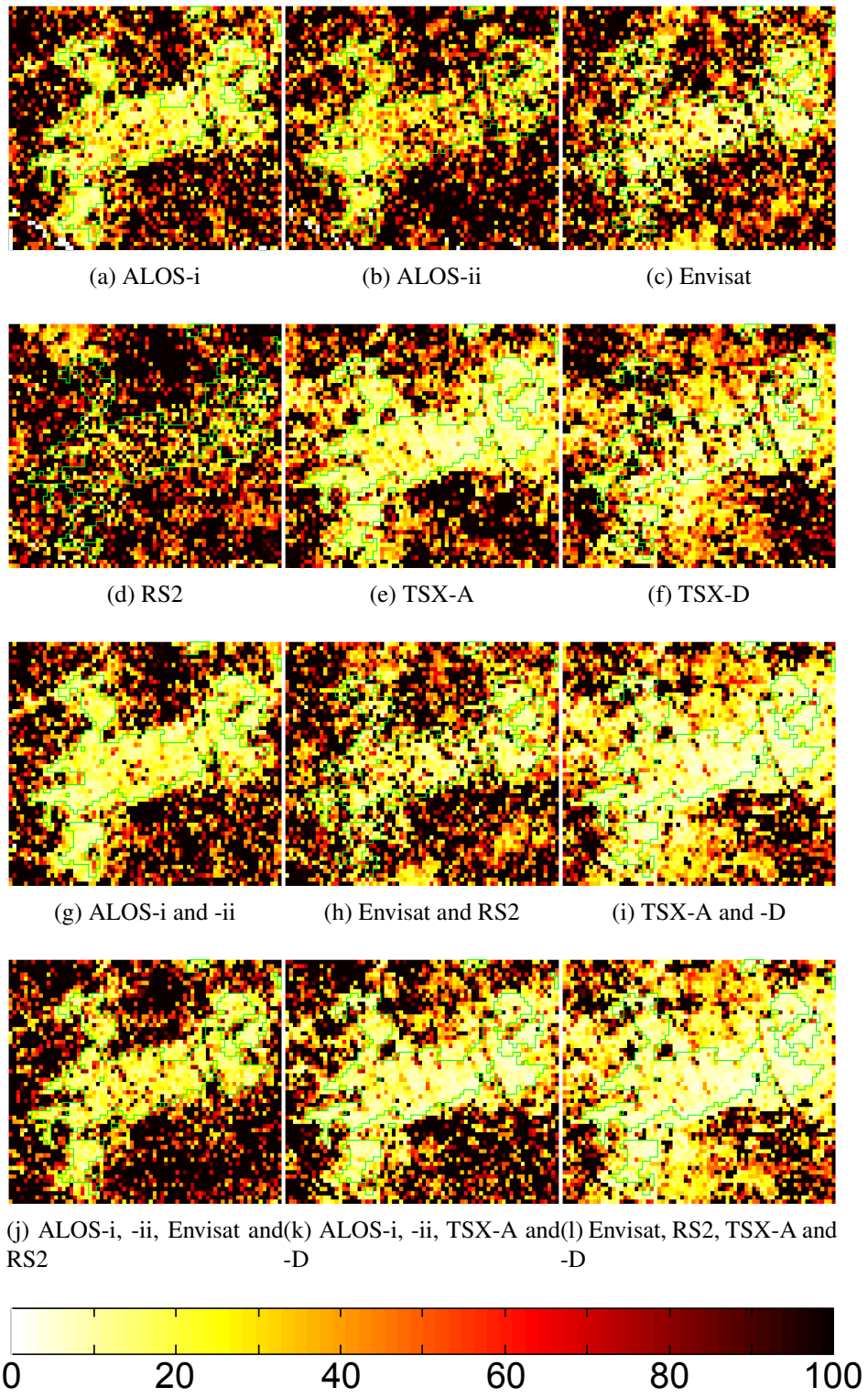

(a) ALOS-i (b) ALOS-ii (c) Envisat

(d) RS2 (e) TSX-A (f) TSX-D

(g) ALOS-i and -ii (h) Envisat and RS2 (i) TSX-A and -D

(j) ALOS-i, -ii, Envisat and RS2 (k) ALOS-i, -ii, TSX-A and -D (l) Envisat, RS2, TSX-A and -D

Figure B.36: Maps of the standard deviations of the amplitude of the seasonal periodic deformation $\sigma_{\hat{\Delta}t}$ (day) for each and combined data set. The area delineated by the polygon corresponds to the pasture.

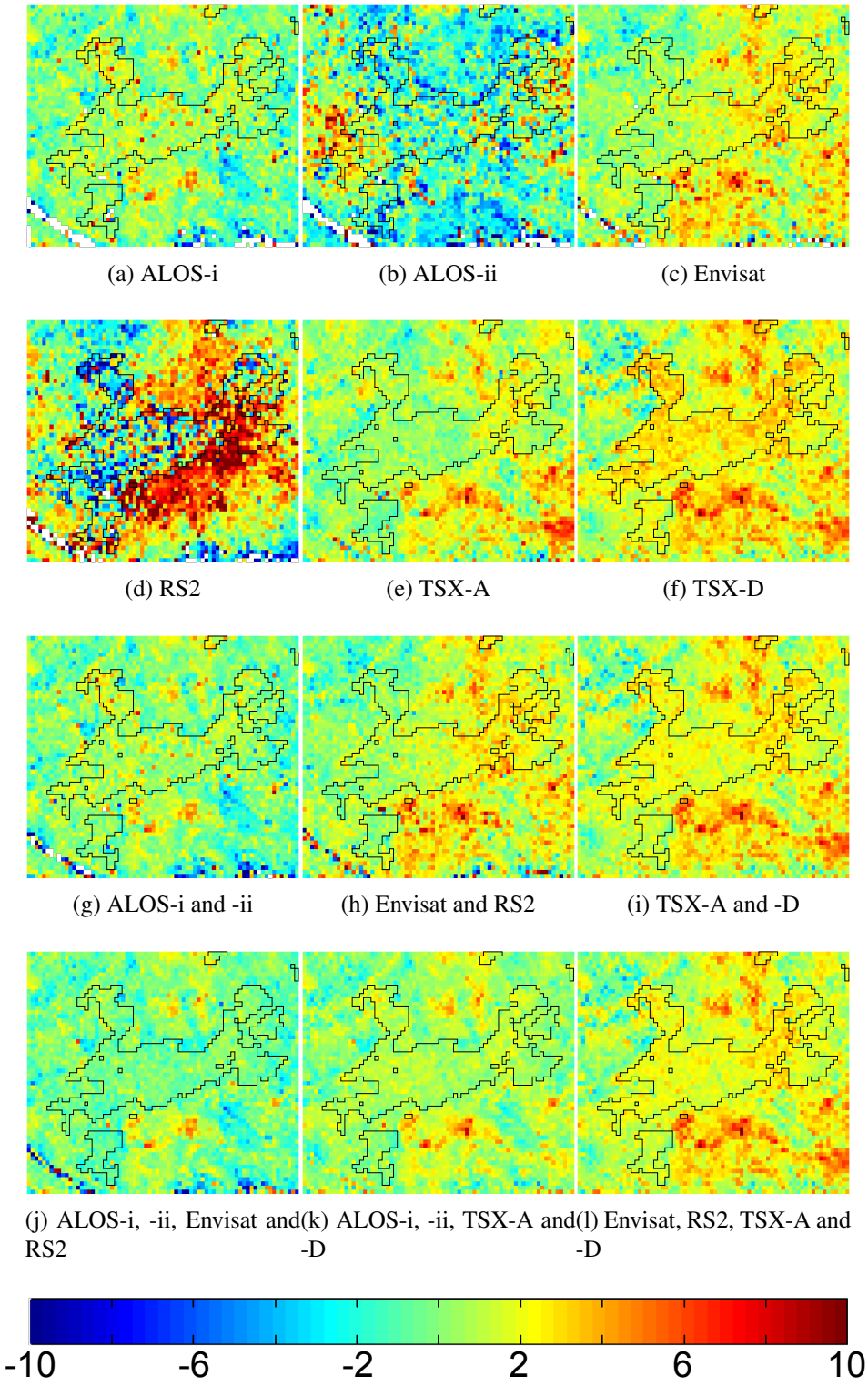

(a) ALOS-i (b) ALOS-ii (c) Envisat

(d) RS2 (e) TSX-A (f) TSX-D

(g) ALOS-i and -ii (h) Envisat and RS2 (i) TSX-A and -D

(j) ALOS-i, -ii, Envisat and RS2 (k) ALOS-i, -ii, TSX-A and -D (l) Envisat, RS2, TSX-A and -D

Figure B.37: Maps of the estimated DEM error $\hat{\Delta z}$ (m) for each and combined data set. The area delineated by the polygon corresponds to the pasture.

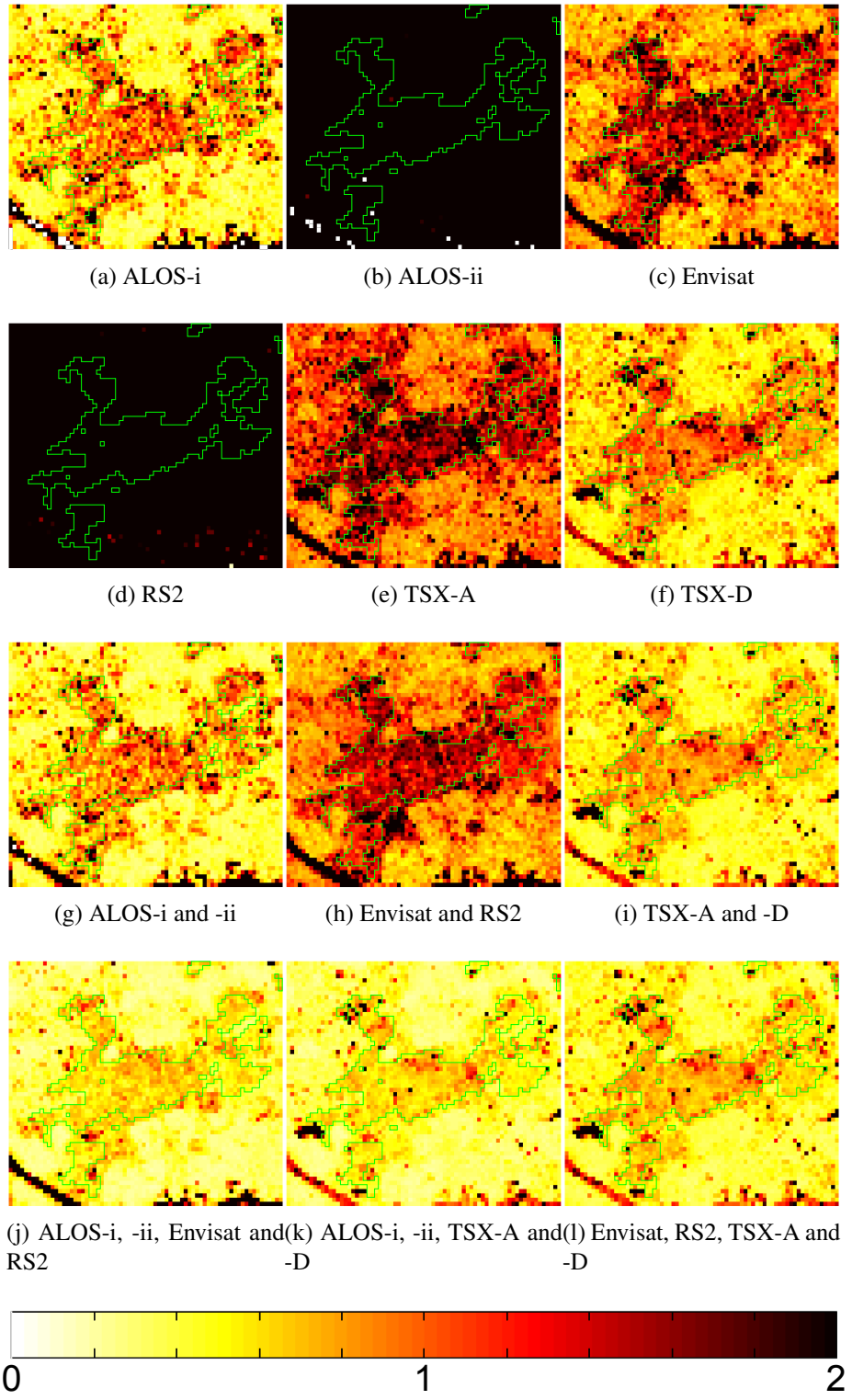

(a) ALOS-i (b) ALOS-ii (c) Envisat

(d) RS2 (e) TSX-A (f) TSX-D

(g) ALOS-i and -ii (h) Envisat and RS2 (i) TSX-A and -D

(j) ALOS-i, -ii, Envisat and RS2 (k) ALOS-i, -ii, TSX-A and -D (l) Envisat, RS2, TSX-A and -D

Figure B.38: Maps of the standard deviations of the DEM error $\sigma_{\hat{\Delta}z}$ (m) for each and combined data set. The area delineated by the polygon corresponds to the pasture.

Bibliography

T. Abe, M. Furuya, and Y. Takada. Nonplanar fault source modeling of the 2008 Mw 6.9 Iwate-Miyagi inland earthquake in northeast Japan. *Bulletin of the Seismological Society of America*, 103(1):507–518, 2013.

V. Akbari and M. Motagh. Improved ground subsidence monitoring using small baseline SAR interferograms and a weighted least squares inversion algorithm. *IEEE Geoscience and Remote Sensing Letters*, 9(3):437–441, 2012.

A. Aobpaet, M.C. Cuenca, A. Hooper, and I. Trisirisatayawong. InSAR time-series analysis of land subsidence in Bangkok, Thailand. *International Journal of Remote Sensing*, 34(8):2969–2982, 2013.

M. Arikan and R.F. Hanssen. Structural deformation of the high-speed line (HSL) infrastructure in The Netherlands; observations using satellite radar interferometry. In *13th FIG International Symposium on Deformation Measurements and Analysis, Lisbon, Portugal*, pages 12–15, 2008.

M. Arıkan, A. Hooper, and R.F. Hanssen. Radar time series analysis over west anatolia. In *European Space Agency (Special Publication) ESA SP-677*, 2010.

M. Arimoto, Y. Fukushima, M. Hashimoto, and Y. Takada. Land subsi-

dence in Semarang, Indonesia, observed by InSAR time-series analysis using ALOS/PALSAR data (in Japanese with abstract and figure captions in English). *Journal of the Geodetic Society of Japan*, 59(2):45–56, 2013.

R. Bamler. The SRTM mission: A world-wide 30 m resolution DEM from SAR interferometry in 11 days. In *Photogrammetric week*, volume 99, pages 145–154. Berlin, Germany: Wichmann Verlag, 1999.

R. Bamler and P. Hartl. Synthetic aperture radar interferometry. *Inverse problems*, 14:R1, 1998.

K.B. Bartlett and R.C. Harriss. Review and assessment of methane emissions from wetlands. *Chemosphere*, 26(1):261–320, 1993.

P. Berardino, G. Fornaro, R. Lanari, and E. Sansosti. A new algorithm for surface deformation monitoring based on small baseline differential SAR interferograms. *IEEE Transactions on Geoscience and Remote Sensing*, 40(11):2375–2383, 2002.

F. Casu, M. Manzo, and R. Lanari. A quantitative assessment of the SBAS algorithm performance for surface deformation retrieval from DInSAR data. *Remote Sensing of Environment*, 102(3):195–210, 2006.

J. Champenois, V. Pinel, S. Baize, L. Audin, H. Jomard, A. Hooper, A. Alvarado, and H. Yepes. Large-scale inflation of Tungurahua volcano (Ecuador) revealed by Persistent Scatterers SAR interferometry. *Geophysical Research Letters*, 41(16): 5821–5828, 2014.

L Chang and R.F. Hanssen. Near real-time, semi-recursive, deformation monitoring

of infrastructure using satellite radar interferometry. In *Geoscience and Remote Sensing Symposium (IGARSS), 2012 IEEE International*, pages 1876–1879, 2012.

L. Chang and R.F. Hanssen. Detection of cavity migration and sinkhole risk using radar interferometric time series. *Remote Sensing of Environment*, 147:56 – 64, 2014.

M. Crosetto, O. Monserrat, N. Adam, A. Parizzi, C. Bremmer, S. Dortland, R.F. Hanssen, and F.J. van Leijen. Validation of existing processing chains in Trrafirma stage 2 Final report. http://www.terrafirma.eu.com/validation/ValProj/Final%20Reports/ValProj_Final_report.pdf, 2008.

M.C. Cuenca and R.F. Hanssen. Subsidence due to peat decomposition in the Netherlands, kinematic observations from radar interferometry. In *Proceedings of Fringe 2007 Workshop*, 2007.

J.C. Curlander and R.N. McDonough. *Synthetic aperture radar*. John Wiley & Sons New York, NY, USA, 1991.

M.P. Doin, S. Guillaso, R. Jolivet, C. Lasserre, F. Lodge, G. Ducret, and R. Grandin. Presentation of the small baseline NSBAS processing chain on a case example: The Etna deformation monitoring from 2003 to 2010 using Envisat data. In *Proceedings of Fringe 2011 Workshop*, 2011.

T. R. Emardson, M. Simons, and F. H. Webb. Neutral atmospheric delay in interferometric synthetic aperture radar applications: Statistical description and mitigation. *Journal of Geophysical Research: Solid Earth*, 108(B5):2231, 2003.

T.G. Farr, P.A. Rosen, E. Caro, R. Crippen, R. Duren, S. Hensley, M. Kobrick, M. Paller, E. Rodriguez, L. Roth, D. Seal, S. Shaffer, J. Shimada, J. Umland, M. Werner, M. Oskin, D. Burbank, and D. Alsdorf. The shuttle radar topography mission. *Reviews of Geophysics*, 45(2), 2007.

A. Ferretti, C. Prati, and F. Rocca. Nonlinear subsidence rate estimation using permanent scatterers in differential SAR interferometry. *IEEE Transactions on Geoscience and Remote Sensing*, 38(5):2202–2212, 2000.

A. Ferretti, C. Prati, and F. Rocca. Permanent scatterers in SAR interferometry. *IEEE Transactions on Geoscience and Remote Sensing*, 39(1):8–20, 2001.

A. Ferretti, A. Fumagalli, F. Novali, C. Prati, F. Rocca, and A. Rucci. A new algorithm for processing interferometric data-stacks: SqueeSAR. *IEEE Transactions on Geoscience and Remote Sensing*, 49(9):3460–3470, 2011.

S. Fujiwara, T. Nishimura, M. Murakami, H. Nakagawa, M. Tobita, and P.A. Rosen. 2.5-D surface deformation of M6.1 earthquake near Mt Iwate detected by SAR interferometry. *Geophysical Research Letters*, 27(14):2049–2052, 2000.

Y. Fukushima. Persistent scatterer interferometry by using StaMPS package (in Japanese with abstract and figure captions in English). *Journal of the Geodetic Society of Japan*, 57(2):41–48, 2010.

Y. Fukushima and A. Hooper. Crustal deformation after 2004 Niigataken-Chuetsu earthquake, central Japan, investigated by persistent scatterer interferometry (in Japanese with abstract and figure captions in English). *Journal of the Geodetic Society of Japan*, 57(4):195–214, 2010.

M. Furuya. Quasi-static thermoelastic deformation in an elastic half-space: theory and application to InSAR observations at Izu-Oshima volcano, Japan. *Geophysical Journal International*, 161(1):230–242, 2005.

M. Furuya, K. Mueller, and J. Wahr. Active salt tectonics in the Needles District, Canyonlands (Utah) as detected by interferometric synthetic aperture radar and point target analysis: 1992-2002. *Journal of Geophysical Research: Solid Earth*, 112:B06418, 2007.

F. Gatelli, A. M. Guamieri, F. Parizzi, P. Pasquali, C. Prati, and F. Rocca. The wavenumber shift in SAR interferometry. *IEEE Transactions on Geoscience and Remote Sensing*, 32(4):855–865, 1994.

P.J. González and J. Fernández. Error estimation in multitemporal InSAR deformation time series, with application to Lanzarote, Canary Islands. *Journal of Geophysical Research*, 116(B10):B10404, 2011.

R.F. Hanssen. *Radar interferometry: data interpretation and error analysis*, volume 2. Kluwer Academic Pub, 2001.

T. Hoogland, J.J.H van den Akker, and D.J. Brus. Modeling the subsidence of peat soils in the Dutch coastal area. *Geoderma*, 171:92–97, 2012.

A. Hooper. A multi-temporal InSAR method incorporating both persistent scatterer and small baseline approaches. *Geophysical Research Letters*, 35(16):16, 2008.

A. Hooper. A statistical-cost approach to unwrapping the phase of InSAR time series. In *Proceedings of Fringe 2009 Workshop*, page 6, 2010.

A. Hooper, H. Zebker, P. Segall, and B. Kampes. A new method for measuring deformation on volcanoes and other natural terrains using InSAR persistent scatterers. *Geophysical Research Letters*, 31(23):L23611, 2004.

A. Hooper, P. Segall, and H. Zebker. Persistent scatterer interferometric synthetic aperture radar for crustal deformation analysis, with application to Volcán Alcedo, Galápagos. *Journal of Geophysical Research: Solid Earth*, 112:B07407, 2007.

A. Hooper, D. Bekaert, K. Spaans, and M. Arıkan. Recent advances in SAR interferometry time series analysis for measuring crustal deformation. *Tectonophysics*, 514:1–13, 2012.

A. Huete, K. Didan, T. Miura, E.P. Rodriguez, X. Gao, and L.G. Ferreira. Overview of the radiometric and biophysical performance of the MODIS vegetation indices. *Remote sensing of environment*, 83(1):195–213, 2002.

R.L. Jordan, E.R. Caro, Y. Kim, M. Kobrick, Y. Shen, F.V. Stuhr, and M.U. Werner. Shuttle radar topography mapper (SRTM). In *Satellite Remote Sensing III*, pages 412–422, 1996.

B. Kampes, R.F. Hanssen, and Z. Perski. Radar interferometry with public domain tools. In *Proceedings of Fringe 2003 Workshop*, 2003.

B.M. Kampes. *Displacement parameter estimation using permanent scatterer interferometry*. Springer, 2005.

H. Kawawa and F. Suga. Monitoring around tokai area using high resolution vertical positioning analysis network. *Journal of the Ggeographical Survey Institute*, (93): 34–43, 2000.

H. Kimura and Y. Yamaguchi. Detection of landslide areas using satellite radar interferometry. *Photogrammetric Engineering & Remote Sensing*, 66(3):337–344, 2000.

T. Kobayashi, M. Tobita, T. Nishimura, A. Suzuki, Y. Noguchi, and M. Yamanaka. Crustal deformation map for the 2011 off the Pacific coast of Tohoku earthquake, detected by InSAR analysis combined with GEONET data. *Earth, Planets and Space*, 63(7):621–625, 2011.

T. Kobayashi, M. Tobita, M. Koarai, T. Okatani, A. Suzuki, Y. Noguchi, M. Yamanaka, and B. Miyahara. InSAR-derived crustal deformation and fault models of normal faulting earthquake (Mj 7.0) in the Fukushima-Hamadori area. *Earth, Planets and Space*, 64(12):1209–1221, 2012.

T. Kobayashi, M. Ishimoto, M. Tobita, and H. Yarai. A tool for reduction of atmosphere-related noises included in an insar image, incorporating a numerical weather model. *Journal of the Geospatial Information Authority of Japan*, 125: 31–38, 2014.

R. Lanari, F. Casu, M. Manzo, G. Zeni, P. Berardino, M. Manunta, and A. Pepe. An overview of the small baseline subset algorithm: A DInSAR technique for surface deformation analysis. *Pure and Applied Geophysics*, 164(4):637–661, 2007.

C.A. Langeveld, R. Segers, B.O.M. Dirks, A. van den Pol-van Dasselaar, G.L. Velthof, and A. Hensen. Emissions of CO2, CH4 and N2O from pasture on drained peat soils in the Netherlands. *European Journal of Agronomy*, 7(1-3):35–42, 1997.

T.R. Lauknes, H.A. Zebker, and Y. Larsen. InSAR deformation time series using an

L1-norm small-baseline approach. *IEEE Transactions on Geoscience and Remote Sensing*, 49(1):536–546, 2011.

H. Laur, P. Bally, P. Meadows, J. Sanchez, B. Schaettler, E. Lopinto, and D. Esteban. Derivation of the backscattering coefficient σ^0 in ESA ERS SAR PRI products. *ESA, Noordjiwk, The Netherlands, ESA Document ES-TN-RE-PM-HL09*, (2), 2002.

M. Lavalle, M. Simard, and S. Hensley. A temporal decorrelation model for polarimetric radar interferometers. *IEEE Transactions on Geoscience and Remote Sensing*, 50(7):2880–2888, 2012.

P. López-Quiroz, M.P. Doin, F. Tupin, P. Briole, and J.M. Nicolas. Time series analysis of Mexico City subsidence constrained by radar interferometry. *Journal of Applied Geophysics*, 69(1):1–15, 2009.

D. Massonnet, M. Rossi, C. Carmona, F. Adragna, G. Peltzer, K. Feigl, and T. Rabaute. The displacement field of the landers earthquake mapped by radar interferometry. *Nature*, 364(6433):138–142, 1993.

D. Massonnet, K. Feigl, M. Rossi, and F. Adragna. Radar interferometric mapping of deformation in the year after the landers earthquake. *Nature*, 369(6477):227–230, 1994.

L. Montanarella, R.J.A. Jones, and R. Hiederer. The distribution of peatland in Europe. *Mires and Peat*, 1(1), 2006.

H. Nakagawa, M. Murakami, and S. Fujiwara. Land subsidence of the northern Kanto plains detected by JERS-1 SAR interferometry (in Japanese with abstract

and figure captions in English). *Journal of the Geodetic Society of Japan*, 45(4): 347–350, 1999.

A.H.M. Ng, H.C. Chang, L. Ge, C. Rizos, and M. Omura. Assessment of radar interferometry performance for ground subsidence monitoring due to underground mining. *Earth, Planets and Space*, 61(6):733–745, 2009.

H.S. Nieuwenhuis and F. Schokking. Land subsidence in drained peat areas of the province of Friesland, the Netherlands. *Quarterly Journal of Engineering Geology and Hydrogeology*, 30(1):37–48, 1997.

T. Nishimura, S. Fujiwara, M. Murakami, M. Tobita, H. Nakagawa, T. Sagiya, and T. Tada. The M6.1 earthquake triggered by volcanic inflation of Iwate Volcano, northern Japan, observed by satellite radar interferometry. *Geophysical Research Letters*, 28(4):635–638, 2001.

S. Ozawa, M. Murakami, S. Fujiwara, and M. Tobita. Synthetic aperture radar interferogram of the 1995 Kobe earthquake and its geodetic inversion. *Geophysical Research Letters*, 24(18):2327–2330, 1997.

T. Ozawa and E. Fujita. Local deformations around volcanoes associated with the 2011 off the Pacific coast of Tohoku earthquake. *Journal of Geophysical Research: Solid Earth*, 118(1):390–405, 2013.

T. Ozawa and H. Ueda. Advanced interferometric synthetic aperture radar (InSAR) time series analysis using interferograms of multiple-orbit tracks: A case study on Miyake-jima. *Journal of Geophysical Research*, 116(B12):B12407, 2011.

A. Parizzi and R. Brcic. Adaptive InSAR stack multilooking exploiting amplitude statistics: A comparison between different techniques and practical results. *IEEE Geoscience and Remote Sensing Letters*, 8(3):441–445, 2011.

A. Parizzi, X.Y. Cong, and M. Eineder. First results from multifrequency interferometry. A comparison of different decorrelation time constants at L, C and X band. In *Proceedings of Fringe 2009 Workshop*, 2009.

A. Pepe, E. Sansosti, P. Berardino, and R. Lanari. On the generation of ERS/ENVISAT DInSAR time-series via the SBAS technique. *IEEE Geoscience and Remote Sensing Letters*, 2(3):265–269, 2005.

A.N. Pettitt. A two-sample Anderson-Darling rank statistic. *Biometrika*, 63(1):161–168, 1976.

M. Peyret, S. Dominguez, R. Cattin, J. Champenois, M. Leroy, and A. Zajac. Present-day interseismic surface deformation along the Longitudinal Valley, eastern Taiwan, from a PS-InSAR analysis of the ERS satellite archives. *Journal of Geophysical Research: Solid Earth*, 116:B03402, 2011.

E.J.M. Rignot. Effect of faraday rotation on L-band interferometric and polarimetric synthetic-aperture radar data. *IEEE Transactions on Geoscience and Remote Sensing*, 38(1):383–390, 2000.

F. Rocca. Modeling interferogram stacks. *IEEE Transactions on Geoscience and Remote Sensing*, 45(10):3289–3299, 2007.

P.A. Rosen, S. Hensley, H.A. Zebker, F.H. Webb, and E.J. Fielding. Surface deforma-

tion and coherence measurements of Kilauea Volcano, Hawaii, from SIR-C radar interferometry. *Journal of Geophysical Research*, 101:23–23, 1996.

P.A. Rosen, S. Hensley, I.R. Joughin, F.K. Li, S. Madsen, E. Rodríguez, and R. Goldstein. Synthetic aperture radar interferometry. *Proceedings of the IEEE*, 88(3): 333–382, 2000.

S. Samieie-Esfahany and R.F. Hanssen. Time-series InSAR: An integer least-squares approach for distributed scatterers. In *Proceedings of Fringe 2011 Workshop*, 2011.

D.T. Sandwell, D. Myer, R. Mellors, M. Shimada, B. Brooks, and J. Foster. Accuracy and resolution of ALOS interferometry: Vector deformation maps of the Father's Day intrusion at Kilauea. *IEEE Transactions on Geoscience and Remote Sensing*, 46(11):3524–3534, 2008.

H.P. Sato, T. Okatani, M. Koarai, A. Suzuki, M. Tobita, H. Yarai, and T. Sekiguchi. Study on detection of landslide-induced surface deformation using SAR interferograms : Case study in Mt. Gassan area, Yamagata Pref., Japan (in Japanese with abstract and figure captions in English). *Journal of the Japan Landslide Society*, 49(2):61–67, 2012.

H.P. Sato, B. Miyahara, T. Okatani, M. Koarai, T. Sekiguchi, and H. Yagi. Detection of landslide surface deformation triggered by the 2011 off the Pacific coast of Tohoku earthquake using InSAR image (in Japanese with abstract and figure captions in English). *Journal of the Japan Landslide Society*, 51(2):5–13, 2014.

F.W. Scholz and M.A. Stephens. K-sample Anderson-Darling tests. *Journal of the American Statistical Association*, 82(399):918–924, 1987.

C.J. Schothorst. Subsidence of low moor peat soils in the western Netherlands. *Geoderma*, 17(4):265–291, 1977.

R. Shamshiri, M. Motagh, M. Baes, and M. Sharifi. Deformation analysis of the Lake Urmia causeway (LUC) embankments in northwest Iran: insights from multi-sensor interferometry synthetic aperture radar (InSAR) data and finite element modeling (FEM). *Journal of Geodesy*, 88(12):1171–1185, 2014.

Q. Sun, L. Zhang, X. Ding, J. Hu, and H. Liang. Investigation of slow-moving landslides from ALOS/PALSAR images with TCPInSAR: A case study of Oso, USA. *Remote Sensing*, 7(1):72, 2014.

L.M.T. Swart. Spectral filtering and oversampling for radar interferometry. Master's thesis, Faculty of Geodetic Engineering, Delft University of Technology, 2000.

T. Tachikawa, M. Hato, M. Kaku, and A. Iwasaki. Characteristics of ASTER GDEM version 2. In *Geoscience and Remote Sensing Symposium (IGARSS), 2011 IEEE International*, pages 3657–3660, 2011.

Y. Takada and Y. Fukushima. Volcanic subsidence triggered by the 2011 Tohoku earthquake in Japan. *Nature Geoscience*, 6(8):637–641, 2013.

M. Tobita, T. Nishimura, T. Kobayashi, K.X. Hao, and Y. Shindo. Estimation of co-seismic deformation and a fault model of the 2010 Yushu earthquake using PALSAR interferometry data. *Earth and Planetary Science Letters*, 307(3):430–438, 2011.

X. Tong, D.T. Sandwell, and B. Smith-Konter. High-resolution interseismic velocity data along the San Andreas Fault from GPS and InSAR. *Journal of Geophysical Research: Solid Earth*, 118(1):369–389, 2013.

R. Touzi, A. Lopes, J. Bruniquel, and P.W. Vachon. Coherence estimation for SAR imagery. *IEEE Transactions on Geoscience and Remote Sensing*, 37(1):135–149, 1999.

H. Une, Sato H.P., H. Yarai, and M. Tobita. Analysis of surface deformation induced by the Noto Hanto and the Chuetsu-oki Earthquakes in 2007 using synthetic aperture radar interferograms (in Japanese with abstract and figure captions in English). *Journal of the Japan Landslide Society*, 45(2):125–131, 2008.

J. van Huissteden, R. van den Bos, and I.M. Alvarez. Modelling the effect of water-table management on CO_2 and CH_4 fluxes from peat soils. *Netherlands Journal of Geosciences*, 85(1):3, 2006.

F. van Leijen and R.F. Hanssen. Ground water management and its consequences in Delft, the Netherlands as observed by persistent scatterer interferometry. In *Proceedings of Fringe 2007 Workshop*, 2007.

Alterra Wageningen UR. Grondsoortenkaart 2006 - simplified soil map of the Netherlands. http://dx.doi.org/10.17026/dans-xky-fsk5, 2006.

M. Wei and D.T. Sandwell. Decorrelation of L-band and C-band interferometry over vegetated areas in California. *IEEE Transactions on Geoscience and Remote Sensing*, 48(7):2942–2952, 2010.

M. Wei, D.T. Sandwell, and B. Smith-Konter. Optimal combination of InSAR and GPS for measuring interseismic crustal deformation. *Advances in Space Research*, 46(2):236–249, 2010.

P.A. Wright, S. Quegan, N.S. Wheadon, and C.D. Hall. Faraday rotation effects on L-band spaceborne SAR data. *IEEE Transactions on Geoscience and Remote Sensing*, 41(12):2735–2744, 2003.

H.A. Zebker and J. Villasenor. Decorrelation in interferometric radar echoes. *IEEE Transactions on Geoscience and Remote Sensing*, 30(5):950–959, 1992.